Lars-Erik Owe

Characterisation of Iridium Oxides for Acidic Water Electrolysis

Thesis for the degree of Philosophiae Doctor

Trondheim, June 2011

Norwegian University of Science and Technology
Faculty of Natural Sciences and Technology
Department of Materials Science and Engineering

NTNU – Trondheim
Norwegian University of
Science and Technology

NTNU
Norwegian University of Science and Technology

Thesis for the degree of Philosophiae Doctor

Faculty of Natural Sciences and Technology
Department of Materials Science and Engineering

ISBN 978-82-471-2930-2 (printed ver.)
ISBN 978-82-471-2931-9 (electronic ver.)
ISSN 1503-8181

Doctoral theses at NTNU, 2011:190

IMT-Report 2011:139

Printed by NTNU-trykk

Preface

This thesis consists of three main parts. The first is an introductory part giving a general introduction, a brief discussion of some of the theory behind the work and a literature overview of the main topics of the thesis. The second part consists of six separate chapters written as papers. Two papers are published and one submitted. The remaining papers are being prepared for submission. The final section is a general conclusion of the work.

After the final section a list of acronyms and symbols used in the thesis can be found. A list of of figures and tables is also included.

All figures, tables, equations and references are numbered continuously throughout the thesis. All the references can be found at the back of the thesis.

Concerning the six papers in the thesis I have contributed to them as follows:

Chapter 7: An impedance model for a porous intercalation electrode with mixed conductivity [1], S. Sunde, I. A. Lervik, L.-E. Owe, M. Tsypkin, *J. Electrochem. Soc.*, 156 (2009) B927–B937: The impedance model was developed and the paper was written mainly by S. Sunde with contributions from I. A. Lervik, M. Tsypkin and myself. This paper was also a part of the PhD thesis of I. A. Lervik.

Chapter 8: Impedance Model for Anodically Formed Iridium Oxide Films: The model was developed by S. Sunde with contributions from myself. I have performed all the computer simulations and done all the experimental work. The paper was written mainly by myself, except for the description of the model that was written by S. Sunde.

Chapter 9: The impedance of iridium-tin oxide: The paper has to a large extent been written by me. I did the experimental work with help from M. Tsypkin. The XPS data was recorded by Professor S. Raaen and the data analysis was done by I. A. Lervik.

Chapter 10, Iridium ruthenium oxide powders, I have written alone. I have done all the experimental work except for the XRD analysis, which has been done in cooperation with M. Tsypkin.

Chapter 11: Electrochemical behaviour of iridium oxide films in trifluromethanesulfonic acid [2], L.-E. Owe, I. A. Lervik, M. Tsypkin, M. V. Syre and S. Sunde, *J. Electrochem. Soc.*, 157 (2010) B1719–B1725: The paper was written by myself with contributions from S. Sunde. I performed all the experimental work except for the measurements of the flat band potentials that were done by I. A. Lervik and M. V. Syre.

Chapter 12: The effect of phosphate on the oxygen evolution reaction on iridium oxide: S. Sunde and myself wrote in the paper in cooperation. I did all the experi-

mental work except for some initial experiments done by students under S. Sunde's and my supervision.

Acknowledgements

The four, almost five, years I have been working on my PhD have been happy years. I owe a lot of people a great deal for making it so. As a preliminary text under this heading I have had "Takk til alle" (Thank you to all). In many ways those three simple words would say it all. However, let me elaborate.

First of all I have to thank my supervisor Svein Sunde for taking me on as his first new PhD student and giving me the help and support I needed.

Secondly I am grateful for the support, help, discussions and fun I have had with the Electrochemical Energy group, both past and present members. I would especially like to thank Ass. Prof. Frode Seland and Prof. Em. Reidar Tunold for all the fruitful discussions and advice they have given me. In the laboratory Dr. Mikhail Tsypkin has been of invaluable help.

I have been so lucky that I have shared my office with several great people. We have had a lot of engaging discussions, both scientific and not. So, Frode, Jana, Anawati, Marte and David, thank you for all the help you have given me, all the discussions we have had and for putting up with me.

The technical and administrative staff at the department has been of great assistance, particularly Martha Bjerknes and Kjell Røkke. They have helped me with a slew of practical problems and for that I am thankful.

I would also like to thank Prof. Richard Haverkamp from the Massey University, New Zealand for the illuminating discussions we had during his stay at NTNU. I also appreciated him giving me my first lesson in how to operate an AFM and for offering to do synchrotron XRD on some of my samples.

My salary has been provided by the Department of Materials Science and Engineering, and I am grateful for that as I have enjoyed having a paid job. I am also grateful for the financing I have gotten from the EU project WELTEMP (project nr.: 212903) that has provided me with the funds to cover experimental costs.

I have been so lucky that I have been able to attend several conferences and meetings both in Norway and abroad. The funds that have made this possible have been provided by the Faculty of Natural Science and Technology, the NTH-fond, WELTEMP and Prof. G. M. Haarberg. I am grateful for the support.

I should also mention the two people that were the main inspiration in my choice of chemistry as a subject: Borgny Hoddevik, my middle school science teacher and Berit Storm, my high school science and chemistry teacher. I am grateful for their inspiration.

My friends have made my leisure time in Trondheim a much more enjoyable time. I don't think I would have been able to finish my thesis without all the fun I have had

with them (or perhaps I would have finished in half the time?). I would especially like to thank the "Voll-gang" and all my friends from my days as a chemistry student. I also have a good time each time I travel back and meet my old friends from home in Bærum and it gives me something to look forward to.

Finally I am ever grateful for all the help and support I have gotten from my family, despite the occasional hint that I should move back south closer to them. In the end my family really does matter the most to me.

Lars-Erik Owe
Gløshaugen, 15th of April 2011

Summary

This thesis covers several topics related to catalysts, in particular iridium oxide based catalysts, for the oxygen evolution reaction (OER) in polymer electrolyte membrane water electrolysers (PEM WE). The focus is on the OER as the energy losses are greater for the OER than for the cathode process, the hydrogen evolution reaction. The aim is to improve the understanding of the role of the catalyst and the electrolyte in the OER in acidic water electrolysers.

Iridium oxide was used in the form of anodically formed iridium oxide films (AIROF) and both pure and mixed iridium oxide powders. Iridium-tin oxides were prepared using the polyol method and iridium-ruthenium oxides were prepared using the hydrolysis method. Electrodes were made either by spraying an ink of the oxide, Nafion solution and isopropanol on a titanium plate, or by deposition of the catalyst on a glassy carbon rotating disk electrode and in some cases covering it with a layer of Nafion.

A mathematical impedance model for a porous intercalation electrode with the possibility of mixed conductivity was developed. Compared with a porous intercalation electrode with metallic conductivity the impedance in the high frequency region is similar. In the low frequency region significant deviations can be seen. The differences are related to the diffusion in the particles and exchange of electrons at the interface between the electrode and the support. Recombination of the charge carriers is also included. This also gives deviations in the low frequency region if the recombination rate is large.

An impedance model, based on dilute solution theory, was also developed for intercalation electrodes with mixed conductivity, such as AIROF. The model predicts the impedance of AIROF to a large degree. To do so the model must include diffusion, including the possibility of trapping of the charge carriers, the faradaic reactions and potential gradients in the system. AIROF acts as a dense film, not a porous electrode. Neither the model or the impedance of AIROF showed clear signs of the semiconductor to conductor transition in AIROF. Trapping was observed in the reduced state of the film.

Iridium-tin oxides were prepared using the polyol method. The background for adding tin to iridium oxide was to reduce the amount of iridium, an expensive noble metal, in the OER catalyst. Tin oxide is a semiconductor, thus it it is important to investigate the conductivity of the catalyst and potential conductivity changes with potential. An impedance study, using the impedance model for a porous intercalation electrode for analysis, was performed. Samples heat treated at 500 °C and samples of pure iridium were found to behave as porous electrodes. The remaining

samples, heat treated at lower temperatures, behaved as dense film electrodes. A heat treatment temperature of 400 °C is not high enough to give good OER activity. Conductivity changes with potential could not be confirmed, however they could not be ruled out either.

Ruthenium oxide has a higher activity for the OER than iridium oxide, however the stability is too low for practical applications. To circumvent this, mixed iridium-ruthenium oxide catalysts were prepared in the hope that the activity would be greater than pure iridium oxide and the stability better than pure ruthenium oxide. Both producing homogeneous chemically mixed catalysts and proving that they were formed proved to be difficult. The mixed iridium-ruthenium oxide catalysts appeared to be physical mixtures of nearly pure iridium oxide and a phase different from pure ruthenium oxide.

AIROF electrodes in trifluoromethanesulfonic acid (TFMSA) were used as a model system to study possible interactions between iridium oxide catalysts and Nafion membranes in PEM WE. A higher rate for the OER and a higher flat band potential in TFMSA point to a significantly higher adsorption of sulphates than triflate on the iridium oxide surface. In both sulphuric acid and TFMSA with $Fe(CN)_6^{3-/4-}$ the oxidation current of the redox couple was much higher than the reduction current. The addition of 10 ppm chloride caused the "blocking" of the cathodic current in TFMSA to disappear and the electrode behaved as a metal electrode. The same effect was not observed in sulphuric acid. This effect is believed to be caused by the lower adsorption of electrolyte species in TFMSA than in sulphuric acid. This allows the chloride greater access to the electrode surface where it hinders reoxidation of exposed iridium metal in cracks in the oxide film.

For PEM WE operating above 100 °C a different electrolyte membrane than Nafion is needed. A polybenzimidazole membrane can be used, however it must be doped with phosphoric acid to improve the conductivity. To investigate effects of phosphate adsorption on iridium oxide catalysts for the OER, the adsorption of phosphates was studied using both AIROF and iridium oxide powder electrodes. In addition to cyclic voltammetry and steady state polarisation measurements experiments were conducted on an electrochemical quartz crystal microbalance. For comparison experiments in sulphuric and perchloric acid were conducted. The rate of the OER was slowest in phosphoric acid and fastest in perchloric acid. The rate of the OER increased with increasing temperature and decreased with increasing phosphate concentration. A preliminary equation to predict the rate of the OER with respect to concentration and temperature was proposed. The results can be interpreted as a greater extent of blocking of the active sites for the OER in phosphate solutions, as compared to perchlorate solutions.

Contents

Part I

Introduction, theory and literature review

Chapter 1

Introduction

> "The wind bloweth where it listeth, and thou hearest the sound thereof, but canst not tell whence it cometh, and whither it goeth"
> *John 3:8*

1.1 Global warming and the hydrogen economy

With rising concern about global warming and the depletion of fossil fuel reserves, alternatives to fossil fuels are being sought [3]. One alternative that is gaining acceptance is to use hydrogen as an energy carrier. Hydrogen has the highest energy density on a weight basis of all known fuels, 142 MJ/kg (HHV). The combustion of hydrogen, for example in a fuel cell or in an internal combustion engine, releases only water to the environment.

Wind and solar energy are both intermittent sources of renewable energy. The wind must blow or the sun must shine if energy is to be produced. Accordingly energy must be stored for use when the energy production is lower than the need. Converting excess electrical energy into hydrogen is a way of storing energy for use in times of energy shortages.

A "clean" way of producing hydrogen is needed as hydrogen is not an energy source in itself. Water electrolysis is, at the moment, the best alternative [4]. If electricity is produced from renewable sources, hydrogen can be produced by water electrolysis without emissions of greenhouse gases. Hydrogen will then be a fuel that does not result in greenhouse gas emissions either in production or in use.

Statoil used this idea in the Utsira project[1]. Two wind turbines provided power to 10 of the households on the island. In times of excessive energy production the surplus energy was used to produce hydrogen and oxygen by water electrolysis. The hydrogen was stored in a pressure vessel until the wind turbines produced less power than required. Hydrogen was then fed to a fuel cell that converted hydrogen and oxygen to electric power or to a hydrogen fuelled internal combustion engine that powered a generator producing electric power.

[1] More details about the project can bee found at Statoil's Utsira project web pages: url: www.statoil.com/no/NewsAndMedia/Multimedia/features/Pages/HydrogenSociety.aspx (last read the 2 of July 2010)

A similar project is run by The International Energy Agency. The project aims to demonstrate the integration of a wind turbine with a water electrolyser[2]. On a slightly larger scale there are plans to make Iceland into the first country embracing the hydrogen economy [5]. Plans for the introduction of hydrogen as a fuel also exist for Norway [6].

The methanol economy, in which methanol is the energy carrier, is proposed by some to be the replacement of the fossil fuels in use today [7] as an alternative to the hydrogen society. Today the majority of methanol is produced from fossil fuel, mainly methane, via syn-gas (a mix of CO, CO_2 and H_2), although production by fermentation of biomass is also possible. Alternatively CO_2 and H_2 can be converted to methanol in essentially the same process. The CO_2 can be separated from exhaust from industrial plants or fossil fuel burning power plants or, eventually, collected from the atmosphere. Obviously a large amount of hydrogen will be required. It would not make much sense to produce the hydrogen from fossil fuels. Water electrolysis, with electricity from a renewable source or from a nuclear power plant, would be the obvious choice.

1.2 Motivation for the thesis

The main purpose of this work is to improve the understanding of the catalysts and electrolytes role in the oxygen evolution reaction (OER) in acidic water electrolysis. The OER is a bigger source of energy loss than the hydrogen evolution reaction [8,9]. Concentration on the OER thus seems appropriate to reduce the energy consumption for water electrolysis.

[2]For more information see: url: http://ieahia.org/pages/static/task24.htm (read the 2 of November 2010)

Chapter 2

Theory

2.1 Electrochemical thermodynamics and kinetics

A brief introduction to electrochemical thermodynamics and kinetics will be given here [10–12]. As an example a general reaction will be used:

$$oO + n\mathrm{e}^- \leftrightarrows rR \tag{2.1}$$

The standard potential, E^0, for a reaction can be found from:

$$E^0 = \frac{\Delta G^0}{n\mathrm{F}} = \frac{\Delta H^0 - T\Delta S^0}{n\mathrm{F}} \tag{2.2}$$

In the equation n is the number of electrons transferred in reaction (2.1) and F = 96485 As/mol is Faradays number and the temperature is T in Kelvin. ΔG^0, ΔH^0 and S^0 are the standard Gibbs energy, the standard enthalpy and the standard entropy of reaction 2.1, respectively.

The reversible potential, E^{rev}, is the potential of the reaction at steady state at the actual operating conditions. E^{rev} is given by the Nernst equation:

$$E^{rev} = E^0 - \frac{\mathrm{R}T}{n\mathrm{F}} \ln \frac{a_R^r}{a_O^o} \tag{2.3}$$

The activity of the reduced and oxidised specie is a_R and a_O respectively.

At E^{rev} the cathodic current, i_c, is equal in size to the anodic current, i_a, which is equal to the exchange current density, i_0: $-i_c = i_a = i_0$. At potentials different from E^{rev} the current, i, can be found from the Butler–Volmer equation:

$$i = \mathrm{i}_0 \left\{ \mathrm{e}^{\left(\frac{\beta n\mathrm{F}}{\mathrm{R}T}\eta_a\right)} - \mathrm{e}^{\left(\frac{(1-\beta)n\mathrm{F}}{\mathrm{R}T}\eta_c\right)} \right\} \tag{2.4}$$

The overpotential, η, is the potential difference between the reversible potential and the actual applied potential and β is the symmetry factor. a and c denotes the anode and cathode, respectively.

From the Butler–Volmer equation it is possible to derive the anodic and cathodic Tafel equations by letting the overpotential become large in the anodic and cathodic direction. The cathodic or anodic current, respectively, can then be neglected.

$$E = \frac{\mathrm{R}T\ln(10)}{\beta n\mathrm{F}} \cdot \log\frac{i_a}{\mathrm{i_0}} = b_a \cdot \log\frac{i_a}{i_0} \tag{2.5}$$

$$E = -\frac{\mathrm{R}T\ln(10)}{(1-\beta)n\mathrm{F}} \cdot \log\frac{i_c}{\mathrm{i_0}} = b_c \cdot \log\frac{i_c}{i_0} \tag{2.6}$$

Equation (2.5) is the anodic Tafel equation and Equation (2.6) the cathodic. The exchange current density, i_0 and the Tafel slope, b_a or b_c, are dependent on the system under study and can be used to compare different catalysts. The Tafel slopes are particularly useful since they are not dependent on the electrode area.

The total cell voltage, E_{cell}, is a product of the reversible cell potential, E^{rev}, at the operating conditions, the various overpotentials, η, and the ohmic drop in the cell. Equation (2.7) gives an expression for the cell potential.

$$E_{cell} = E^{rev} + |\eta_c| + \eta_a + IR_{\mathrm{cell}} \tag{2.7}$$

The ohmic resistance in the cell is R_{cell} and the total current is I. The overpotential can be split into a part caused by the kinetics, the activation overpotential, η_{act} and a part caused by mass transport, the concentration overpotential, η_{conc}.

2.2 Electrochemical methods

This section describes a few details about the electrochemical methods used in this work, with emphasis on the procedures not commonly used. A full description of the electrochemical methods can be found in an electrochemistry textbook, see for example Ref. [10–12].

2.2.1 Normalising electrochemical measurements

When comparing two electrodes that do not have the same electrical charge it can be advantageous to normalise the charge. The charge of the electrode can be found by integrating the current potential curve. Determining the charge at different sweep rates, ν, makes it possible to find the inner, outer and total charge of the electrode [13]. The inner charge represents the active sights of the electrode that are hard to get at (deep within the electrode), the outer charge is a measure of the sights that are easy to get at and the total charge is, naturally, a measure of all the active sights. To put it in other words, if cyclic voltammetry (CV) at a high speed is recorded it will be the easily accessible sights that are responsible for the current, conversely if the sweep rate is slow (almost) all the sights will be active. This is the basis for finding the inner, outer and total charge.

The inner, outer and total charge can be found using the procedure given in [13]. Briefly, the outer charge can be found by plotting the integrated charge, q^*, against the inverse of the square root of the sweep rate, $1/\sqrt{\nu}$. This should result in a straight line. Extrapolating the curve to zero ($\nu \to \infty$) gives the outer charge. The total charge is found by plotting $1/q^*$ against $\sqrt{\nu}$, which should also give a straight curve.

Extrapolating to zero ($\nu \rightarrow 0$) gives the total charge. The difference between the total and the outer charge gives the inner charge.

The sweep rate dependence of the charge can be explained by diffusion of reactants in the electrode [13], specifically of protons inside the oxide catalyst. The other explanation is based on charging of the double layer in addition to a Faradaic contribution [14]. This is further discussed in Ref. [15, 16]. Some caution should be used when using the charge found at potentials below that of the OER to describe the area available for the OER [17]. The double layer capacitance found from electrochemical impedance spectroscopy is a more suitable choice.

2.2.2 Electrochemical Impedance Spectroscopy

Electrochemical Impedance Spectroscopy (EIS) has been used to investigate the electrode processes and adsorption on the electrode in this work, see Chapter 7, Chapter 8 and Chapter 9. Although EIS has not been used to study the oxygen evolution reaction in this work, it is worth mentioning that it is possible [18–20].

The Mott–Schottky equation

The background for the Mott–Schottky equation was developed by Mott [21] and Schottky [22, 23] in the nineteen thirties and forties.

Semiconductor electrodes have an excess charge in the space charge region, except at the flat band potential, $\mathrm{E_{fb}}$. The excess charge leads to a capacitance, the space charge capacitance, C_{sc}. The Mott–Shottky equation, equation (2.8), gives the relationship between the C_{sc} and the potential applied to the electrode [12, ch. 18.2], [24, p. 259–260].

$$\frac{1}{C_{\mathrm{sc}}^2} = \frac{2}{e\epsilon_0\epsilon \mathrm{N_d}} \left(-\Delta\phi - \frac{\mathrm{kT}}{e} \right) \tag{2.8}$$

In the equation ϵ_0 is the permittivity of vacuum, ϵ is the dielectric constant and $\mathrm{N_d}$ is the dopant concentration in the semiconductor. $\Delta\phi$ is given by $\Delta\phi = \mathrm{E} - \mathrm{E_{fb}}$, where E is the applied potential. k is the Boltzmann constant. The Mott–Shottky relationship is only valid for solid, crystalline semiconductors (not powders or amorphous solids).

The equation predicts that there is a linear relationship between the applied potential, E and $1/C_{\mathrm{sc}}^2$. A plot of $1/C_{\mathrm{sc}}^2$ against the applied potential is called a Mott–Shottky plot [24, p. 259–260]. The point of intersection between the plot and the potential axis gives the flat band potential, whilst the slope of the plot is inversely proportional to the dopant concentration in the semiconductor.

Adsorption of ions on the semiconductor surface will give a compensating charge in the semiconductor. $\mathrm{E_{fb}}$ will thus change if the charge caused by adsorption of ions changes[1]. Adsorption of anions will give a negative shift of the $\mathrm{E_{fb}}$ [25].

Oxide films grown on metals will often have a smaller linear region in the Mott–Schottky plot than a bulk semiconductor. This is caused by the oxide layer being

[1] The total charge must change, if say a number of ions with charge -1 are replaced by the same number of ions of a different type, but still with charge -1, the flat band potential will not change.

thin compared to the thickness of the space charge layer. Also the value of N_d will not correspond to the impurity concentration, instead it will be a measure of the nonstoichiometry of the oxide film [25, 26].

Variations of the flat band potential, E_{fb}, with the frequency have been observed for some systems, for example on single crystal zinc oxide [27]. The frequency dependence should be checked for all systems. However, since most studies use approximately the same frequency this effect is largely cancelled when comparing results [26].

2.2.3 Electrochemical quarts crystal microbalance

The Electrochemical quarts crystal microbalance (EQCM) combines electrochemical and mass measurements [28]. The mass change of the electrode can be followed as the electrochemical measurement is conducted. Small mass changes, in the sub nano gram range, can be measured. The principle of the measurement is based on following the change in the resonance frequency of a quarts crystal that also acts as the working electrode. The frequency will change when the mass of the crystal changes. An increasing mass gives a decreasing resonant frequency. The Sauerbery equation [28, 29] gives the relationship between the frequency and mass change:

$$\Delta f = -\frac{2f_0^2 \Delta m}{A(\mu_q \rho_q)^{1/2}} \tag{2.9}$$

In the equation Δf is the change of the resonance frequency of the EQCM crystal, f_0 is the resonance frequency of the crystal, Δm is the mass change, A is the piezoelectric active area, ρ_q is the density and μ_q is the shear modulus of the crystal. For a typical quartz crystal the density is $2.648 \cdot 10^6$ g/m^3 and the shear modulus is $2.947 \cdot 10^{13}$ g/m s^2 [30].

Several authors have performed EQCM studies on iridium oxide, see Ref [31–36]. EQCM studies are also available on ruthenium oxide [37] and ruthenium [38]. Further discussion of previous EQCM work is available in Chapter 4 and Chapter 6.

2.3 Redox couples

Redox couples, such as the hexacyanoferrate couple ($Fe(CN)_6^{-3}$ / $Fe(CN)_6^{-4}$ couple), have a stable potential in a given solution. As such they can be useful for probing the energy levels of an electrode. See for example Section 4.5 that discusses the use of redox couples to study AIROF electrodes. A nice introduction to the use of the $Fe(CN)_6^{-3}$ / $Fe(CN)_6^{-4}$ couple for studies of semiconductor electrodes can be found in the work of Berghe, Cardon and Gomes [27]. Other uses for redox couples can be to study the fraction of the electrode that is in use for a given electrochemical reaction [39].

2.4 Intercalation and electrochromism in oxides

Electrochromic oxides are materials that change their optical properties with changes in their potential. The most known electrochromic oxide is perhaps tungsten oxide, WO_3, that changes from a colourless or bleached state at anodic potentials to a blue-black colour at cathodic potentials. The first description of the electrochromism in WO_3, and likely also the first report where electrochromism is clearly defined, was made by Kraus in an unpublished report at Balzers AG in 1953 [40]. However Tronstad [41] observed changes in the optical properties of passive oxide layers on metals with changes in their potential in 1933 by the use of ellipsometry, though colour changes were not reported. Thus it was known that the optical properties of the oxide layer could change, but electrochromism was as such not described until 1953.

The electrochromic effect is associated with the insertion and expulsion of ions from the electrolyte into the oxide, MeO_n, as it is reduced and oxidised [40]:

$$MeO_n + xI^+ - xe^- \leftrightarrows I_xMeO_n \tag{2.10}$$

In the equation a cation, I^+, is used as an example, however an anion is also possible. The ion insertion or expulsion is necessary to maintain charge neutrality in the oxide layer upon oxidation and reduction of it. The insertion of ions into the oxide is called intercalation.

Iridium oxide differs from the majority of electrochromic oxides in that it changes to the coloured state with oxidation [42, 43]. Not all forms of iridium oxide are electrochromic. Anodically formed iridium oxide films (AIROF), an oxide layer electrochemically grown on iridium metal (see Chapter 4), is the best known example of electrochromic iridium oxide. However, also electrochemically deposited iridium oxide [31, 32] can show electrochromism, whilst iridium oxide powders do not [44]. Thus the crystal structure, the degree of crystallinity and the size of the crystallites determine if iridium oxide will be electrochromic.

2.5 Acid–base properties of oxides: The point of zero charge and the isoelectric point

The *point of zero charge* (pzc) and the *isoelectric point* (IEP) are measures of the acid-base properties of surfaces. The pzc is the pH at which the surface of the sample has zero charge in absence of specific adsorption of species other than water species (H^+ and OH^-). The IEP is the pH at which the surface charge is zero, also in the presence of specific adsorption [45, 46].

For a discussion of the connection between the oxygen evolution reaction and the pzc, see Section 3.6. Also for transition metal oxides some evidence of a connection between the pzc and the number of electrons in the unit cell per metal atom exists [47].

Several methods are available for determining the pzc or the IEP. Table 2.1 gives a brief description of the different methods presented here, including the typical

amount of oxide needed for the method in question. Ultimately the amount of oxide needed is dependent on the oxide being examined. It is worth noting that several of the methods require large amounts of oxide. This might not always be practical.

Table 2.1: Different methods for determining PZC.

Method	*Amount of oxide*	pH *range*	*Ref.*
Potentiometric Titration	20 g/l		[48]
Mass Titration	2 g	3–10	[49]
Potentiometric Mass Titration	15 g/l	> 4	[50, 51]
Differential Potentiometric Tit.	20 g/l	> 3	[52]
Immersion Technique	> 15 g	> 4	[53]
(Micro)Electrophoresis	mg range		[10]
Atomic Force Microscope	mg range		[54]

The titration techniques are based on titrating either an oxide suspension and comparing it with a sample without the oxide, or titrating oxide suspensions with different ionic strengths [48, 52]. Instead of varying the ionic strength the oxide concentration can be changed [50, 51], or distilled water can be "titrated" with the oxide [49].

The immersion technique was first described by Ahmed [53]. Several different solutions of an inert electrolyte, with different pH-values, are prepared. An amount of oxide is added to each solution and the change in pH is observed. The pzc is found at the pH that gives the smallest change in pH upon addition of oxide.

Electrophoresis is the movement of charged particles in a potential field. At the IEP the particle is not charged, hence it will not move in the potential field [10]. The measurement is carried out by varying the solution pH until the particles do not move. This pH is the IEP. Fully automated apparatus that can preform such measurements are commercially available.

An Atomic Force Microscope, AFM, can be used to find the pzc. The force measured between the probe of the microscope and the sample will change as a function of the pH of the surrounding solution. The pH at which the force has the lowest value is the pzc of the sample [54]. This method has been used for a wide variety of systems, particularly for oxides, see for example [55–58].

The pzc can be estimated from the electronegativity of the oxide, X_{ox}, using the Buttler–Ginley correlation [59]. The electronegativity of the oxide can be found from the Mulliken electronegativities of the metal and oxygen:

$$X_{\mathrm{ox}} = (\chi_{\mathrm{M}}^{\mathrm{n}} \cdot \chi_{\mathrm{O}}^{\mathrm{m}})^{1/(\mathrm{n}+\mathrm{m})} \tag{2.11}$$

The Mulliken electronegativity, χ, of an element is defined as the average of the electron affinity and the ionization energy of the element (available in for example Ref. [60]). In the equation the subscript M refers to metal and O to oxygen.

Chapter 3

Water electrolysis

Water electrolysis is by no means a new process. The first reported water electrolysis experiments, conducted by Taets van Troostwijk and Deiman, took place in the Netherlands in 1789 [61]. In an industrial scale, water electrolysis has over 100 years of history [62]. In Norway Norsk Hydro, now Yara, operated several large water electrolysis plants, the first large plant was opened in the 1920s [63].

Nowadays most of the hydrogen produced is from fossil fuels, manufactured via steam-reforming or petroleum cracking (for a brief discussion of these methods see Section 3.7 at the end of this chapter). For some applications the hydrogen produced from fossil fuels is not pure enough. Water electrolysis is therefore still used when high purity hydrogen is needed, or if the amount of hydrogen needed is not large enough to justify a steam-reforming plant. Today about 5 % of the world's hydrogen production is by water electrolysis [63].

Alkaline water electrolysis still dominates the market for water electrolysis. Small scale water electrolysis systems based on polymer electrolyte membrane (PEM) technology are available. High temperature solid oxide water electrolysis systems, often based on doped zirconium oxide as the electrolyte, are under development (not discussed further here). In addition large amounts of hydrogen (about 3 % of the world's production [63]) is produced as a byproduct, for example from the chlor-alkali industry.

3.1 Reaction mechanism

Water electrolysis is the process of splitting water into hydrogen and oxygen by electrochemical means. This is accomplished by applying a sufficiently large potential between the anode and the cathode, which are immersed in an aqueous electrolyte[1]. Oxygen gas will be evolved at the anode and hydrogen gas at the cathode.

The oxygen evolution is described by equation (3.1). Likewise hydrogen evolution is described by equation (3.2). The total reaction is given by equation (3.3).

[1] Or in the case of PEM water electrolysis water is fed to the anode and a polymer electrolyte is used

$$2H^+ + \frac{1}{2}O_2 + 2e^- \leftarrow H_2O \tag{3.1}$$

$$2H^+ + 2e^- \rightarrow H_2 \tag{3.2}$$

$$H_2O \leftrightarrows H_2 + \frac{1}{2}O_2 \tag{3.3}$$

The reactions at the anode and cathode can proceed by the means of intermediates, typically different adsorbed species [64]. Several different reaction mechanisms can be envisioned, Bockris [64] proposed five and Matsumoto and Sato [65] proposed four. As an example, two reaction mechanisms relevant for oxygen evolution from oxide electrodes are given below.

The oxide path [64]:

$$OH^- + M \leftrightarrows MOH + e^- \tag{3.4}$$

$$2MOH \leftrightarrows MO + M + H_2O \tag{3.5}$$

$$2MO \leftrightarrows 2M + O_2 \tag{3.6}$$

M is a metal site on the electrode surface.

The electrochemical oxide path [64]:

$$OH^- + M \leftrightarrows MOH + e^- \tag{3.7}$$

$$MOH + OH^- \leftrightarrows MO + H_2O + e^- \tag{3.8}$$

$$2MO \leftrightarrows 2M + O_2 \tag{3.9}$$

The Tafel slope, b_a, can give an indication of which mechanism and which rate determining step (RDS) is followed during a particular experiment. However some caution should be used when comparing theoretical Tafel slopes with experimental values. Among the complicating factors are that the symmetry factor, β, is not always 0.5. Semiconducting electrodes, like some oxide electrodes are, can be problematic as there might be a potential drop in the space charge layer of the electrode. This will give an erroneous value for the Tafel slope [65].

The hydrogen evolution reaction can be divided into three steps (for acidic solutions):

$$H^+ + e^- \leftrightarrows MH \tag{3.10}$$

$$2MH \leftrightarrows H_2 + 2M \tag{3.11}$$

$$H^+ + HM + e^- \leftrightarrows H_2 + M \tag{3.12}$$

The first step (3.10) is called the Volmer reaction, the second step (3.11) is called the Heyrovsky reaction and the last step (3.12) is called the Tafel reaction. The hydrogen evolution reaction can proceed either by step (3.10) followed by step (3.11) or step (3.10) followed by step (3.12).

3.2 Thermodynamics and kinetics

The thermodynamic data for reaction 3.3 at standard conditions is given in Table 3.1.

Table 3.1: Thermodynamic data for water electrolysis [66]

ΔH^0	286 kJ/mol
ΔG^0	237 kJ/mol
S^0	163 J/Kmol

The standard potential, E^0, for the reaction is thus (see also section 2.1):

$$E^0 = \frac{\Delta G^0}{n\mathrm{F}} = \frac{\Delta H^0 - T\Delta S^0}{n\mathrm{F}} = 1.228 \text{ V} \tag{3.13}$$

In the equation $n = 4$ is the number of electrons transferred in reaction (3.3), F is Faradays number and the temperature is T in Kelvin. At E^0 the reaction consumes electrical energy $W_{el} = \Delta G$ and heat $Q = T\Delta S$. The thermoneutral voltage, $E_{tn} = {}^{\Delta H}/_{n\mathrm{F}}$, is the voltage at which reaction (3.3) does not consume or produce heat [67]. At voltages above E_{tn} excess heat will be produced and a cooling system is needed, below this value heat needs to be supplied to the system to prevent cooling. However, this makes it clear that it is possible to reduce the electrical energy consumption by operating the electrolyser at a higher temperature if a heat source[2] is available. Pressurising the electrolyser might, however, be necessary to reap the full benefit of increasing the temperature [68, 69].

The kinetics and thermodynamic principles are discussed in general in the Theory chapter, see Section 2.1. Further discussion of the thermodynamics and kinetics of water electrolysis (mainly focused on alkaline water electrolysis) can be found in the works of LeRoy, Bowen and LeRoy [68] and LeRoy [69].

3.3 Alkaline water electrolysis

The traditional industrial method of hydrogen production by electrolysis is water electrolysis in an alkaline solution, typically 25–35 wt% KOH, at temperatures of 60–90 °C [62,70]. The anode is typically made of nickel and the cathode of steel, stainless steel or nickel. The latest trends for the electrodes are both morphological in nature, increasing the active area by increasing the roughness, and catalytic, by applying catalysts. The catalysts are often nickel based compounds with molybdenum on the cathode and cobalt or lanthan on the anode [71].

The cell design can be divided into two main types, a tank type and a filter press type [63, 70]. The tank type uses monopolar electrodes fitted in a tank. The monopolar system offers a rugged system with a simple design and construction at the expense of power consumption. The filter press type uses bipolar electrodes stacked together in a large number (several hundreds). The gap between the electrodes can be very narrow, reducing the ohmic loss in the electrolyte. The electrolyte

[2] This naturally makes most sense if waste heat can be used.

is pumped through the system. The filter press type offers a lower power consumption, but the system is more complicated both in fabrication and maintenance. Today the filter press system dominate the market.

For both cell types a separator is placed between the anode and cathode to prevent mixing of the produced gasses. Traditionally asbestos was used as a separator, however it has now largely been replaced by synthetic materials like polysulfones or oxide-ceramic materials such as barium titanate, calcium tiatnate or nickel oxide [63].

The electrolyser can be pressurised. The Lurgi company[3] produces a filter press type of water electrolyser that operates at 32 bar. One advantage of pressurising the electrolyser is that a compressor to pressurise the products for storage is often not needed. Also the gas bubbles in the electrolyte occupy a smaller volume reducing the ohmic losses in the system. The net effect is that the energy consumption compared to atmospheric units is not that much higher despite the products being delivered at a higher pressure [63]. However, the construction of the system is more complicated.

The overall energy efficiency of a modern alkaline water electrolysis system is 70–80 %, with a current efficiency above 98 %. The electrical energy consumption per normal m^3 H_2 is in the range of 4–5 kWh. The purity of the produced gasses are typically higher than 99.8 % for hydrogen and 99.6 % for oxygen [63, 70].

A recent review by Zeng and Zhang is available for further study [71].

3.4 PEM water electrolysis

PEM water electrolysis is a newer method than alkaline water electrolysis. The General Electric Company developed the PEM[4] water electrolysis system from the nineteen fifties and onwards. The liquid electrolyte was replaced with a solid polymer Nafion®. Nafion® is a proton conductive polymer based on perfluorosulfonic acid [63, 70, 72]. Later several studies have been published investigating PEM electrolysers, see for example [67, 72–81].

A PEM system consists of a stack of several membrane-electrode assemblies separated by a current collector that allows transport of reactant water and the produced gasses. The current collector must be stable during operation. A gas diffusion layer next to the electrode allows the reactants to be transported to the electrode-membrane interface and the products to be transported away. The gas diffusion layer also allows current to flow to and from the electrodes. Porous titanium is often used as the gas diffusion layer on the anode side and carbon cloth on the cathode side [70]. Figure 3.1 shows the membrane-electrode assembly. The cathode catalyst is typically based on platinum, often supported on carbon. Ruthenium and iridium oxide are common choices as anode catalyst, see Section 3.5 and Section 3.6.

Compared to an alkaline water electrolysis system a PEM system offers several advantages: The current density is much higher, up to 2 A/cm^2. The power consumption can be lower than alkaline systems. In laboratory systems a cell voltage of 1.567 V at a current density of 1 A/cm^2 and a temperature of 80 °C was

[3] Now Industrie Haute Technologie SA, http://www.iht.ch/

[4] At that time referred to as the Solid Polymer Electrolyte (SPE).

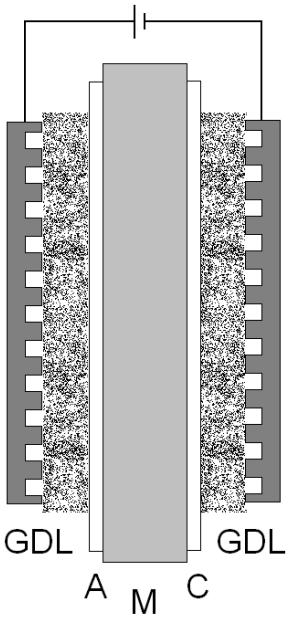

Figure 3.1: The membrane-electrode assembly of a PEM water electrolyser. Legend: GDL: Gas diffusion layer and current collector, A: Anode, M: Membrane and C: Cathode. In a stack the current collector would be symmetrical, with fluid transport channels on both sides.

reported [82]. This gives a power consumption of 3.75 kWh per normal m^3 H_2.

In contrast to the alkaline systems it is not necessary to pump an alkaline liquid through the system. Pure water (or steam) is supplied directly to the cell. The higher current density also makes it possible to build the system more compact. Use of a membrane electrolyte results in higher gas purity than in alkaline systems, also pressurisation up to 150 bar can be achieved [72].

A recent EU project, the GenHyPEM (Générator d'Hydrogène par électrolyse de l'eau PEM) [80] demonstrated PEM water electrolysis systems producing between 0.1 and 5.0 Nm^3/h of H_2. Stable performance was obtained at current densities of 1 A/cm^2 at pressures up to 50 bar. Single cell efficiencies of 72 % and stack efficiencies of 65 %, at current densities of 1 A/cm^2, was shown.

3.4.1 Stability

Andolfatto and co-workers [78] studied the long term stability of a PEM water electrolyser using different catalysts and water cleaning techniques. Stable operation was found over 6000 hours for a system containing titanium GDL and IrO_2 catalyst, both for the anode and cathode. Poisoning of the catalysts and membranes by metal ions from dissolution of the construction materials is suggested to be an important factor in deactivation. The membrane conductivity drops when protons are exchanged by metal ions, giving higher ohmic resistance in the cell. As such the feed water must be cleaned of metal ions. The same problem was observed by Millet *et al.* [79]. Other investigations have shown operation times of 5000 hours [74] and up to 15000 hours [75] without irreversible degradation.

The stability of PEM water electrolysis systems used for non steady state operation is often reported as being better than that of the traditional alkaline systems. For the GenHy®5000 water electrolyser, capable of producing 5.0 Nm^3/h of H_2, intermittent operation was not found to affect the performance degradation during the first 5000 h of operation [80].

3.5 Catalysts for the hydrogen evolution reaction

The catalyst choice for the hydrogen evolution reaction depends on the type of electrolyser. In alkaline systems steel or nickel is used, as mentioned above. Non noble metal alternatives are often based on cobalt or metal hydrides. For example a $NiCo_2O_4$ catalyst bound with Teflon gave 13000 A/m^2 at 1.63 V in 5 M KOH at 70 °C [83]. The remaining discussion will be focused on catalysts for PEM systems. For the hydrogen evolution on the cathode in a PEM water electrolyser platinum catalysts are preferred.

Section 3.1 should make it clear that the binding energy of hydrogen to the metal will influence the hydrogen evolution reaction as the intermediate of the reaction is hydrogen bonded to metal. If the binding energy is high the first partial reaction, step (3.10), will proceed quickly, but the desorption of hydrogen, step (3.11) or step (3.12), will be slow. The overall reaction will thus be slow. The opposite situation, a low binding energy, will make the desorption quick, but the initial formation of the intermediate slow, thus the overall reaction will be slow. The ideal catalyst for the hydrogen evolution reaction has an intermediate binding energy for hydrogen. This is formalised in a "Volcano-plot" [84]. The "Volcano-plot" plots the binding energy of hydrogen to the metal against the exchange current density for the hydrogen evolution reaction on the same metal. The plot derives its name from the volcano like shape of it. The plot clearly shows that high or low binding energies give lower exchange current densities compared to intermediate values. Platinum is at the top of the curve.

3.6 Catalysts for the oxygen evolution reaction

A significant energy loss in PEM water electrolysers can be found on the anode, i.e. on the oxygen evolution electrode [8]. Improving the catalyst on the anode will thus improve the efficiency of the electrolyser. Reducing the cost of the catalyst, either by using cheaper materials or reducing the loading, is also desirable. However, as the cost of the hydrogen produced is dominated by the cost of electricity, which amounts to about 70 % [72], increasing the efficiency is of a higher importance than decreasing catalyst cost.

On the anode side the conditions are strongly oxidising and most metals will oxidise. As such, conductive oxides are appropriate as catalysts [65]. Noble metal oxides with rutile crystal structure, for example ruthenium and iridium oxide, are active for the OER. For application in PEM electrolysers the catalyst is normally used in powder form.

The reaction paths for the OER, see Section 3.1, makes it obvious that the oxygen evolution reaction involves a step with an oxygen atom bound to a metal atom. The binding energy of oxygen to metal is thus important for the OER. In a manner similar to the one used for hydrogen evolution, "Volcano-plots" can be constructed for the OER [85]. The plot shows how the exchange current density for the OER changes with the energy for the transition between the lower and higher oxide state. The oxides that oxidise easily are poor catalysts as the intermediate are strongly adsorbed. Oxides that do not oxidise with ease are also poor catalysts as the intermediates are slow to adsorb. The ideal catalyst has intermediate energies for the lower to higher oxide transition. RuO_2 and IrO_2 lie near the peak of the volcano. Recently these results have been confirmed for some of the oxides by density functional theory (DFT) calculations [86–89]. Unfortunatly Hansen *et al.* [89] found that the overpotential for the OER will be high on all oxides as three intermediates are involved in the OER. The binding energy for each of the intermediates is such that a single material that binds them optimally can not be found.

Tseung and Jasem [83] and later Rasiyah and Tseung [90] took departure in a similar thought. They compared the potential for the lower to higher oxide state transition to the potential for the OER in 5 M KOH. An excellent correlation was found. The best catalysts, iridium oxide, ruthenium oxide, nickel oxide and cobalt oxide, evolve oxygen after undergoing a transition between a lower and a higher oxide state. A different group of oxides were found that evolve oxygen at a potential close to the OH^-/HO_2^- couple. Oxides that have a stable electronic configuration and do not readily undergo further oxidation (for example PbO_2) or oxides with a transition at a high potential (for example PtO_2) belong to this group.

The acid base properties of the oxide, as expressed by the point of zero charge (pzc), has also been suggested as a method of predicting and explaining electrocatalytic activity towards the OER [59, 91, 92]. The thought behind is that the acid base properties are determined by the adsorption of water species (H^+, OH^-, etc.). The same species can be intermediates in the OER. Thus the adsorption properties of the intermediates will influence the reaction rate, as discussed above. Also DFT calculations have shown that there is a linear trend between the binding energy of oxygen and various surface species [86], further strengthening the presumption that the pzc and the activity towards the OER are connected. For comparison of catalysts it is also convenient that the pzc is an intrinsic parameter; differences in surface area does not influence the comparison. Comparison between the pzc of physical and chemical mixtures of nickel and cobalt oxides was studied by De Faria and co-workers [93, 94]. The actual pzc measured for physical mixtures seems to be dependent on the electrochemical surface area of the pure oxides, and not the molar, weight or dry surface area (BET) fraction.

A review of transition metal oxides for OER, including experimental data for Tafel slopes and overvoltages, is available in Ref [65]. The authors found that the activity for the OER was, in decreasing order: "RuO_2, IrO_2, Co and Ni containing oxides and finally Fe, Mn and Pb containing oxides."

Iridium metal is sometimes used as an oxygen evolution catalyst [73,80], however there is little doubt the iridium metal will quickly oxidise during operation giving iridium oxide. Platinum is not appropriate as an anode catalyst as platinum oxide

does not have the necessary conductivity.

The deactivation mechanism of the oxygen evolving electrode depends on the oxide catalyst in use and the operational conditions. In acidic media RuO_2 dissolves during the OER, rendering it unsuitable for practical applications, although adding iridium will improve the stability [95, 96]. Other deactivation mechanisms can be poisoning, detachment of the catalyst from the electrode or deactivation as the result of problems with any possible catalyst supports [95, 96].

3.7 Other methods of hydrogen production

As mentioned in the introduction to this chapter water electrolysis is responsible for a small part of the world's hydrogen production. The bulk of the hydrogen is produced by reforming. Steam reforming is the dominant technique with partial oxidation and autothermal reforming emerging as techniques useful for hydrogen production *in situ* in a vehicle [97]. Steam reforming is conducted at high temperatures and elevated pressure. A general reaction for steam reforming is given in equation (3.14). The produced CO is converted to more H_2 in a water-gas-shift reactor, see equation (3.15). For use in fuel cells the other purification steps are also needed, including removing sulphur and CO left over after the water-gas-shift reaction.

$$C_mH_n + mH_2O \leftrightarrows mCO + (m + {}^n/_2)H_2 \tag{3.14}$$

$$CO + H_2O \leftrightarrows CO_2 + H_2 \tag{3.15}$$

Hydrogen can be produced from a wide selection of biomass, for example from fast growing crops or waste from forestry and agriculture, by thermal decomposition or steam reforming. Algae or bacteria can produce hydrogen given the right conditions, either by using sunlight as an energy source or in the dark using the carbohydrates in the biomass as the energy source [97].

At temperatures above 2500 °C water decomposes. However the material challenges in building a system that can operate at these temperatures and also finding a renewable heat source render direct decomposition of water difficult. By clever use of chemical reagents a cycle can be set up that splits water at lower temperatures. This is called thermochemical water splitting [97].

Water can be directly split into hydrogen and oxygen by sunlight, known as photoelectrolysis [97]. Semiconducting materials are used for either both anode and cathode or only one of them. Sunlight excites electrons in the semiconductor giving a photocurrent analogous to that in a solar panel for electricity production. The photocurrent is used directly to split water into hydrogen and oxygen.

Chapter 4

Anodically formed iridium oxide films

4.1 Introduction

Anodically formed iridium oxide films (AIROF) is an electrochemically grown oxide film on iridium metal. AIROF electrodes have been used in three of the articles presented in Part II of this thesis. As an introduction to those articles this chapter gives a review of the available literature on AIROF[1].

Some of the first reports on AIROF is from the sixties and seventies [98–103]. An increasing current in the anodic region with potential cycling on iridium electrodes was noted, but the cause of this was not understood. The first assumption was that the oxide formed in the anodic scan was completely reduced in the cathodic scan [101, 102]. Rand and Woods [100] did not agree as they noticed that the charge in the hydrogen region decreased with potential cycling. Thus, they argued, the exposed metallic area must be reduced with the potential cycling. Surface roughening, caused by the potential cycling, could not either be the explanation for the increase in charge in the oxide region as the hydrogen charge decreased. The irreversible formation of an oxide layer was suggested by Buckley and Burke [103] in 1975.

4.2 Manufacture of AIROF

All the first reports of the manufacture of AIROF used potential cycling to grow the oxide film on iridium metal electrodes. Otten and Visscher published two papers [101, 102] in 1974 dealing with the preparation of AIROF by potential cycling on an iridium foil. When cycling between 0 and 1400 mV they observed that both the hydrogen peaks and the oxygen peaks grew. The hydrogen peaks did not continue to grow after about 80 cycles, whilst the oxygen peaks continued to grow also after 80 cycles. The oxygen coverage of the electrode increased almost linearly with the number of cycles. Oxide reduction peaks were observed at 950 mV and 750 mV

[1]The use of AIROF in the medical field, for example as electrodes for neural stimulation, is outside the scope of this chapter and will not be covered.

when cycling up to 1400 mV. Cycling up to 1500 mV or oxidising the electrode at 1600 mV also gave an oxide reduction peak at 1350 mV. Later Buckley and Burke [103] reported much the same as Otten and Visscher [101, 102]. However, they also reported that the increase of charge with potential cycling is not a simple surface roughening, but the continuous irreversible growth of an oxide layer. Potential pulsing between the same potential limits as used during potential cycling is a quicker way of growing AIROF [104].

The mechanism for the growth of the oxide layer is suggested to be the initial formation of a compact oxide layer. The outer monolayer of this is oxidised and becomes hydrated at potentials above 1.2 V. Further oxidation of the compact layer is inhibited by the hydrated layer, only one monolayer of hydrous oxide can be formed at a constant potential [104]. Unlike ruthenium oxide that can be grown potentiostaticly at potentials over 1.45 V [105], AIROF does not develop by holding it at a constant potential. By cycling the potential the compact oxide layer is reduced and reformed, only the hydrated surface layer remains after each cycle. This builds up as a hydrous oxide layer [104]. The oxide film grows at the metal to metal-oxide interface [106]. The upper and lower limit of the potential cycle, that must be exceeded for the film to grow, are about 1.15 V and 0.30 V. About half the Ir atoms in the surface atomic layer can be converted to hydrous iridium oxide during one cycle or pulse [104].

Some iridium is dissolved during oxide film formation, and the electrolyte can in some cases be coloured by this [105]. The mass loss during growth has been confirmed by quartz crystal microbalance (EQCM) measurements [34]. However the oxide growth is not a dissolution–redeposition process, as shown by the equal growth rate on a rotating disc electrode at 0 rpm and 4000 rpm. A study by Pickup and Birss [107] showed that the dissolution of the oxide during growth is much less in $LiClO_4$ solutions than in H_2SO_4 solutions, higher growth rates of the oxide could thus be achieved in $LiClO_4$ solutions. In addition the films grown in $LiClO_4$ have a higher mechanical stability and appear to be less hydrated than films grown in H_2SO_4 solutions. However the growth rate of the oxide is higher in sulphuric acid than it is in perchloric acid [108]. Mozota and Conway [109,110] studied the growth rate in a wider range of solutions and found that growth rate decreases in the order: 0.5 M H_2SO_4 > 0.5 M $HClO_4$ $\gg$ 0.5 M Na_2SO_3 $\gg$ 0.5 M NaOH.

Kötz and Neff [111, 112] followed the formation of AIROF on an emersed[2] electrode with Ultraviolet Photoemission Spectroscopy (UPS) in perchloric acid. The oxide formation starts at a potential of 0.6 V versus SCE. Oxide formation on Ir was found to be directly associated with increasing adsorption of ClO_4. The features of the UPS data that reflect the oxide formation during the first anodic scan are still present after scanning the potential back to 0 V versus SCE, confirming that the oxide formation is irreversible.

The solution the AIROF electrode is prepared in affects the growth of the oxide layer, both with respect to pH and type. Higher pH values gives a lower growth rate, and at pH > 3.5 the growth rate is almost negligible [113]. The role of ions (H^+, Li^+, K^+, Na^+, OH^- and F^-) in the growth of the oxide film was studied by

[2]Not immersed! This is an *ex-situ* investigation.

Pickup and Birss [114]. Chloride ions in the solution AIROF is to be prepared in hinders the growth of the iridium oxide layer [115]. Also the structure of the oxide film is dependent on the solution it was prepared in [116]. The extent of cracking of the film, as seen by SEM and ellipsometric analysis, depends on the preparation solution. Films grown in sulphuric acid appear more cracked than films grown in perchloric acid. The thickness of the film is, however, the same [116]. Finally the growth and redox kinetics of AIROF electrodes in sulphuric and *p*-toluen sulfonic acid was studied by Bock and Birss [117]. The charge transfer reactions were 10 times faster for films grown in sulphuric acid solutions, although the shape of the CVs recorded in the two electrolytes were quite similar.

The growth of AIROF in alkaline solutions was studied by Burke and Scannell [118] (NaOH solutions) and Kapałka and co-workers [119] ($NaClO_4$ solutions). It is possible to grow a hydrous iridium oxide layer in a dilute base (0.1–0.5 M NaOH), but not in a strong one (1.0 M NaOH) [118]. The growth rate per cycle declines with the number of cycles. Higher sweep rates increases the growth rate. Sweep rates above 2.0 V/s gives the largest growth after a fixed number of cycles. The optimum temperature for growth appears to be 40 °C. The stability of the oxide films grown in base are lower than the acid grown films. Transferring them to an acidic solution results in detachment of the film from the base metal and the dissolution of the film. At high sweep rates the anodic sweep in cyclic voltammograms recorded in dilute base show signs of acid response. This can be attributed to the local pH change in the porous film caused by the release of protons during the anodic reaction, thus an acidic environment is created within the porous film layer. This is not observed in strong alkaline solutions, perhaps explaining why oxide films can not be grown in strong alkaline solutions. Acid grown films do not show local pH changes, possibly do to the more open texture of the acid grown films.

In a two part study Mozota and Conway [109, 110] studied the monolayer stage of the iridium oxide growth, the transition to the reversible multilayer oxide film and finally the thick multilayers conductivity switching behaviour. Careful control of the anodic limit in cyclic voltammograms can be used to avoid hydrous oxide growth. Underpotential deposition of OH-species starts at a lower potential than on gold or platinum. The growth rate of the oxide film was found to vary with the solution. In the reduced state only the unblocked iridium surface is available for electrochemical reactions, this explains why the current for the H reactions does not increase with increasing oxide layer thickness. The only double layer charging is the charging of the unblocked iridium surface. When the electrode is oxidised, the oxide becomes conductive. Now the oxide takes part in the electrode reactions, the current will therefore increase with increasing oxide layer thickness.

The finished oxide film typically has a cracked structure (dried-out mud) [105, 120] although porous and less cracked films are reported by some [2].

A nice review of how to find the thickness of an iridium oxide film can be found in the work of Elzanowska and Birss [121]. The charge passed during a slow potential scan between 0 V and 1.236 V is used to represent the thickness of the film as a charge enhancement factor (CEF). The CEF is the ratio of the charge for the oxide layer compared to the charge passed during the first potential scan (about 0.11 mC/cm^2). Furthermore a monolayer of oxygen corresponds to a thickness of

about 0.3 nm [101, 102] and one monolayer will give a charge of 0.544 mC/cm^2. A film thickness of 295 nm gave a charge capacity of 23.0 mC/cm^2 [122].

The actual thickness of the oxide film can be found by ellipsometric and reflectrometric measurements [42,123]. 200 cycles between 0–1.5 V in 0.5 M H_2SO_4 gives a film close to 2500 Å. Also it was found that the oxide film at a potential of 1.4 V is 10–15 % thicker than the same film at 0.25 V. Michell, Rand and Woods [124] studied the film thickness by finding the weight of the film and using the density for bulk IrO_2. After 200 cycles to 1.5 V in 1 M sulphuric acid the film was 6.5 nm and after 3600 cycles the film thickness had increased to 22 nm. The change in the film's light reflectance can not be explained by the small change is thicknes, thus confirming that it is a change in the films absorbance that is responsible [123].

McIntyre and others [122] found that the density of the oxide film is 2.0 g/cm^3 (compared to 11.68 g/cm^3 for anhydrous bulk IrO_2).

It is also possible to make composite films of AIROF and polyaniline [125]. It is not possible to form the composite film simultaneously, one must first form the iridium oxide film and then deposit polyaniline in its cracks as the adsorption of polyaniline hinders the oxide formation. The composite films show a pseudocapacitance much higher than for an AIROF film and also very fast kinetics.

Transferring the AIROF electrode to a different electrolyte, than the one the film was grown in, should be approached with some caution as the studies of Birss *et al.* [105], Bock and Birss [120] and Lee *et al.* [126] show that the AIROF electrode can crack and possibly expose Ir metal to the electrolyte upon such transfer. Cracking might also happen during potential cycling.

4.3 The properties and structure of AIROF

Electrochromism in AIROF was reported by Gottesfeld and co-workers [42, 43]. When the oxide film reaches sufficient thickness, the film changes colour to blue-black upon oxidation (potentials above about 1 V), and returns to a transparent state after reduction. The time for colouration of a 170 nm film stepped from 0 V to 1 V was found to be 40 ms [42]. However, when the oxide film gets too thick (CEF 150–200) anodic colouration is not observed, the film stays black at all potentials [110].

The anodic colouration of the film corresponds to a change in the oxidation state of Ir from III to IV [122, 127]. During colouration and bleaching the ions required to maintain charge neutrality can come from: bound H_2O and OH-groups on the oxide surface, free H_2O in the electrolyte within the film pores, hydrated H^+ species in the bulk electrolyte and other ions in the solution. There is not enough adsorbed species to fully satisfy the charge neutralisation requirements.

The reactions of iridium oxide in aqueous solutions can be written as [121]:

$$(IrO_2 \cdot nH_2O)_5 + 5e^- + 7H_3O^+ + 2X^- \leftrightarrow [Ir_5O_3(OH)_7 \cdot 5nH_2O]^{2+} \left(X^-\right)_2 + 7H_2O \quad (4.1)$$

$$M_3^+ [Ir_5O_{10}(OH)_3 \cdot 7H_2O]^{3-} + 5e^- + 7H_2O \leftrightarrow M^+ [Ir_5O_6(OH)_4 \cdot 10H_2O]^- + 2M^+ + 7OH^- \quad (4.2)$$

where equation (4.1) is the reaction in acidic solutions and equation (4.2) for alkaline solutions. X^- is an anion in the solution and M^+ is a cation.

The pH effect on AIROF was studied by Burke, Mulcahy and Whelan [113]. The potential of the main anodic and cathodic peak was found to decrease with increasing pH. The oxygen evolution potential exhibited a traditional behaviour of -59 mV per pH unit. Both phosphate and sulphate solutions gave these results. The open circuit potential of the oxide film changed almost linearly from pH = 0 to pH = 13 with a slope of -78 mV per unit pH in a phosphate solution. The slope changed slightly in different solutions. The pH dependence has also been proposed to be -68 mV per pH by Birss, Elzanowska and Gottesfeld [34]. This is in contrast to thermally prepared iridium oxide electrodes (DSA-type) that show a dependence of -64.5 mV per unit pH in a phosphate solution [113]. The pH dependence has been found to be independent of the acid solution (sulphuric, nitric or perchloric acid) the film was grown in [34]. However the solution appears to influence the Ir(+III)/Ir(+IV) reaction stoichiometry [34].

The solution pH also affects other properties of the oxide layer. Yuen, Lauks and Dautremont-Smith [128] conducted a voltametric study as a function of pH. The potential of the peaks in a CV change, a dependence of 85 mV per pH unit was found for the main anodic peak. Pickup and Birss [114] gave the potential of the main anodic peak, as a function of pH, as: $E^o(pH)$ / V vs SHE $= 0.93 - 0.089 \cdot pH$. Changes in the pH of the solution inside of the film during oxidation and reduction might make this equation hard to use in near neutral solutions. The charge of the oxide (both reduced and oxidised form) changes with pH [114]. The reduced oxide is cationic at pH 2, approximately neutral at pH 7 and slightly anionic at pH 13. The oxidised form is neutral and slightly anionic between pH 2 and pH 9 and is significantly anionic at pH 13.

In dilute perchloric acidic solutions, less than 50 mM $HClO_4$ in 1 M $NaClO_4$, the response of the film is primarily determined by the diffusion of H^+ in the electrolyte phase [129]. A similar response was observed in H_2SO_4/Na_2SO_4 solutions, however the ions involved seemed to be HSO_4^-. Furthermore the response in more concentrated sulphite solutions was significantly slower and much more dependent on the H^+ concentration than in perchloric acid solutions.

Buckley and Burke [103] investigated the effect of chloride on AIROF electrodes prepared in chloride free solutions. No effect was found for chloride concentrations of 0.04 M.

Kapałka and co-workers [119] found a peak separation between the main anodic and cathodic peak of 750 mV in an ammonia and sodium perchlorate solution with a pH of 9. This is much larger than what is observed in acidic solutions. The reason for this is not irreversibility, as one might expect, but local pH changes inside the oxide film. A pH change inside of the film of up to 10 units is expected. The addition of ammonia buffers the solution inside the oxide film and reduces the peak separation to about 100 mV.

Frazer and Woods [106] determined the relationship between the oxygen evolution rate and the amount of oxide on the iridium surface. An approximate linear relationship between the amount of oxide and the activity was observed. The stability of AIROF films for the OER over an hour long period was examined by galvanostatic

polarisation and CVs by Čukman and Vuković [130]. An increase in the potential after some 30 minutes coincides with the CV of the film changing to that of an iridium electrode with a single monolayer of oxide. Anodic polarisation to potentials above 1.65 V can result in complete removal of the oxide film [19,105,123,131]. This was confirmed by ellipsometri, the values obtained at 1.25 V were within 0.2 % of the value obtained on the fresh Ir-electrode [123]. Impedance measurements also confirm the loss of the outer oxide layer if the AIROF electrode is submitted to OER at potentials above 1.6 V [19]. AIROF is quite stable at 1.55 V [105], however holding the film at 1.55 V prevents further development of the film, possibly do to ageing.

EQCM measurements of the oxidation and reduction of hydrous iridium oxide electrodes have been performed by Birss and others [34]. The mass change of the electrode in a single potential sweep was found to vary linearly with the oxide film charge density. It was found that the mass of the iridium oxide film increased by about 6 g when 1 mole of Ir sites are reduced in an sulphuric acid solution. Since the mass of the electrode decreases during oxidation, protons are thought to be involved in the reactions. OH^- ions would have given a mass increase. It is proposed that the reduction involves the injection of 1.5 moles of H^+ and 0.25 moles of SO_4^- and the expulsion of one mole of water per mole of Ir sites. This would correspond to a mass change of 7.5 g. A later study by Bock and Birss [35] suggested slightly different values, with the injection of 1.15 H^+ and 0.15 HSO_4^- and the expulsion of 0.6 H_2O per e^-. In alkaline solutions the mass change is the opposite of that observed in acids, the mass change is also smaller, between 3 and 4 g per mole of Ir sites [34]. In near neutral solutions alkali metal ion insertion might occur during the reduction of the oxide if the alkali metal ion concentration is significantly higher than the H^+ or OH^- concentration [114].

Interestingly Bock and Birss [35] found that the mass change between the reduced and oxidised form of AIROF film was greatest in a 0.6 M $HClO_4$ solution (12 g/mol), followed by a 0.4 M HNO_3 solution (6.5 g/mol) and smallest in a 0.4 M H_2SO_4 solution (5.5 g/mol). The amount of water involved during the reduction and oxidation reaction is suggested to be part of the cause. In $HClO_4$ and HNO_3 only 0.2 mol of H_2O per e^- are expelled compared to the 0.6 mol in H_2SO_4. Also it was found that the mass changes between the oxidised and reduced form of the oxide was influenced mainly by the solution used to study the oxide, and almost independent of the growth conditions (growth solution and potential cycling or pulsing).

The kinetics of charging and discharging of iridium oxide films in aqueous and non-aqueous media was investigated by Pickup and Birss [132]. The oxidation and reduction reaction is not reversible. As a measure of the kinetics of the anodic peak the scan rate, ν_o, at which the voltammogram changes from being reversible to being kinetically limited is used. For 0.1 μm thick films $\nu_o = 0.74$ V/s. Increasing the film thickness decreases ν_o. The potential of the main peaks (A_1/C_1) is not dependent of the sweep rate (at least up to 1 V/s) for thin films [36]. For thicker films sweep rates lower than 0.1 V/s gave diffusion control. From chronocoulometry the diffusion coefficient for the charging and discharging of the oxide film can be found [132]. The diffusion coefficient for potentials below and above 0.71 V differ by one to two orders of magnitude. This indicates that the charging and discharging

of the oxide is limited by the electronic conductivity at low potentials since the conductivity of the reduced film is less than the oxidised film. In acetonitrile about 35 % of the oxide sites charged and discharged faster, about one order of magnitude, than the remaining sites.

In aqueous solutions Aurian-Blajeni *et al.* [133] found that for the reduced film the electronic conductivity was the controlling factor for the rate of charge transfer, whilst in the oxidised film it might be proton diffusion. Furthermore the impedance results can be modelled by an equivalent circuit containing a double layer capacitor in parallel to a series consisting of a charge transfer resistance, a constant phase element and finally a capacitor and a resistance in parallel. The impedance response is a combination of two main effects [134]: The diffusion of the proton-electron couple in the film and the transport of solution ions into and out of the pores of the film to compensate for the charge of the film.

Further impedance measurements were conducted by Glarum and Marshall [129]. They investigated the effect of the thickness of the film, the pH and the potential on the impedance of iridium oxide. The capacitances found by cyclic voltammetry were larger than those found from impedance measurements. The difference was reduced in dilute solutions and by changing from sulphate to perchloric solutions.

The effect of ageing iridium oxide electrodes in acidic and alkaline solutions was determined by Elzanowska and Birss [121]. Ageing the electrode in the reduced state, or preforming very slow potential sweeps, in an acidic solution gave a positive shift in the anodic peak positions and a reduction, up to 50 %, of the reaction kinetics. The effect of ageing could be reversed by potential cycling or holding the electrode in the oxide region for a brief time (one minute). In alkaline solutions no ageing was observed. The effect of ageing was suggested to be the loss of water from the film in acidic solutions at negative potentials which inhibits the ion/solvent transport processes in the film.

The valency and structure of iridium in anodic iridium oxide films were determined by Hüppauff and Lengeler [135]. They used X-ray absorption spectroscopy in their investigation. The valency, v, of Ir in AIROF varied between 3.0 and 4.8 in a voltammogram cycle. In addition the first coordination shell around an iridium ions shrinks from 0.203 nm at $v = 3.0$ to 0.191 nm at $v = 4.8$, whilst at the same time a strong spread in the interatomic distances in the first coordination shell was observed.

The actual crystallographic structure of AIROF can be challenging to find as the film is quite thin. Also, as thick films do not show electrochromism [110], producing a thick film for crystallographic studies might not give relevant results. Michell, Rand and Woods [124] used electron diffraction to find that the structure of a AIROF layer was hexagonal.

The data available on the temperature effect on AIROF is scarce. Cruz, Otero and Zañartu [136] describes the temperature effect in 0.5 M H_2SO_4 for temperatures between 20 °C and 70 °C. The growth rate of the oxide layer was found to increase up to temperatures of 50 °C. At higher temperatures it decreases, perhaps do to the increased dissolution rate of the oxide. Cycling of the electrode at 70 °C also leads to a decrease in the oxide charge. With increasing temperature the CV changes. The main anodic peak does not change, but the anodic prepeak does. The anodic

current at potentials above the anodic main peak increases, as do the currents in the hydrogen region. The potential and current of the main cathodic peak decreases with increasing temperature. An additional peak, cathodic to the main cathodic peak, appears at higher temperatures.

Pickup and Birss [137] conducted a study of the electrochemistry of iridium oxide films, grown in aqueous solutions, in non-aqueous solutions. Both acetonitrile and propylene carbonate was used with $LiClO_4$ as the supporting electrolyte. In addition tetrahydrofuran with 1 M $LiBF_4$ and 1,3-dioxolane with 1 M $LiBF_4$ were used as electrolytes. The film was electrochromic in all solutions.

Comparing the reaction rate of the Ir(+III)/Ir(+IV) transition in films grown in sulphuric and *p*-toluen sulfonic acid by electrochemical impedance spectroscopy show that reaction rate is up to 9–12 times higher in sulphuric acid [117]. The reaction rate difference can not be caused by film thickness effects as the thickness of the films grown in sulphuric and *p*-toluen sulfonic acid was the same [116]. Morphological differences are suggested to be the cause of the different reaction rates.

Vuković [131] conducted a study comparing the electrochemistry of hydrous iridium oxide films with that of heat treated anhydrous iridium oxide films. Heat treatment was carried out in air for one hour at temperatures between 473 K and 773 K. The electrodes had a lower charge after heat treatment than before heat treatment, however the charge of the heat treated electrodes could be restored by potential pulsing in the electrolyte. The heat treated electrode appeared to be more stable, although this stability was lost when the electrode was rehydrated.

The AIROF electrodes have been compared with reactively sputtered iridium oxide films (SPIROFs) by Yuen, Lauks and Dautremont-Smith [128]. SPIROF gives a different CV than AIROF; the peaks are broader than the peaks in AIROF and there is no irreversible anodic peak. Furthermore the SPIROF electrodes show a normal nernsitan behaviour with respect to pH.

4.4 The prepeak

The prepeak, i.e. the small peak often found before the main anodic peak, has received a lot of attention [36, 136, 138]. The exact origin of the prepeak is still debated. As the experimental parameters, solution pH, oxide film thickness and the potential limits affect the kinetics of the oxidation and reduction of AIROF electrodes [138], one must be careful when choosing the experimental parameters. For example, if the lower potential limit in CVs is above 0.2 V, the position of the prepeak gets a positive shift and can merge with the main peak. Thus the prepeak can not be studied.

Gottesfeld and co-workers [139] believe that conductivity changes in the AIROF electrode is the cause of the prepeak. The poor conductivity of AIROF at low potentials only allows a small rate of oxidation seen as the anodic prepeak. When the potential is further increased the conductivity increases giving a fast oxidation of the remainder of the film seen as the main anodic peak. Elzanowska *et al.* [138] does not agree. The reason for this is that conductivity changes can not predict the merging of the prepeak with the main peak when the sweep rate is increased, nor

can it explain the different behaviour of the prepeak in different electrolytes.

The other explanations for the prepeak are based on there being separate reaction sites that are responsible for the prepeak. These are different from the ones that are responsible for the main peak. The origin of the sites responsible for the prepeak might be explained by the following reasoning [36]: When the electrode is swept to a potential below 0 V, hydrogen evolution occurs. The hydrogen evolution will occur close to the iridium surface do to the low conductivity of the film in the reduced state. Hydrogen evolutions consumes protons or water and forms an alkaline environment. The oxide film close to the iridium surface might thus be partially dehydrated and structurally altered giving rise to a different electrochemical response. This idea is further supported by the fact that when transferring the AIROF electrode from one solution to the other, the main peak characteristics equilibrate immediately whilst the prepeak characteristics equilibrate much slower, only after several cycles in the full potential range (0–1.4 V or larger). This is interpreted to mean that the sites that react in the prepeak are deep within the film [136,138], i.e. close to the iridium metal surface.

The position of the prepeak shifts in the positive direction with increasing film thickness [36, 129], in contrast to the main anodic peak that does not shift with cycling. The cathodic equivalent to the anodic prepeak can only be seen for very thin films. Both the anodic and the cathodic prepeak show a pH dependence of -80 mV per pH unit, slightly higher than the main peaks pH dependence.

The kinetics of the prepeak are usually reported as being slow [138]. The prepeak is also considered to be irreversible whilst the main anodic peak is reversible [129]. The reaction stoichiometry is different from the main peak reaction. Mass changes measured by EQCM show that the water exchange and the involvement of anions are greater for the anodic and cathodic prepeaks than the main peaks [36].

The anodic prepeak is only seen in some growth media [36]: Perchloric acid, nitric acid, sulphuric acid, 0.5 M Na_2CO_3 and, depending on the growth conditions, phosphoric acid. Fonseca *et al.* [108] found that the prepeak is better defined in sulphuric acid than in perchloric acid. The prepeak disappears when transferring a film grown in an acidic solution to an alkaline one [36, 138]. It is, however, some times possible to see traces of the prepeak during the first one or two cycles in the alkaline solution. This is linked to the slow exchange of protons and anions with alkali metal ions and hydroxide with potential cycling.

From the prepeak's position and peak current at differing sweep rates one finds that the process responsible for the peak is an irreversible surface process. The following reactions are proposed for the prepeak:

$$\mathrm{Ir(OH)_{ads} + H_2O \rightarrow Ir(OH)_2 + e^- + H^+ \rightarrow IrOOH + e^- + H^+} \tag{4.3}$$

The temperature affects the prepeak differently than the main anodic peak. The peak potential of the prepeak decreases with increasing temperature. At the same time the prepeak gets less well defined [136].

4.5 Electronic structure

The energy levels and the nature of the electronic states on a bare and oxide covered Ir electrode were studied by Gottesfeld [140] by using the $Fe(CN)_6^{-3}/Fe(CN)_6^{-4}$ couple. On the bare Ir RDE in acidic solutions the response was as expected for a metal electrode; an anodic and a cathodic limiting current proportional to the concentration and the square of the rotation rate ($\omega^{1/2}$) up to $\omega = 10000$ rpm was observed. On the oxide coated electrode the electrode was blocked for both the anodic and the cathodic processes for potentials below 0.5 V versus SCE. At potentials above 0.9 V versus SCE the oxide covered electrode behaved practically equal to the bare Ir electrode. The gradual transition between the blocking behaviour and the non-blocking behaviour occurred in the same potential region that the film changed from transparent to coloured. The response in alkaline electrolytes, where the $Fe(CN)_6^{-3}/Fe(CN)_6^{-4}$ couple has a higher oxidising power, was different. Here no blocking was observed and the response was the same on the bare and oxide covered RDE. The rate of electron transfer and transport must thus be strongly dependent on the relative positions of the electron energy levels in the solution and in the oxide. The bleaching process is expected to be accompanied by the filling of the *d*-band. This will change the properties of the electrode from that of a metallic conductor to a semiconductor which has a band gap so large that visible light is not absorbed. The blocking effect can thus be explained: In the bleached oxide film the density of states (DOS) is small and the mobility of the charge carriers is low in the region where charge injection has to take place. The reduction of $Fe(CN)_6^{-3}$ will thus be hindered and the reaction rate will be low. At anodic potentials, i.e. in the coloured state, the density of states is high and the film behaves as a metal.

An UPS study of AIROF in perchloric acid by Kötz and Neff [112] gave information about the band structure. Comparing the spectrum of a coloured electrode (1.25 V versus SCE) and a bleached electrode (0.0 V versus SCE) shows that the position of the t_{2g} band in the bleached state is shifted to a value between 1.0 eV and 2.5 eV lower than that of the coloured film. In addition the DOS at the Fermi level is reduced to zero for the bleached film, i.e. the film has semiconducting properties.

The electronic structure of AIROF formed in neutral phosphate buffer solutions (pH = 6.9) was investigated by Silva *et al.* [141]. The reduced film was found to behave as a *p*-type semiconductor. A flat band potential of 0.05 V versus SCE was found using capacitance measurements (Mott-Schottky plots). A band gap of about 3.2 eV was measured from the photoelectrochemical spectrum. This is slightly less than the value, 3.5 eV, for a single crystal of IrO_2.

The electronic structure of AIROF was used by Yuen, Lauks and Dautremont-Smith [128] to explain the shape of the voltammograms recorded on AIROF. A relationship between the DOS and the CV can be shown. This was used to show that AIROF has a pH dependent DOS.

Chapter 5

Oxide powder catalysts

The most convenient way of using an oxide catalyst in a PEM water electrolyser is in the form of a powder catalyst, see Chapter 3.6. The other oxide forms that can be used, are discussed in Chapter 6. Lervik *et al.* [44] gives a comparison of the electrochemical properties of iridium oxide powder and AIROF.

5.1 Manufacturing methods

Several methods have been used to make oxide powder catalysts. Wet chemical methods, like the polyol method [142–145], hydrolysis [44, 146] or sol-gel [16, 147–149], are based on reactions of metal ions in a solution to form metal, hydroxide or oxide particles. Heat treatment can be used to convert metal or hydroxide particles to oxides. Salt melts can also be used, like in the Adams fusion method [150, 151].

In the polyol method a polyol, for example ethylene glycol, is used both as the solvent and the reduction agent. Small metal particles are formed by reduction of the metal ions in solution [142, 152, 153]. Microwave irradiation can be used to shorten the reaction time and increase the nucleation rate giving smaller particles [154]. Subsequent heat treatment converts the metal particles to oxides [143–145]. Both pure and mixed oxides can be produced.

The hydrolysis method is based on forming a metal hydroxide by reacting the metal precursor salt with an aqueous sodium hydroxide solution [44, 146]. The produced powder is heat treated to form an oxide. Pure and mixed oxides can be produced. Lervik *et al.* [44] produced pure iridium oxide powders with an average crystallite size of 20 nm using the hydrolysis method.

The sol-gel methods can be used to make powders or to make layers directly on a substrate. A SnO_2–IrO_2–Ta_2O_5 powder catalyst was prepared by Ardizzone and co-workers [149] using the sol-gel technique, whilst Murakami *et al.* [155] produced a IrO_2–SeO_2 catalyst powder.

The Adams fusion method uses molten $NaNO_3$ as the oxidation agent [150, 151]. Although originally developed for the synthesis of PtO_2 [150, 151], it has later been used for the production of pure and mixed IrO_2 catalysts for use in PEM water electrolysers [156–158]. The mixed oxides include IrO_2–Ta_2O_5 [157], IrO_2–RuO_2 [157] and IrO_2–RuO_2–SnO_2 [156].

Depositing a catalyst on a catalyst support with a high surface area can be an effective way to improve the utilisation and the stability of the catalyst. For oxygen evolution catalyst the support must be able to withstand the high potential encountered during the oxygen evolution reaction. The carbon materials typically used for PEM fuel cells are not stable at the potentials encountered during the oxygen evolution reaction and can not be used. Several materials have been suggested as catalyst support materials for the oxygen evolution reaction, including antimony doped tin oxide [159,160], boron-doped diamond [161,162], Magneli phase titanium oxide [163], titanium carbide [164] and ruthenium-titanium oxide [165,166].

5.2 Mixed oxides

Mixed oxides can refer to both chemical and physical mixtures. Physical mixtures differ from chemical mixtures by the mixing level. Chemical mixtures are mixed on an atomic lever, whilst physical mixtures are mixtures of micro or nano sized particles of the pure components [94]. Interactions between the different oxides can only be seen in chemically mixed oxides. Mixed oxides will, in this text, be used to refer to chemically mixed oxides unless explicitly stated otherwise.

Mixed oxides can be formed when the crystal structures and the electronic band structures of the oxides are compatible. The creation of a common structure is a requirement for the creation of common electronic bands. The creation, or not, of common electronic bands, specifically the valence band, are of interest to electrocatalysis since it will affect the overpotential of reactions on the oxide. A good introduction to the formation of bands in oxides can be found in Goodenough [167]. An overview of the band structure of common oxides, including the ones discussed here, can be found in the work of Honig [168].

If a common valence band is formed, the position of the band should change with composition. This is an effect of different band fillings. A change in band position implies a change in the Fermi level. This implies a change in the oxidation potential, and thus should also affect the oxygen evolution reaction [90]. There should also be a change in the cyclic voltammograms. Unfortunately, it is often hard to detect changes in the cyclic voltammograms because of poor peak resolution.

In the case of iridium and ruthenium oxide alloys prepared by reactive sputtering Kötz and Stucki [169] have shown this relationship. Their results show a shift in the oxygen evolution potential as well as a shift in peak positions in cyclic voltammograms. XPS results show the formation of a common valence band and how it shifts with changes in the composition.

5.2.1 Segregation in mixed oxides

When studying the difference between chemical mixtures and physical mixtures of oxides, one must consider the effect that segregation of the chemical mixture can have on the results. If the chemical mixture segregates into two phases, either pure or nearly pure, the results would be expected to resemble the physical mixture of

the two pure oxides. It is therefore important to check if the chemical mixture is a homogeneous mix or several phases of different composition.

The possibility of forming solid solutions of RuO_2 and IrO_2 was reported in 1980 by Balko and Davidson [170]. Later studies confirm the results [171]. EXAFS (Extended X-ray Adsorption Fine Structure) investigations have been performed [172, 173] using DSA-type electrodes [173] and oxide powder electrodes synthesized by the hydrolysis method [172]. In both cases the conclusion was that a true solid solution was formed between IrO_2 and RuO_2.

Recent preliminary theoretical calculations indicate that iridium and ruthenium can form thermodynamically stable mixed oxides [174, 175]. It is important to keep in mind that the stability of mixed oxides might be different for nanoparticles as compared to larger particles. Mowbray *et al.* [176] calculated the formation energy for nanoparticles and surfaces of several pure oxides. It was found that the formation energy of IrO_2 was significantly higher than those of SnO_2 and RuO_2, whilst TiO_2 had an even lower formation energy. In vacuum a chemical mix with iridium oxide can therefore be expected to be enriched with iridium in the middle of the mixed oxide particle. The surface would be expected to be enriched with the compound with lower formation energy. When the surface of the oxide is covered with oxygen, for example at potentials close to the oxygen evolution potential, the situation changes [175]. As iridium binds oxygen stronger than ruthenium, iridium atoms show a strong tendency to migrate to the surface, particularly to the coordinatively unsaturated sites (cus). Ruthenium will, on the other hand, migrate to the bulk.

A true solid solution was reported by Marshall and co-workers [145] for iridium-tin oxide prepared by the polyol method based on evidence from XRD experiments. The introduction of ruthenium into the iridium-tin system led to a segregation for systems with Ru content over 30 mol%. A mix of metalic Ru and an oxide phase containing Ir, Sn and Ru was formed. A core-shell structure with Ru metall as the core was suggested. Similar results were found in ruthenium rich RuO_2–IrO_2–TiO_2 powders prepared by the sol-gel method, however in a thermally prepared DSA-type electrode no segregation was observed [148]. This was suggested to be an effect of the titanium support do to the oxide particles beeing afixed to the titianium surface. On the other hand in thermally prepard RuO_2–IrO_2 layers on titanium a surface enrichment of iridium was observed [177, 178].

Conflicting conclusions regarding segregations of mixed systems can be found in the literature. In the iridium tin oxide system, prepared by sol-gel, increasing annealing temperatures have been shown to give a surface enrichment of iridium by Ardizzone *et al.* [16]. IrO_2–SnO_2 powders prepared by the sol-gel technique showed a linear shift in the lattice parameters from that of IrO_2 to that of SnO_2 with increasing tin content, segregation was not observed [155]. However, sol-gel synthesis of IrO_2–Ta_2O_5 gave a segregated oxide consisting of a crystalline IrO_2 phase and an amorphous Ta_2O_5-phase for heat treatment temperatures below 700 °C [147]. In the case of the SnO_2–IrO_2–Ta_2O_5 powder catalyst prepared by Ardizzone and coworkers [149] using the sol-gel technique it was not possible to determine if a true solid solution was formed, however a decrease in the crystallite size was observed with increasing amounts of iridium. This was explained to be caused by iridium or tantalum atoms replacing tin in the oxide lattice. This hinders lattice growth

because of the distortion caused by the introduction of a substitutional species in the tin oxide lattice. Furthermore at low iridium contents tantalum has the effect of increasing the surface concentration of iridium, possibly since tantalum displaces iridium in the lattice and moves it to the surface.

5.3 Characterisation studies of pure and mixed oxide powders

To gain full understanding of the oxygen evolution catalysts it is not sufficient to only characterise them under operational conditions, for example in a lab scale PEM electrolyser. In such a system it can be difficult to separate the contributions from the oxide catalyst alone. Therefore the traditional electrochemical methods are employed as well as physical characterisation methods such as X-ray techniques and electron microscopy. A nice review of the properties of several of the oxides used as OER catalysts has been prepared by Matsumoto and Sato [65]. The structure of metallic oxides are discussed by [167].

The structure of the catalyst, including the lattice parameters, is typically determined by XRD. The commonly used oxides for OER catalysts have a rutile structure. Ruthenium and iridium oxide have the rutile structure, as do oxide mixes of iridium or ruthenium with cobalt [179], iron [179], manganese [65], nickel [179], tantalum [146], tin [143, 145, 180] or titanium. The crystallinity of the oxides is affected by the heat treatment temperature, the preparation method and the sample composition. Higher heat treatment temperatures give a more crystalline sample, as demonstrated by Marshall and co-workers [180] for $Ir_{0.6}Sn_{0.4}O_2$. For the iridium-tin oxide system increasing crystallinity was also found with increasing tin content [143].

The preparation of oxide catalysts often involve a heat treatment step. Temperature programmed analysis methods (TPA), like thermal gravimetric analysis (TGA) or tapered element oscillationg microbalance (TEOM), can be used to follow the mass change of the catalyst as it is heated in a chosen atmosphere. Iridium and ruthenium chloride decompose to the respective oxide when heated in air [181]. For $IrO_3 \cdot 3\,H_2O$ the crystal water was lost between 100–200 °C. The oxidation to IrO_2 was completed by about 680 °C, further heating gave a slow mass loss until the oxide decomposed to pure iridium metal at temperatures above 1070 °C. In contrast to this, $RuCl_3 \cdot xH_2O$ showed a continuous weight loss from just above room temperature to 440 °C, where the sample was oxidised to RuO_2. Heat treatment of ruthenium hydroxide at a lower temperature than 400 °C can also give RuO_2. Two hours at 250 °C was enough to fully oxidise electrochemically deposited ruthenium hydroxide [182, 183].

For mixed oxides the composition of the prepared catalyst is seldom exactly the same as the desired composition. Energy dispersive spectroscopy, EDS, is often combined with a SEM or a TEM, and can offer a convenient way of measuring the composition of the sample as a whole or the composition of smaller parts of the sample. XPS can also be used to study the surface composition, or by varying the energy of the X-ray a depth profile of the composition can be obtained [184].

Other methods are also available to study both surface and bulk composition, see for example Rubel *et al.*. [185] for an extensive study on iridium-tin oxide. For iridium-tin oxide samples prepared by the modified polyol method a slight enrichment of tin was found in the surface by XPS measurements [143]. On the other hand iridium enrichment was found for thermally prepared iridium-tin oxide samples [185].

The optimum particle size is a compromise between the increased surface area small particles give and the decrease in stability when the particle size decreases. The particle size is typically calculated from XRD spectra of the catalyst or measured directly from electron microscope pictures. In the later case it can be difficult to separate the crystallite size (as measured by XRD) and the agglomerate size. The agglomerate size can also be found by particle sizing instruments, although the catalyst must often be dispersed in a liquid for such experiments. For nanocrystalline ruthenium oxide prepared by sol-gel methods a decrease in the activity for the oxygen evolution reaction was seen with an increase in the crystallite size [186]. The Tafel slope also increased with increasing particle size, indicating a shift from kinetic to mass transport control. The crystal size can change with the composition of the oxide. Marshall and co-workers found that the crystal size increased with increasing tin content for iridium-tin oxide catalysts prepared by the polyol method [143].

The surface area of the catalyst can be found by gas adsorption. However, this method, called the Brunauer, Emmett and Teller method, does not necessarily give a value relevant for electrochemistry as the surface area found by gas adsorption might not be correlated to the electrochemical surface area. The electrochemical surface area can be found from cyclic voltammetry, see Section 2.2.1. The electrochemical surface area can be used to compare electrodes with different surface area and structure. The OER on AIROF has been compared to both thermally prepared iridium oxide [187] and iridium oxide prepared by the hydrolysis method [44]. In both cases the mechanism and specific electrocatalytic activity for the OER were comparable.

The conductivity of the catalyst can be measured in the dry state by measuring the resistivity over a compressed sample of the catalyst [143]. However, the value measured in the dry state might not be the same as during operation. For example, it is well known that some forms of iridium oxide change conductivity with the potential (i.e the oxidation state), see Chapter 4. Impedance measurements can offer a method of measuring the conductivity of the catalyst at the working potential. Sunde *et al.* [1, 188] proposed an impedance model and a way of interpreting it to find conductivity changes, albeit only qualitatively, of oxide powder electrodes. For iridium oxide prepared by the hydrolysis method and heat treated at temperatures of 450 °C there appeared to be an increase in the conductivity with increasing potential [188]. For samples heat treated at higher temperatures no conclusions could be drawn.

The Tafel slope gives an indication of the mechanism for the OER, as discussed in Section 3.1. There can be several Tafel slopes, one at low overpotentials and one or more at higher potentials. Values in the range 36–42 mV/dec have been observed for iridium-tin oxide powders, indicating that the rate determining step for the OER is the second step in the oxide path, equation (3.5), or the second step in the electrochemical oxide path, equation (3.8) [144]. For iridium-ruthenium oxides

the activity increased and the Tafel slope decreased, from 60–70 mV/dec for pure iridium oxide to 40–50 mV/dec for pure ruthenium oxide, with increasing ruthenium content [160]. Also the Tafel slope was found to decrease with increasing loading of $Ir_{0.5}Ru_{0.5}O_2$. For tin-iridium-tantalum oxide prepared by sol-gel a Tafel slope of 44 mV/dec, slightly lower than the tin-iridium catalyst that was also tested, was found by Ardizzone and co-workers [149]. Comparisons of the OER rate for several oxide compositions and types can be found in Ref. [146, 160]. The Tafel slope and the exchange current density together describe the OER activity of the catalysts.

A different way of stating the activity of the catalyst is to give the potential of the electrode at a given current density. Marshall [180] found the potential at 1 mA/cm^2 for $Ir_{0.6}Sn_{0.4}O_2$ heat treated at temperatures between 400 and 650 °C. The potential was found to vary between 1.48 V for the sample heat treated at 450 °C and 1.52 V for the sample heat treated at 650 °C. To take into account different effective electrode areas the potential at a specific current per charge (A/C) can be used instead of the current density [82, 180].

Chapter 6

Other types of iridium oxide catalysts and metallic iridium

This chapter will briefly discuss some of the other oxide forms that may be used as oxygen evolution catalysts. Experiments performed on metallic iridium that are relevant to the study will also be reviewed.

6.1 Thermally produced oxides

An important class of of oxides used as oxygen evolution catalysts (and a slew of other processes, for example chlorine evolution) is the thermally decomposed oxides. They are often referred to as DSA (Dimensionally Stable Anodes) type electrodes. The DSA was patented by Beer in 1969 [189] and further developed and commercialised by de Nora [190]. Briefly, a DSA consists of a metallic backing, typically titanium, with an active layer of a noble metal oxide or a mixed noble metal oxide layer.

Much of the work on noble metal oxides has been conducted on DSA type electrodes, as such a large amount of literature is available on the thermal oxides. It is however not quite clear how applicable the DSA literature is to this work as there are quite large differences between the oxide powders and the thermally decomposed oxide layers.

DSA electrodes are prepared by applying a layer of a solution containing the precursor salt(s), often chloride salts, to a substrate. Titanium is the common substrate. The thickness of the final oxide layer can be increased by repeated application and drying of the precursor salt solution before the final heat treatment. Heat treatment, typically at 400–600 °C, decomposes and oxidises the salt giving an oxide layer. The use of a titanium substrate gives appreciable titanium oxide amounts in the oxide layer. Using chloride salts gives significant chloride levels in the finished oxide. Nitrate salts can be used if chlorides are unwanted [191].

Several different compositions of thermally produced oxides have been prepared over the years. Traditionally the industrial electrodes consisted of a mix of RuO_2 and TiO_2 [190], possibly with the addition of a third element, for example iridium [192]. Other compositions have also been prepared depending on the application. For

oxygen evolution in neutral or acidic media iridium oxide based electrodes have been used, sometimes stabilised by the addition of other components such as tantalum oxide [193,194], niobium oxide [195], tin oxide [196] or antimony oxide [197] or mixed with ruthenium oxide for increased activity [177,178].

One direct comparison of thermally produced iridium oxide and AIROF was reported by Ouattara *et al.* [187]. The activity and the mechanism for the OER were found to be similar. The shape of the CVs do, however, differ markedly between the thermal oxides and AIROF. The surface redox reaction is faster on AIROF electrodes, but the stability to anodic polarisation is poorer on AIROF.

One of the few studies on the temperature effect on iridium oxide catalysts was reported by Fierro and co-workers [15]. They used an IrO_2 DSA-type electrode supported on p-Si. It was found, by calculating the activation energy for the reactions, that there are two reactions during charging and discharging of the electrode when a CV is recorded. One is a reaction with an activation energy of about 2.4 kJ/mol (dominating at low sweep rates) and the other is a reaction with zero activation energy (seen at high sweep rates). The reaction with zero activation energy is suggested to be caused by the charging of the electrical double layer, whilst the other contribution is related to the slow diffusion of protons within the iridium oxide layer.

On thermally prepared iridium oxide Calderon *et al.* [39] used the Fe^{3+} / Fe^{2+} couple to look at the effect of loading on the fraction of the electrode used. The rather depressing result was that only a small area, less than 2 %, of the electrode area participates in the reaction.

6.2 Physical and chemical vapour deposition

Pure iridium oxide and mixed oxides can be produced by chemical (CVD) or physical vapour deposition (PVD), either directly or by depositing a metal and then oxidising it.

Chao and co-workers [198] showed that it is possible to produce several different morphologies of nanostructured iridium oxide by metal organic chemical vapour deposition. By varying the substrate temperature and the precursor reservoir temperature the following morphologies were produced: Nanoblade, layered-column, incomplete-nanotube and square-nanorod. XRD results show that crystalline iridium oxide was produced. Unfortunately no electrochemical experiments were performed.

Catalytic layers in a PEM water electrolysis cell can be prepared by depositing the oxide catalyst directly onto the electrodes by dc magnetron sputtering (plasma enhanced PVD). Slavecheva and co-workers [199,200] have produced both pure iridium oxide films and iridium platinum oxide films using this technique. Amorphous IrO_2, that covered the substrate in a uniform, porous and continuous film, was formed. Activating the electrode by potential cycling (0–1.4 V) increased the charge of the electrode by oxidising metallic iridium, hydrating the film and increasing the number of active sites in the film. The optimum electrode was found to be a pure IrO_2 layer 500 nm thick, corresponding to a loading of 0.2 mg/cm^2 [200]. This electrode gave a current of 0.3 A/cm^2 at 1.55 V in a PEM cell. The CVs before and

after a 168 hour stability test (galvanostatically at 0.3 A/cm^2) were identical.

Iridium oxide films were sputtered onto substrates using radio frequency and dc plasma excitation by Wessling and co-workers [201–203]. The change in the physical structure and the chemical composition were described for different sputtering parameters. It was found that the morphology of the deposited film changed with potential cycling, giving a less ordered and more open structure after cycling [201,202]. In addition the charge of the electrode and oxygen level increased with cycling, indicative of formation of $Ir(OH)_3$ and $Ir(OH)_4$. The charge of the activated film was found to be proportional with film thickness.

One possibility for making iridium oxide films is to deposit an iridium metal layer on a substrate and subsequently oxidise it electrochemically. This method was used by Lee *et al.* [126] to produce iridium oxide electrodes for neural stimulation. An iridium layer, either 30 nm or 60 nm was deposited on a silicon wafer or titanium by electron beam evaporation. The iridium layer was oxidised electrochemically by cycling the potential between 0 and 1.45 V in 0.1 M sulphuric acid, just as if preparing an AIROF electrode. CVs of the iridium oxide layer are nearly identical[1] to those seen on AIROF. More interestingly, however, was that the 30 nm thick film was fully oxidised (i.e. the layer was oxidised right through to the substrate) after 800 cycles, whilst the 60 nm thick sample required 1600 cycles. A SEM investigation showed that the thickness of the oxide layer increased with cycling and that the final oxide layer was thicker than the original metallic layer. This caused cracking in the electrode that had 60 nm iridium metal deposited on it. The adhesion to the substrate was still good.

XAS of sputtered films show that the oxidation state in sputtered iridium oxide films is close to +4 before the start of the OER [204], compared to +4.8 for AIROF samples [135]. However the decrease in the Ir–O bond length was found to be close to the one found in AIROF, with a decrease from 0.2011 nm to 0.1963 nm when the oxidation state increased from 3.03 to 3.85 for the sputtered film.

The DOS of sputtered iridium oxide films and sputtered iridium tantalum oxide films was found using both electrochemical impedance spectroscopy and potentiometric intermittent titration by Backholm, Georén and Niklasson [205]. Both methods gave roughly the same results. The DOS showed similar trends as theoretical calculations.

6.3 Electrochemically deposited iridium oxide

Iridium oxide electrodes can be produced electrochemically by either first depositing iridium metal and then oxidising it [31, 206, 207], or by depositing iridium oxide directly [32, 208–210].

Jung, Lee and Tak [32] deposited iridium oxide directly onto indium-doped tin oxide (ITO) quarts crystals by electrochemical deposition. The aim was to investigate the electrochromic mechanism via potential step, CV, EQCM, SEM, XPS and Augerelectron spectroscopy (AES). The electrochemical measurements were conducted in a phosphate buffered saline electrolyte at pH 7.2. It was found that the

[1] Disregarding the somewhat original way of presenting the CVs.

colouring of the film is do to proton injection and ejection. Sodium ions might also effect the colouration, insomuch as a higher presence was found in the coloured film than in the bleached. EQCM results confirm the injection and ejection of protons and sodium ions. Interestingly it was found that the iridium oxide film swells and cracks at potentials of 0.9 V (SCE), also the coloured film was thicker than the bleached film. Finally it was found, as seen previously, that the bleached film is $Ir(OH)_3$ and the coloured film is IrO_2.

Iridium oxide was deposited directly onto gold or ITO electrodes from a solution of iridium chloride, oxalic acid and potassium carbonate by Chen, Taylor and Scherson [208]. Absorbance measurements over the visible light spectrum showed increasing absorbance with increasing potential, showing that the electrode was electrochromic. The kinetics of the reduction and oxidation was found to change with the solution pH; in acid (0.5 M H_2SO_4) the oxidation was faster than the reduction, whilst the opposite was true in the alkaline solution (0.3 M Na_2CO_3). The main anodic peak potential was found to change by -77 mV/pH.

Gold was also used as a substrate by Mailley and co-workers [209] to electrodeposit iridium. The deposited iridium was oxidised subsequently. The iridium oxide film they obtained was, however, not quite like AIROF in the electrochemical response. To achieve highly ordered iridium oxide deposits templates of polystyrene spheres can be used [210].

El Saway and Birss [31] deposited iridium metal directly onto a gold coated quartz crystal from a dilute H_2IrCl_6 solution. A porous layer, that could be oxidised electrochemically to a porous electrochromic iridium oxide layer, was formed. A detailed investigation of the optimum deposition conditions are given. A concentration of $H_2IrCl_6 \leq 0.05$ M at a potential of 0.2 V gives a charge efficiency close to 100 %.

6.4 Oxide powder films

A class of electrodes that can be difficult to define are electrodes dip-coated in a solution containing iridium metal powders or iridium metal powder intermediates. Thin iridium metal powder films can be formed this way. The metal powder film can be oxidised thermally or electrochemically by cycling the electrode potential analogous to the production of AIROF [211, 212]. The electrochemically produced oxide layer is electrochromic, thus the electrochemically oxidised electrode has similarities to both a powder electrode and an AIROF electrode. The mechanism and rate for the OER are similar to those found for thermally prepared oxides and AIROF [213].

Analogous films can be made by direct deposition of iridium oxide powders instead of iridium metal powders. Nakagawa, Beasley and Murray [9] deposited iridium oxide powders with a diameter of 2 nm on glass carbon electrodes by electroflocculation. An overpotential for the OER of 0.25 V at 0.5 mA/cm^2 is reported.

6.5 Metallic iridium

A few authors report about investigations on metallic iridium. Undoubtedly several of these investigations are actually studies of thin iridium oxide films on iridium metal, however they are still discussed in this section.

Juodkazytė *et al.* [33] performed an EQCM study of anodic oxidation of thermally produced iridium in acidic and alkaline solutions. Fluctuations in the mass was observed between 0.4–0.8 V and an increase in mass was observed at potentials between 0.8 and 1.2 V. Reaction 6.1 was proposed for the first potential region and reaction 6.2 for the second (both in acidic and alkaline solutions). Judging by the CVs presented it seems likely that the iridium electrode was at least partially oxidised.

$$\mathrm{Ir} + 3\mathrm{H_2O} - 3\mathrm{e^-} \leftrightarrow \mathrm{Ir(OH)_3} + 3\mathrm{H^+} \tag{6.1}$$

$$\mathrm{Ir} + 3\mathrm{H_2O} - 4\mathrm{e^-} \leftrightarrow \mathrm{IrO(OH)_2} + 4\mathrm{H^+} \tag{6.2}$$

Iridium metal can be deposited electrochemically directly onto a titanium substrate [130] from a $(NH_4)_2IrCl_6$ in HCl solution at 40 mA/cm^2. No oxide growth was observed with potential pulsing [130], however the time used was short. The activity of the iridium electrode for the OER decreases with heat treatment, but the stability increases. This behaviour is explained by the electrodeposited iridium layer becoming dehydrated and more compact with heat treatment. Titanium carbide has also been used as a support for an iridium metal OER catalyst [164]. The activity of the supported iridium was significantly higher than the unsupported iridium black.

A screening has been performed of metallic catalyst supported on carbon for OER in acidic media by Forgie and co-workers [174]. Binary mixes of ruthenium with palladium, iridium, copper, cobalt, rhenium, chrome and nickel were prepared over the whole composition range and their activity for the OER was studied. The best catalyst was $Ru_{60}Co_{40}$ and $Ru_{70}Ir_{30}$. As the catalysts were pretreated by potential cycling thin oxide layers were likely formed on the catalysts.

Part II

Papers

Chapter 7

An impedance model for a porous intercalation electrode with mixed conductivity

Svein Sunde, Ingrid Anne Lervik, Lars-Erik Owe, Mikhail Tsypkin

This article is published in The Journal of the Electrochemical Society [1]. *The layout of the article has been changed to improve readability, however the text and figures have not been changed.*

7.1 Abstract

A mathematical model for the impedance of porous intercalation electrodes of mixed conductivity has been derived. The model is based on an agglomerate model and dilute-solution theory. With respect to the impedance of similar electrodes of metallic conductivity, two corrections were identified. The first is related to the diffusional component of interparticle transport in the porous electrode. The second is an impedance related to the exchange of electrons with the electrode at the electrode–support interface. These two corrections may lead to significant deviations in the low frequency region of the impedance spectra of the mixed conductor. In the high frequency region, however, no significant differences were found between the impedance of the metallic electrode and that of mixed conductivity for similar parameter sets. Recombination of charge carriers in the system has been included through a spherical Gerischer impedance, giving rise to substantial deviations in the low frequency regions if reaction rates are significant.

Manuscript submitted January 7, 2009; revised manuscript received April 15, 2009.

7.2 Introduction

Modelling of porous electrodes, and their impedance in particular, plays an important role in the interpretation of experimental data. The models initially proposed for simple processes such as double-layer charging [214, 215] and faradaic reaction [216, 217] has later been extended to include transport processes in the electrolyte phase and also in the electrode. For technologically important electrodes such as those of metal hydride and Li-ion batteries the diffusion process is frequently assumed to take place in spherically shaped electrode particles [218–224]. Another area of current interest is porous, nanostructured, semiconducting electrodes for applications in photovoltaic cells [225].

A common assumption in these models is that the conductivity associated with one of the species in the electrode matrix is high so that the transport of this species can be handled as a pure migration process decoupled from any concentration gradients. It is the purpose below to theoretically investigate the consequences of removing this assumption for the impedance for a porous electrode with spherically shaped intercalation particles with mixed conductivity. That is, we seek to establish a model that can accommodate significant contributions to the matrix conductivity from both positively and negatively charged carriers, such as holes and electrons in a porous semiconducting electrode, or ions and electrons in an intercalation electrode of ionic conductivity comparable to that of the electronic carriers. We discuss the model in terms of parameters typically found in the literature and also expected to be at least partly relevant for a specific system, viz. that of iridium oxide, an electrochromic expected to display significant changes in its electronic and ionic conductivity as a function of its redox state. In particular we address the question of whether or not it is to be expected that the metal-to-insulator transition will be detectable in the impedance spectra of nanostructured, porous iridium oxide electrodes. We do emphasise, however, that the model is far more general to be limited to this system, cf. the examples referred to above.

Below we first outline the physical aspects of the system along with some assumptions made, then briefly review the general modelling framework on which the mathematical model is based, and proceed to work out the detailed theory based on these descriptions. The general behaviour of the impedance derived is discussed in terms of limiting cases and detailed simulations. We limit the discussion to include primarily those aspects of the model that are related to the relations between the mixed-electrode case and the case of a metallic electrode.

7.3 Theory

7.3.1 Physical description

The electrode to be modelled is porous and contains separate particles in electrical and diffusive contact with each other. The electrical current in the electrode particle phase is partly ionic and partly electronic, and the transport from particle to particle occurs through necks as indicated in Fig. 7.1 The necks are narrow in a sense to be

defined below.

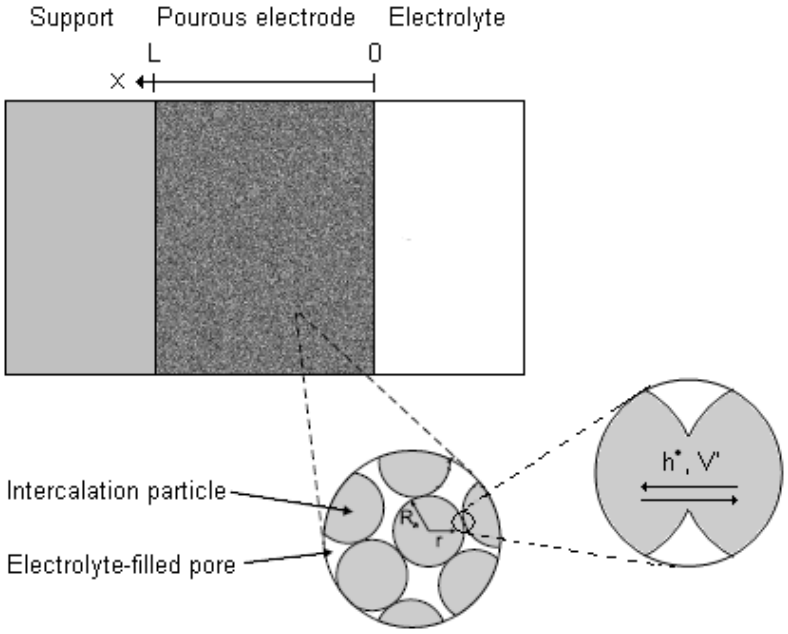

Figure 7.1: Schematic presentation of the porous electrode. The geometry and transport through necks formed between particles are indicated separately. Protons are used as an example of intercalant ions, and holes also contribute to the transport. (Note that in the model derivation we describe the system in terms of proton vacancies and holes (see text).)

The (non-porous) particle may exchange intercalants with the surrounding electrolyte through the area not occupied by necks. The particle is thus presented with two sources of intercalants, the neck boundary with other particles and the interface to the electrolyte containing dissolved intercalants. We assume spherical particles, but the macroscopic shape of the electrode is a sheet of the electrode material with dimensions in the direction normal to the sheet much smaller than the in-plane dimensions. The backing material on which the electrode rests is assumed to be a metal.

Apart form this the model follows concepts similar to the flooded-agglomerate model as described for example in Ref. [218], and porous-electrode modelling will be employed [226]. The transport of charge in the matrix is thus handled as a one-dimensional process. We also assume that diffusional processes in the electrolyte phase are not important. This is relevant when composite electrodes of intercalation particles and solid electrolytes such as Nafion are employed [146]. We neglect the effects of extended space charges in the model, assuming that any deviations from electroneutrality in the particles are confined to a region at the electrolyte-matrix interface of negligible dimensions relative to the particle size. Likewise we assume the absence of any such regions of extension comparable to the typical pore size in the electrolyte phase.

7.3.2 Speciation for a mixed electronic–ionic system: Iridium oxide

The equations to be derived below assume two oppositely charged species in the solid phase. We illustrate here the speciation of an oxide system to illustrate that the theory can also be used to describe other binary systems than intrinsic semiconductors or the like. As an example of current interest we consider iridium oxide.

The electronic structure of crystalline iridium oxide is characterised by a partially filled t_{2g} band [168]. Upon reduction the t_{2g} band fills up with electrons and the extra charge associated with these are assumed being compensated for by the intercalation of protons or hydroxyl ions. Whether hydroxyl ions or protons are the actual species being exchanged is of no concern here [227], and for sake of illustration we choose to consider protons as the intercalated species.

Close to the completely reduced state of the oxide where the t_{2g}-band is almost completely filled, the oxide (in the form of anodically formed iridium oxide films, AIROF) thus behaves as a p-type semiconductor [140, 141]. Consistent with this, it also displays anodic colouration, in contrast (literally speaking) to a number of other oxides [40]. Also, previous impedance data on AIROF show signs of large decreases in conductivity upon reduction (proton injection/hydroxyl ejection) of the oxide [129].

A natural choice of species in iridium oxide may therefore be protons and holes. However, these species would not appear in the oxide in equal quantities, and their charges take the same sign. Assuming the number of vacant states per volume in the t_{2g}-band in the fully oxidised oxide (i.e. corresponding to the stoichiometric IrO_2) to be c_0, the concentration of electron holes becomes $p = c_0 - c_+$, where c_+ is the proton concentration. As an alternative, therefore, one may take the fully reduced state of the oxide as a point of departure. In analogy with the Kröger-Vink notation [228] for defects in solids one may consider proton vacancies of effective negative charge therefore as a species in the system in addition to the electron holes. Thus, we choose here to describe the oxide in terms of these species, ascribing a negative charge to the former and a positive charge to the latter, for which the system becomes perfectly analogous to a binary electrolytic solution.

7.3.3 Mathematical model for the impedance of the intercalation particle

We employ here the dilute-solution approximation in which the flux density vector of species i in the particle, $\mathbf{N}_i$, (in the absence of convection) is described by [229]

$$\mathbf{N}_i = -z_i u_i F c_i \nabla \Phi_1 - D_i \nabla c_i \tag{7.1}$$

where z_i is the charge number, u_i the mobility, c_i the concentration, and D_i the diffusion coefficient of species i. F is the Faraday constant, and Φ_1 the electric potential. We assume in this work the diffusion coefficient to be constant (i.e. no variations with concentration).

The choice of species made in the previous section now makes it possible to use equations for a binary electrolyte, for which the material balance,

$$\frac{\partial c_i}{\partial t} = -\nabla \cdot \mathbf{N_i} + R_i \tag{7.2}$$

becomes [229]

$$\frac{\partial c}{\partial t} = D\nabla^2 c + R_c \tag{7.3}$$

with

$$c = \frac{c_+}{\nu_+} = \frac{c_-}{\nu_-} \tag{7.4}$$

$$R_c = \frac{z_+ u_+ R_- - z_- u_- R_+}{z_+ u_+ - z_- u_-} \tag{7.5}$$

and

$$D = \frac{z_+ u_+ D_- - z_- u_- D_+}{z_+ u_+ - z_- u_-} \tag{7.6}$$

by elimination of the electrical potential. In these equations $\nu_+ = 1$ and $\nu_- = 1$ are the number of moles of holes and proton vacancies introduced in the oxide per mole of electrons extracted during its oxidation. R_i is the production rate of species i. Eq. (7.3) is valid also for non-zero currents [229]. (Eq. (7.4) would imply the relation $R_+/\nu_+ = R_-/\nu_-$, but this is not important here.)

We assume that a harmonic perturbation is applied in the driving force for intercalation (applied potential or current) for $t > 0$ so that the concentration c may be written:

$$c = c\,(\mathbf{r}, 0) + \tilde{c}\,(\mathbf{r}, t) \tag{7.7}$$

The Laplace-transformation of the time-derivative of the concentration is then

$$\mathcal{L}\left\{\frac{\partial c}{\partial t}\right\} = s\mathcal{L}\left\{\tilde{c}\right\} - \tilde{c}\,(0) = s\mathcal{L}\left\{\tilde{c}\right\} \tag{7.8}$$

the last relation owing to $\tilde{c}\,(0) = 0$. Insertion of (7.8) into (7.3) yields

$$s\mathcal{L}\left\{\tilde{c}\right\} = D\nabla^2\mathcal{L}\left\{\tilde{c}\right\} + \mathcal{L}\left\{\tilde{R}_c\right\} \tag{7.9}$$

with

$$\nabla^2\mathcal{L}\left\{\tilde{c}\right\} = \frac{1}{r^2}\left[\frac{\partial}{\partial r}\left(r^2\frac{\partial\mathcal{L}\left\{\tilde{c}\right\}}{\partial r}\right) + \frac{1}{\sin\vartheta}\frac{\partial}{\partial\vartheta}\left(\sin\vartheta\frac{\partial\mathcal{L}\left\{\tilde{c}\right\}}{\partial\vartheta}\right) + \frac{1}{\sin^2\vartheta}\frac{\partial^2\mathcal{L}\left\{\tilde{c}\right\}}{\partial\varphi^2}\right] \tag{7.10}$$

in spherical coordinates. ϑ and φ are the angles of the polar coordinate system. The reaction rate R_c is assumed to consist of one time-independent and one time-dependent term as in Eq. (7.7) for the concentration.

As boundary conditions we require that the solution is finite at r = 0. At the particle interfaces r = R_a holes may only be transported into or out of the particle through the necks, Fig. 7.1, whereas vacancies may also be generated or annihilated at the particle interface exposed to the electrolyte in addition to the

vacancy transport through necks. In general the rate of particle exchange at r = R_a, $\mathcal{L}\{\tilde{v}\}$, therefore depends on variables ϑ and φ, Eq. (7.10). Neglecting the effect of transport through necks on the concentration inside the particles through the assumption of narrow necks, however, we set [229]

$$\frac{\mathcal{L}\left\{\tilde{i}_f\right\}}{z_-\nu_-F} = -\frac{D}{1-t_-}\frac{\partial\mathcal{L}\{\tilde{c}\}}{\partial r}\mid_{r=R_a} = -\mathcal{L}\{\tilde{v}_f\} \tag{7.11}$$

where $\mathcal{L}\left\{\tilde{i}_f\right\}$ is the Laplace transform of the harmonically varying (in analogy with Eq. (7.7)) part of the faradaic current at the particle-electrolyte interface and $\mathcal{L}\{\tilde{v_f}\}$ is implicitly defined as $\mathcal{L}\left\{\tilde{i}_f\right\}/(z_-\nu_-F) = -\mathcal{L}\{\tilde{v_f}\}$, or $\mathcal{L}\left\{\tilde{i}_f\right\}/F = \mathcal{L}\{\tilde{v_f}\}$ with $z_- = -1$ and $\nu_- = 1$. t_- is the transference number for (here) intercalant vacancies, $t_- = -z_-u_-/(z_+u_+ - z_-u_-)$ [229].

We assume the faradaic current (corresponding to interfacial ion transfer for the case of iridium oxide) i_f to be a function of the proton concentration in the oxide particle and the potential difference $\Phi_1 - \Phi_2$, where Φ_2 is the potential in the electrolyte, as

$$\begin{aligned}\tilde{i}_f &= \left(\frac{\partial i_f}{\partial c}\right)_{\Phi_1-\Phi_2}\tilde{c}\,(r=R_a) + \left[\frac{\partial i_f}{\partial(\Phi_1-\Phi_2)}\right]_c\left(\tilde{\Phi}_1-\tilde{\Phi}_2\right)\\ &= A\tilde{c}\,(r=R_a) + B\left(\tilde{\Phi}_1-\tilde{\Phi}_2\right)\end{aligned} \tag{7.12}$$

with $A = \left(\frac{\partial i_f}{\partial c}\right)_{\Phi_1-\Phi_2}$ and $B = \left[\frac{\partial i_f}{\partial(\Phi_1-\Phi_2)}\right]_c$.

Below we will calculate the impedance of a porous electrode containing the intercalation particles employing a one-dimensional model. For this model it is practical to express the gradient of $\tilde{c}$ in terms of the potential and current in the solid phase. To this end we therefore note that [229]

$$-\frac{i_s}{z_+\nu_+F} = (z_+u_+ - z_-u_-)\,Fc\frac{\partial\Phi_1}{\partial x} + (D_+ - D_-)\frac{\partial c}{\partial x} \tag{7.13}$$

as expressed in terms of x since for narrow necks the radial coordinate will be in the x-direction. i_s is the current corresponding to the rate of transfer of species across the neck.

With Eq. (7.7) and the corresponding equation for Φ_1 the term $c\partial\Phi_1/\partial x$ becomes

$$c\frac{\partial\Phi_1}{\partial x} = \left[c\,(R_a, t=0) + \tilde{c}\,(R_a,t)\right]\left[\frac{\partial\Phi_1}{\partial x}\,(t=0) + \frac{\partial\tilde{\Phi}_1}{\partial x}\,(t)\right] \tag{7.14}$$

Neglecting second order terms, the contribution to $\tilde{v}$ therefore consists of a term $c\partial\tilde{\Phi}_1/\partial x$ and a term $\tilde{c}\partial\Phi_1\,(t=0)/\partial x$. We expect $\partial\Phi_2/\partial x\,(t=0) = 0$ since the current at $t = 0$ is zero. Therefore, in view of Eq. (7.12), with zero faradaic current and diffusive equilibrium through the necks, we expect also that $\partial\Phi_1/\partial x\,(t=0) = 0$, and

$$c\frac{\partial\Phi_1}{\partial x} \approx c_e\frac{\partial\tilde{\Phi}_1}{\partial x}\,(t) \tag{7.15}$$

where c_e is the steady-state concentration in the matrix.

For the remainder of this paper we assume that $\nu_- = \nu_+ = 1$ and that $z_+ = -z_- = 1$. However, more general expression should be easily worked out if needed.

7.3.4 The single-particle impedance

In a random packing of particles, each particle typically has six neighbours [230]. In the current model the interparticle transport is considered to occur in the x-direction (normal to the electrode plane). We consider a time instant in which there is transport of defect into the particle through a neck pointing in the negative x-direction. This transport would partly be compensated by transport of defects out of the particle through a neck pointing in the positive x-direction, should such a neck also be present, since the driving forces for particle transport (gradients in the x-direction in Φ_1 and c) hardly would change sign from particle to particle.

Since gradients in Φ_1 and c along x would be much smaller than to lead to significant changes in magnitude across one particle diameter, the direct consequences in terms of net transport into or out of the particle would thus not be expected to be of any consequence except for blocking a fraction of the particle surface to intercalation from the electrolyte. However, the process would offset the symmetry of the diffusion process that would otherwise have been spherical. This also, in turn, leads to a dependence of $\Phi_1 - \Phi_2$ on ϑ and φ, that would lead to a non-uniform faradaic current at the particle surface.

For deriving a reasonably simple approximation for the diffusion process in the intercalant particles, we make the fundamental assumption that the diffusion process is still reasonably well represented by one not dependent on ϑ and φ. If intercalant transport through the necks formed between the intercalation particles is neglected and there is only intercalation from solution, the angle-independent part of Eq. (7.10) combined with Eq. (7.2) may be written (c.f. Ref. [219])

$$s\mathcal{L}\left\{\tilde{u}\right\} = D\frac{\partial^2 \mathcal{L}\left\{\tilde{u}\right\}}{\partial r^2} - k\mathcal{L}\left\{\tilde{u}\right\} \tag{7.16}$$

where $\tilde{u}$ is related to $\tilde{c}$ as $\tilde{u} = r \cdot \tilde{c}$. In Eq. (7.16) we have included also a sink term (with $k > 0$, not included in Ref. [219]) to account for the case of trapping of neutral combination of charge carriers [129]. The rate constant k absorbs rate constants and any other prefactors stemming from linearisation of R_+ and R_- in the concentration c, and includes also the factors associated with z_+, u_+ etc, c.f. Eq. (7.5). (In Ref. [129] equilibrium was assumed for the trapping process.) Eq. (7.16) may also be relevant for the case of intrinsic semiconductors with significant hole and electron recombination.

At r = 0 the boundary condition for $\mathcal{L}\left\{\tilde{u}\right\}$ becomes

$$\mathcal{L}\left\{\tilde{u}\right\} = 0, r = 0 \tag{7.17}$$

With boundary conditions Eq. (7.17) and Eq. (7.11) the solution of Eq. (7.16) becomes

$$\mathcal{L}\left\{\tilde{c}\right\} = \frac{(1-t_-)\,\mathcal{L}\left\{\tilde{v}_f\right\}\sinh\left(\alpha r\right)}{rD\left[\frac{\alpha}{R_a}\cosh\left(\alpha R_a\right) - \left(\frac{1}{R_a^2}\right)\sinh\left(\alpha R_a\right)\right]} = \mathcal{L}\left\{\tilde{v}_f\right\} G\left(s, r; R_a, D\right) \tag{7.18}$$

where $\alpha = \sqrt{\frac{s+k}{D}}$.

Laplace-transforming the equation for the faradaic current at the oxide surface, Eq. (7.12), and inserting Eq. (7.18) into the result gives

$$Y_f = \frac{\mathcal{L}\left\{\tilde{i}_f\right\}}{\mathcal{L}\left\{\tilde{\Phi}_1 - \tilde{\Phi}_2\right\}} = \frac{B}{1 - \frac{A}{F} Z_{D\prime}} \tag{7.19}$$

with [219]

$$Z_{D\prime}(j\omega) = \frac{(1 - t_-)\, R_a}{D} \frac{\tanh\left(R_a \sqrt{\frac{j\omega + k}{D}}\right)}{\left[R_a \sqrt{\frac{j\omega + k}{D}} - \tanh\left(R_a \sqrt{\frac{j\omega + k}{D}}\right)\right]} \tag{7.20}$$

Eq. (7.19) may be graphically represented by an equivalent circuit consisting of a resistor 1/B in series with the diffusion impedance $Z_D = -\frac{A}{BF} Z_{D\prime}(j\omega)$. With k = 0 the diffusion impedance, Eq. 7.20 is identical to the impedance derived for spherical particles by Jacobsen and West [231] (with subscripts δ and 0 in their paper corresponding to r = 0 and $r = R_a$ here).

For $k \neq 0$ Eq. (7.20) corresponds to the spherical equivalent of a Gerischer impedance.

For k = 0, dividing Z_D by $\tanh R_a \sqrt{\frac{j\omega}{D}}$ may be represented by an equivalent circuit consisting of the parallel connection of an impedance element $\sim \frac{\tanh R_a \sqrt{\frac{j\omega}{D}}}{\sqrt{j\omega D}}$ well known for one-dimensional diffusion [232], and a resistance $\sim \frac{R_a}{D}$. However, in this case the value of the resistance and the components of the other impedance in this parallel circuit would be correlated. These should in principle not, therefore, appear as independent variables in complex non-linear least-squares (CNLS) fitting.

7.3.5 Impedance of the porous electrode

For the electrode phase in the porous electrode we have from Eq. (7.13) and (7.15) (with all steady-state gradients equal to zero)

$$\tilde{i}_1 = -\sigma \frac{\partial \tilde{\Phi}_1}{\partial x} - \Delta \frac{\partial \tilde{c}}{\partial x} \tag{7.21}$$

with $\sigma = \xi\left(z_+ u_+ - z_- u_-\right) c_e z_+ \nu_+ F^2$ and $\Delta = \xi z_+ \nu_+ F\left(D_+ - D_-\right)$. ξ is the ratio between the neck area per projected electrode area and the projected electrode area, $\xi i_s = i_1$.

Ohm's law for the electrolyte and the charge balance read [217, 226]

$$\tilde{i}_2 = -\kappa \frac{\partial \tilde{\Phi}_2}{\partial x} \tag{7.22}$$

$$\frac{\partial \tilde{i}_1}{\partial x} + \frac{\partial \tilde{i}_2}{\partial x} = 0 \tag{7.23}$$

In Equations (7.21), (7.22), and (7.23), i_1 and i_2 are the macroscopic current densities in the electrode and electrolyte phases, respectively [226]. κ is the conductivity of the electrolyte phase. The number of charges per time per length that leaves the electrolyte phase is given by

$$\frac{\partial \tilde{i}_2}{\partial x} = a\tilde{i}_f + \frac{\partial a\tilde{q}}{\partial t} \tag{7.24}$$

where a is the surface area per volume. q is the charge in the double layer process.

Again, a harmonic perturbation has been assumed to be applied for $t > 0$ so that all quantities may be split into time-dependent and time-independent parts as in Eq. (7.7).

Using that

$$\frac{\partial aq}{\partial t} = a\frac{\partial q}{\partial \left(\Phi_1 - \Phi_2\right)}\frac{\partial \left(\Phi_1 - \Phi_2\right)}{\partial t} = aC_d\frac{\partial \left(\tilde{\Phi}_1 - \tilde{\Phi}_2\right)}{\partial t} \tag{7.25}$$

Laplace-transforming Eq. (7.24), and using Eq. (7.25),

$$\frac{d\mathcal{L}\left\{\tilde{i}_2\right\}}{dx} = a\mathcal{L}\left\{\tilde{i}_f\right\} + aC_d\mathcal{L}\left\{\frac{\partial \left(\tilde{\Phi}_1 - \tilde{\Phi}_2\right)}{\partial t}\right\} \tag{7.26}$$

Because the harmonic signal is applied for $t > 0$ only and

$$\mathcal{L}\left\{\frac{\partial \left(\tilde{\Phi}_1 - \tilde{\Phi}_2\right)}{\partial t}\right\} = s\mathcal{L}\left\{\tilde{\Phi}_1 - \tilde{\Phi}_2\right\} - \left[\tilde{\Phi}_1\left(0\right) - \tilde{\Phi}_2\left(0\right)\right] = s\mathcal{L}\left\{\tilde{\Phi}_1 - \tilde{\Phi}_2\right\} \tag{7.27}$$

we obtain

$$\frac{d\mathcal{L}\left\{\tilde{i}_2\right\}}{dx} = a\mathcal{L}\left\{\tilde{i}_f\right\} + aC_d s\mathcal{L}\left\{\tilde{\Phi}_1 - \tilde{\Phi}_2\right\} \tag{7.28}$$

We now assume that there exists a relation between the faradaic current $\mathcal{L}\left\{\tilde{i}_f\right\}$ and the potential difference $\mathcal{L}\left\{\tilde{\Phi}_1 - \tilde{\Phi}_2\right\}$ through an admittance $Y_f\left(s\right)$ such as in Eq. (7.19).

Thus

$$\frac{d\mathcal{L}\left\{\tilde{i}_2\right\}}{dx} = \left[aY_f\left(s\right) + aC_d s\right]\mathcal{L}\left\{\tilde{\Phi}_1 - \tilde{\Phi}_2\right\} \tag{7.29}$$

From Equations (7.21) and (7.22) we get

$$\frac{d\tilde{\Phi}_1}{dx} + \frac{\Delta}{\sigma}\frac{\partial \tilde{c}}{\partial x} - \frac{d\tilde{\Phi}_2}{dx} = -\frac{\tilde{i}_1}{\sigma} + \frac{\tilde{i}_2}{\kappa} \tag{7.30}$$

With Eq. (7.18) this becomes

$$\frac{d\mathcal{L}\left\{\tilde{\Phi}_1\right\}}{dx} + \frac{\Delta}{\sigma}G\frac{\partial \mathcal{L}\left\{\tilde{v}_f\right\}}{\partial x} - \frac{d\mathcal{L}\left\{\tilde{\Phi}_2\right\}}{dx} = -\frac{\mathcal{L}\left\{\tilde{i}_1\right\}}{\sigma} + \frac{\mathcal{L}\left\{\tilde{i}_2\right\}}{\kappa} \tag{7.31}$$

Using that $\mathcal{L}\{\tilde{v}_f\} = \mathcal{L}\left\{\tilde{i}_f\right\} F^{-1} = (Y_f/F)\,\mathcal{L}\left\{\tilde{\Phi}_1 - \tilde{\Phi}_2\right\}$ we finally get

$$H(s)\,\frac{d\mathcal{L}\left\{\tilde{\Phi}_1 - \tilde{\Phi}_2\right\}}{dx} = -\frac{\mathcal{L}\left\{\tilde{i}_1\right\}}{\sigma} + \frac{\mathcal{L}\left\{\tilde{i}_2\right\}}{\kappa} \tag{7.32}$$

where

$$H(s) = 1 + \frac{\Delta Y_f G}{\sigma F} \tag{7.33}$$

where G is to be evaluated at $r = R_a$, i. e. at the particle necks. Since $G(r = R_a) = Z_{D\prime} = -\frac{BF}{A} Z_D$ and with Eq. (7.19),

$$H(s) = 1 - \frac{B\Delta}{\sigma A} Y_f Z_D = 1 - \frac{B\Delta}{\sigma A}\frac{Z_D}{\frac{1}{B} + Z_D} \tag{7.34}$$

Suitable boundary conditions are

$$\begin{aligned} \tilde{i}_2 = -\tilde{I}, \tilde{i}_1 = 0 \text{ at } x = 0 \\ \tilde{\Phi}_2 = 0 \text{ at } x = 0 \\ \tilde{i}_2 = 0 \text{ at } x = L \end{aligned} \tag{7.35}$$

Integration of Eq. (7.23) and use of Eq. (7.35) gives

$$\tilde{i}_1 + \tilde{i}_2 = -\tilde{I} \tag{7.36}$$

Inserting Eq. (7.36) into Eq. (7.32) gives

$$\frac{d\tilde{\Phi}_1}{dx} - \frac{d\tilde{\Phi}_2}{dx} = \left[\frac{\tilde{I}}{\sigma} + \tilde{i}_2\left(\frac{1}{\kappa} + \frac{1}{\sigma}\right)\right]\frac{1}{H(s)} \tag{7.37}$$

Differentiating Eq. (7.29) and using Eq. (7.37) gives

$$\frac{d^2\mathcal{L}\left\{\tilde{i}_2\right\}}{dx^2} = \frac{a\left[Y_f(s) + C_d s\right]}{H(s)}\left[\mathcal{L}\left\{\tilde{i}_2\right\}\left(\frac{1}{\sigma} + \frac{1}{\kappa}\right) + \frac{\mathcal{L}\left\{\tilde{I}\right\}}{\sigma}\right] \tag{7.38}$$

The solution to this differential equation with the boundary conditions (7.35) is [217]

$$\frac{\mathcal{L}\left\{\tilde{i}_2\right\}}{\mathcal{L}\left\{\tilde{I}\right\}} = -\frac{\kappa}{\sigma + \kappa}\left[1 + \frac{\sigma/\kappa \sinh\nu(1-y) - \sinh\nu y}{\sinh\nu}\right] \tag{7.39}$$

with

$$\begin{aligned} y &= \frac{x}{L} \\ \nu &= L\sqrt{c\frac{\kappa+\sigma}{\kappa\sigma}} \\ c &= \frac{\left[aY_f(s) + aC_d s\right]}{H(s)} \end{aligned} \tag{7.40}$$

Integration of Eq. (7.22) and using Eq. (7.39) gives

$$\mathcal{L}\left\{\tilde{\Phi}_2(L)\right\} - \Phi_2(0) = \frac{L\mathcal{L}\left\{\tilde{I}\right\}}{\kappa+\sigma}\left[1 + \frac{-\frac{\sigma}{\kappa}(1-\cosh\nu) - \cosh\nu + 1}{\nu\sinh\nu}\right] \tag{7.41}$$

Use of Eq. (7.39) in Eq. (7.29) gives

$$\mathcal{L}\left\{\tilde{\Phi}_1(L)\right\} - \mathcal{L}\left\{\tilde{\Phi}_2(L)\right\} = \frac{L\mathcal{L}\left\{\tilde{I}\right\}}{H(s)\,\nu\sinh\nu}\left(\frac{1}{\kappa} + \frac{1}{\sigma}\cosh\nu\right) \tag{7.42}$$

Adding Eqs. (7.41) and (7.42) gives for the impedance Z_p, defined as $Z_p = \left[\mathcal{L}\left\{\tilde{\Phi}_1(L)\right\} - \Phi_2(0)\right]/\mathcal{L}\left\{\tilde{I}\right\}$ (c.f. Ref. [226])

$$\begin{aligned} Z_p &= \frac{\mathcal{L}\left\{\tilde{\Phi}_1(L)\right\} - \Phi_2(0)}{\mathcal{L}\left\{\tilde{I}\right\}} \\ &= \frac{L}{\kappa+\sigma}\left[1 + \frac{\frac{\kappa+\sigma}{H(s)\kappa} - \frac{\sigma}{\kappa} + 1 + \left(\frac{\kappa+\sigma}{H(s)\sigma} + \frac{\sigma}{\kappa} - 1\right)\cosh\nu}{\nu\sinh\nu}\right] \end{aligned} \tag{7.43}$$

where the Laplace-variable s is related to angular frequency ω through $\mathrm{s} = j\omega$, where $\mathrm{j} = \sqrt{-1}$.

To relate the potential difference $\mathcal{L}\left\{\tilde{\Phi}_1(L)\right\} - \Phi_2(0)$ to the potential as measured with respect to a reference electrode we assume the iridium oxide system and the speciation given above and write the proton-transfer reaction as (for the oxidation direction of the reaction) as

$$H_H^x \rightleftharpoons V_H\prime + H^+(aq) \tag{7.44}$$

where H_H^x is an intercalated hydrogen, and at the interface to the electrode support connecting to the electrode

$$0 \rightleftharpoons h^\bullet + e' \tag{7.45}$$

The electrochemical potential of electrons in the connecting leads is thus given through (in the dilute solution limit [233]),

$$-\mu_e = \mu_h = \mu_h^0 + RT\ln c(L) + F\Phi_1(L) \tag{7.46}$$

assuming Eq. (7.45) to be in equilibrium. Since the measured potential is related to the electrochemical potential in a reference electrode as $-FV = \mu_e - \mu_e^{ref}$ it follows that the potential V is logarithmically dependent on c. We assume that μ_e^{ref} can be measured by a reference electrode so that its value is representative of Φ_2 at $x = 0$ plus a constant. The amplitude and phase of the measured electrode potential is thus derived by taking the time dependent part of the linearised Eq. (7.46),

$$F\tilde{V} = \frac{RT}{c_e}\tilde{c}(L) + F\tilde{\Phi}_1(L) - F\Phi_2(0) \tag{7.47}$$

Using Eq. (7.18) for $\tilde{c}$ and Eq. (7.19) for the rate $\tilde{v} = \tilde{i_f}/F$ at $x = L$ gives

$$F\mathcal{L}\left\{\tilde{V}\right\} = F\mathcal{L}\left\{\tilde{\Phi}_1(L)\right\} - F\Phi_2(0) - \frac{RT}{c_e}\frac{B}{A}Z_D Y_f\left[\mathcal{L}\left\{\tilde{\Phi}_1(L)\right\} - \mathcal{L}\left\{\tilde{\Phi}_2(L)\right\}\right] \tag{7.48}$$

Replacing the potential difference $\left[\tilde{\Phi}_1(L) - \tilde{\Phi}_2(L)\right]$ with the expression in Eq. (7.42) finally gives

$$F\mathcal{L}\left\{\tilde{V}\right\} = F\mathcal{L}\left\{\tilde{\Phi}_1(L)\right\} - F\Phi_2(0) - \frac{RT}{c_e}\frac{B}{A}\frac{Z_D Y_f}{H(s)}\frac{L\mathcal{L}\left\{\tilde{I}\right\}}{\nu\sinh\nu}\left(\frac{1}{\kappa} + \frac{1}{\sigma}\cosh\nu\right) \tag{7.49}$$

The impedance of the porous intercalation electrode is thus given by Equations (7.19), (7.20), (7.40), and (7.43) plus an additive correction term

$$Z_p^m = -\frac{RT}{c_e}\frac{B}{FA}\frac{Z_D Y_f}{H(s)}\frac{L}{\nu\sinh\nu}\left(\frac{1}{\kappa} + \frac{1}{\sigma}\cosh\nu\right) \tag{7.50}$$

7.3.6 Limiting behaviour

It is of interest to investigate the model derived above in various limits of parameters and frequencies for the interpretation of experimental data. For comparing the mixed-conductivity case with the case in which the oxide is effectively a metallic conductor, we first address the case for which $\Delta = 0$. For this case, in turn, we first address first the dependence on the conductivities σ and κ.

For large values of σ and κ ν becomes small, and, by expanding the sinh- and cosh-functions of Z_p (Eq. (7.43)) Z_p reduces to

$$\lim_{\nu\to 0} Z_p = \frac{L}{\kappa+\sigma}\left[1 + \frac{2 + \frac{\sigma}{\kappa} + \frac{\kappa}{\sigma}}{\nu^2}\right] \tag{7.51}$$

For large values of σ and κ the first term approaches zero, and upon insertion of Eq. (7.40) the last term becomes $1/Lc$. Thus

$$\lim_{\kappa,\sigma\to\infty} Z_p = \frac{1}{Lc} = \frac{1}{La\left(Y_f + j\omega C_d\right)} \tag{7.52}$$

In other words, a parallel connection of single particle impedances as expected. In this case it then becomes interesting to investigate the high and low frequency limits of Y_f, for which we refer to Ref. [220], in which it is shown that the diffusion impedance would be expected to behave roughly as a semi-infinite Warburg element at high frequencies ($\omega \gg \omega_D = \frac{D}{R_a^2}$) and as a series combination of a capacitor and a resistor at low ω, $\omega \ll \omega_D$. At high ω a semicircle representing the parallel combination of $1/B$ and C_d would result.

For finite conductivities κ and σ the porous-electrode impedance Z_p (Eq. (7.43)) becomes

$$Z_p \simeq \frac{L}{\kappa+\sigma}\left[1 + \frac{2}{\nu^{\frac{1}{2}}\exp\nu} + \frac{\frac{\sigma}{\kappa} + \frac{\kappa}{\sigma}}{\nu}\right] \simeq \frac{L}{\kappa+\sigma}\left[1 + \frac{\frac{\sigma}{\kappa} + \frac{\kappa}{\sigma}}{\nu}\right] \tag{7.53}$$

in the large ν-limit. With the definition of ν (Eq. (7.40)) included

$$Z_p = \frac{L}{\kappa+\sigma} + \frac{\sigma^2+\kappa^2}{(\kappa\sigma)^{\frac{1}{2}}(\kappa+\sigma)^{\frac{3}{2}}} \frac{1}{\sqrt{a\left(Y_f + j\omega C_d\right)}} \tag{7.54}$$

In the limit of $\omega \gg \omega_D$ the particle admittance Y_f reduces to a conductance B. For this situation, the impedance given by Eq. (7.54) becomes equivalent of a linear Gerischer element.

For small ν the sinh- and cosh- functions may be expanded as in Eq. (7.51), and on using Eq. (7.40) we get

$$\lim_{\nu\to 0} Z_p = \frac{L}{\kappa+\sigma}\left[1 + \frac{2+\frac{\sigma}{\kappa}+\frac{\kappa}{\sigma}}{L^2}\left(\frac{\kappa\sigma}{\kappa+\sigma}\right)\frac{1}{a\left(Y_f+j\omega C_d\right)}\right] \tag{7.55}$$

Eq. (7.55) is thus simply a shifted and scaled single-particle impedance, i. e. a shifted and scaled version of Eq. (7.52). Depending on parameters this may give e.g. a shifted semi-circle in the impedance-plane plot (finite B but negligible Z_D) or a series connection of a capacitor and a resistance (negligible Y_f altogether).

For materials expected to switch conductivity, it is also of interest to investigate Z_p in the limit of low matrix conductivity σ. For $\sigma/\kappa \to 0$ ν (Eq. (7.40)) becomes

$$\lim_{\sigma/\kappa\to 0} \nu = L\sqrt{\frac{aY_f(s) + aC_d(s)}{\sigma}} \tag{7.56}$$

For large ratios of κ/σ the last term in Eq. (7.43) becomes approximately equal to $L(\coth\nu)/(\sigma\nu)$. Expanding the coth-function ($x\coth x \approx 1+\frac{1}{3}x^2$) for low values of ν (and frequency) gives

$$Z_p \approx L\left(\frac{1}{\kappa} + \frac{1}{\sigma\nu^2} + \frac{1}{3\sigma}\right) \tag{7.57}$$

In the high-frequency regime $\nu^{-1}\coth\nu \approx \nu^{-1}$, which again may give rise to the approximation that the impedance acts as a Gerishcer element.

This essentially brings back the limiting form described by Eq. (7.55) above but with different parameters.

The equations above are analytical expressions of the forms presented graphically in Ref. [220].

For the general case of $\Delta \neq 0$ the limiting expressions for Z_p invariably contain $H(s)$, and limiting behaviour for cases in which the latter quantity is not equal to one are not easily broken down into simpler circuit elements. However, the limiting behaviour for $\Delta = 0$ given above will serve as a basis for comparison with calculations using the full expressions to be presented below.

For small ν the sinh and cosh functions of Z_p^m in Eq. (7.50) can be expanded to give

$$Z_p^m \approx -\frac{RT}{c_e}\frac{B}{FA}\frac{Z_D Y_f}{H(s)}\left(\frac{1}{\kappa}+\frac{1}{\sigma}\right)\frac{L}{\nu^2} \tag{7.58}$$

From the above we expect $Y_f \approx Z_D^{-1}$ at low ν, so that

$$Z_p^m \approx -\frac{RT}{c_e}\frac{B}{FA}\frac{1}{1-\frac{B\Delta}{\sigma A}}\left(\frac{1}{\kappa}+\frac{1}{\sigma}\right)\frac{L}{\nu^2} \tag{7.59}$$

which would be expected to give capacitance behaviour at low frequencies with the approximation for Z_D given in this frequency range in Ref. [220]. In Eq. (7.59) we also used that $H(s) \approx 1 - B\Delta/\sigma A$ in this limit, c.f. Eq. (7.34).

7.3.7 Simulation parameters

Assuming a kinetic expression of Butler-Volmer type [234] [1], c.f. Eq. (7.44) above,

$$i_f = i_0\left\{\exp\left[\frac{(1-\beta)F(\Phi_1-\Phi_2-U)}{RT}\right]-\exp\left[\frac{-\beta F(\Phi_1-\Phi_2-U)}{RT}\right]\right\} \tag{7.60}$$

The equation assumes no variation in the concentration of protons in solution. β is a symmetry factor and i_0 an exchange-current density. A direct evaluation using the formulas below Eq. (7.12) gives $B = \frac{i_0 F}{RT}$ and $A = \frac{i_0 F}{RT}(-\partial U/\partial c)$. (As noted in Ref. [220] the concentration dependence of i_0 will not affect the concentration dependence of the current).

The concentration may be estimated from unit cell dimensions and number of intercalants per unit cell. Pursuing the example given above the unit cell dimensions for a rutile is in the order of 60 cubic Angstroms (62.4 for TiO_2). Each unit cell contains two metal atoms, and if maximally one proton per metal atom is assumed (enough to fill the t_{2g} band in IrO_2) the concentration becomes in the order of $0.05\,\mathrm{mol}\cdot\mathrm{cm}^{-3}$. We somewhat arbitrarily set the concentration c_e to a fraction of this, $c_e = 0.004\,\mathrm{mol}\cdot\mathrm{cm}^{-3}$.

The diffusion coefficients and conductivities may be related through the Nernst-Einstein relation,

$$D_i = \frac{k_B T}{q_i} u_i\prime \tag{7.61}$$

where $u_i\prime$ is the mobility of species i, k_B the Boltzmann constant, q_i its charge, and D_i its diffusion coefficient, with the conductivity given as

$$\sigma = \sum_i q_i u_i\prime n_i \tag{7.62}$$

where q_i is the charge of species i and n_i is the concentration in units of cm^{-3}. The electron hole mobility in semi-conductors like silicon appear to be around $500\,\mathrm{cm}^2\cdot(\mathrm{V}\cdot\mathrm{s})^{-1}$ [235], which might serve as a point of departure. However, the resistivity of ruthenium and iridium oxides appear to be in the order of [236] $1\,\mathrm{m}\Omega\cdot\mathrm{cm}$ (for a dimensionally stable anode (DSA), thus including some porosity). Assuming a charge carrier concentration of $10^{22}\,\mathrm{cm}^{-3}$ in the oxidised state [237] the mobility then becomes rather low, in the order of $1\,\mathrm{cm}^2\,(\mathrm{Vs})^{-1}$. (Note that the definitions of

[1] This assumes that adsorption is not important in the ion transfer. In case this is not a good approximation adsorption can easily be worked into the theory [219].

mobility and conductivity in Equations (7.61) and (7.62) do not correspond entirely to those implicit employed in the balance of this work [229], in which the conductivity is defined as $\sigma = F^2 \sum_i z_i^2 u_i c_i$, c.f. Eq. (7.21). The mobilities are therefore related as $u_i\prime = |z_i| F u_i$. The Nernst-Einstein relation, Eq. (7.61) in this case reads $D_i = RT u_i$.)

To make the base case calculations correspond to those of Ref. [220] the mobility $u_+\prime$ was set to $0.1\,\mathrm{cm}^2 \cdot (\mathrm{V} \cdot \mathrm{s})^{-1}$ for holes. In addition the conductivity of Eq. (7.62) was multiplied by an arbitrary factor of $\xi = 0.034$, as was also Δ. The mobility of proton vacancies was set to $1.7 \cdot 10^{-8} \mathrm{cm}^2 \cdot (\mathrm{V} \cdot \mathrm{s})^{-1}$. While this is probably unrealistically low for protons in, say, iridium oxide, it does give an effective diffusion coefficient of $10^{-9}\,\mathrm{cm}^2 \cdot \mathrm{s}^{-1}$ as in the reference to which we compare our results. Note that this parameter set implies that $u_+ >> u_-$, or $t_- \approx 0$, and may not be regarded as representing mixed conductivity proper. However, we will illustrate also the case for which $t_- = 0.5$ below.

The specific surface area in a volume V may be estimated by multiplying V by the volumetric density of the particles V_d (typically 0.6 for a random packing of particles [230]) and by their surface area, and dividing by their volume. Per volume, the surface area then becomes $\frac{3V_d}{R_a}$. Again, however, to compare with Ref. [220], we adjusted the packing density to 0.5.

A summary of the base case parameters is given in Table 7.1. In Table 7.2 are given parameters corresponding to those of Ref. [220] derived from the parameters in Table 7.1 and the equations above. With these numbers well-separated time

Table 7.1: Base case parameters for the impedance model.

Parameter	Value[2]	Unit	Reference
c_0	0.025	$\mathrm{mol} \cdot \mathrm{cm}^{-3}$	
c_e	0.004	$\mathrm{mol} \cdot \mathrm{cm}^{-3}$	
z_+	1		
z_-	-1		
ν_+	1		
ν_-	1		
$u_+\prime$	0.1	$\mathrm{cm}^2 \cdot (\mathrm{V} \cdot \mathrm{s})^{-1}$	See text
$u_-\prime$	$1.7 \cdot 10^{-8}$	$\mathrm{cm}^2 \cdot (\mathrm{V} \cdot \mathrm{s})^{-1}$	
i_0	$0.69 \cdot 10^{-3}$	$\mathrm{A} \cdot \mathrm{cm}^{-2}$	
$\frac{\partial U}{\partial c_e}$	20.27	$\mathrm{V} \cdot \mathrm{cm}^3 \cdot \mathrm{mol}^{-1}$	[220]
k	0	s^{-1}	
R_a	$2 \cdot 10^{-4}$	cm	See text
κ	55	$\mu\mathrm{S}\,\mathrm{cm}^{-1}$	[220]
V_d	0.5		See text
L	100	μm	[220]
C_d	10	$\mu\mathrm{F} \cdot \mathrm{cm}^{-2}$	[220]
ξ	0.034	-	
T	353.15	K	-

[2]For potential-dependent parameters at $\Phi_1 - \Phi_2 = 0V$ (In the published version the footnote

Table 7.2: Derived parameters for the base case set.

Parameter	Value[3]	Unit	Reference
$1/B$	44.06	$\Omega\,\mathrm{cm}^2$	See text
A	- 0.46	$\mathrm{A}\cdot\mathrm{cm}\cdot\mathrm{mol}^{-1}$	
D	1.0×10^{-9}	$\mathrm{cm}^2\cdot\mathrm{s}^{-1}$	
a	7500	cm^{-1}	
σ	1.3	$\mathrm{S\,cm}^{-1}$	
t_-	0		

constants for the coupled capacitive-charging and charge-transfer and the diffusion processes appear.

Eq. (7.62) will in the iridium oxide have validity limited to small values of c_e, since for larger concentrations electrons may not have negative effective mass any more and thus not be well described as holes. Also, for large vacancy concentrations the limiting factor for the protonic conductivity might be the proton concentration rather than the concentration of vacancies.

The frequency range was 0.1 mHz through 100 kHz for the calculations in Fig. 7.2 through 7.4 and 7.8. For the remainder of the calculations the range was 0.05 mHz through 100 kHz.

7.4 Results and Discussion

The impedance of the mixed case with the parameters above is compared to the corresponding impedance of the metallic electrode in Figures 7.2 and 7.3. As can be seen from the figures, the spectrum of the mixed electrode for the base parameters with $u_+ >> u_-$ is not significantly different from that of the metallic electrode. The two contributions to the spectrum of the mixed conductor (viz. Z_p and Z_p^m) are plotted separately in Fig. 7.4. Their sum has been included in the figure for comparison. Apparently, the effect of H (s) on $\mathrm{Z_p}$ is offset almost exactly by $\mathrm{Z_p^m}$, and the total impedance is that of an electronic (hole) conductor ($\mathrm{t_-} \approx 0$).

In Figures 7.5 and 7.6 we display the results of a calculation in which the proton-vacancy mobility has been set to $0.1cm^2\,(Vs)^{-1}$. As apparent from the results, $Z_p + Z_p^m$ is now quite different from the metallic electrode in the low-frequency range, but not at all in the high-frequency end.

The impedance for the mixed conducting electrode as a function of A is shown in Fig. 7.7 for $u_+\prime = u_-\prime = 0.1cm^2\,(Vs)^{-1}$. However, the basic shape of the spectra are retained and show no qualitative differences from the spectra of the metallic electrode.

Calculations with $k \neq 0$ are shown in Figures 7.8 (diffusion-impedance Z_D) and 7.9 (porous electrode with mixed conductivity). In both figures the balance of the

erroneously reads: “Reference 2”.

[3]For potential-dependent parameters at $\Phi_1 - \Phi_2 = 0V$ (In the published version the footnote erroneously reads: “Reference 3”.

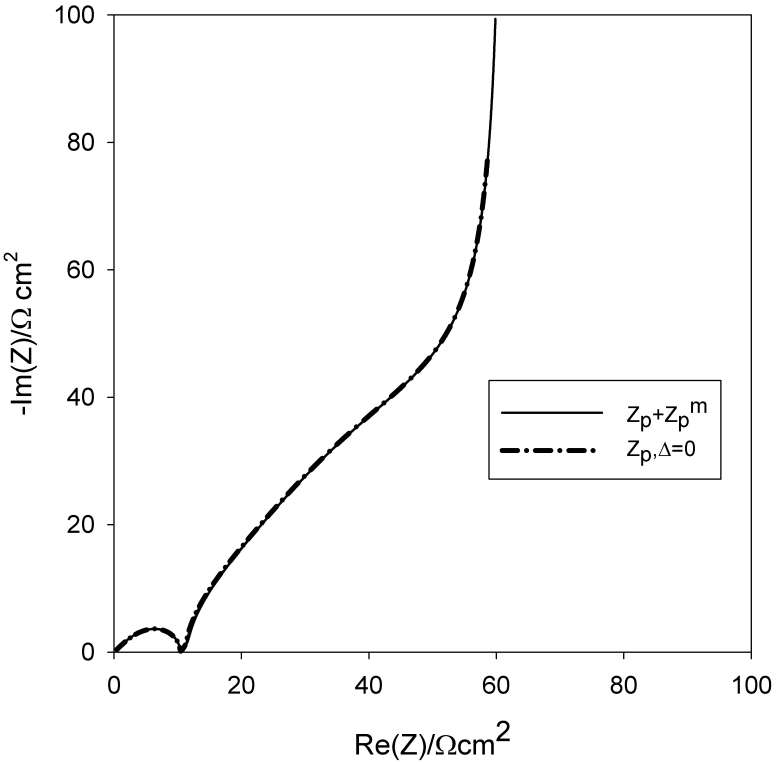

Figure 7.2: Comparison of the total impedance $\mathrm{Z_p} + \mathrm{Z_p^m}$ of the mixed conducting porous intercalation electrode with that of a metallically conducting porous intercalation electrode $\mathrm{Z_p}, \Delta = 0$ (curves overlap). Parameters are given in Table 7.1 and 7.2.

parameters take their default values, except for R_a in Fig. 7.8 which has been set to $2 \cdot 10^{-3}$ cm. As expected, the effect of finite k is to bend the impedance plane plot over at low frequencies leading, for large values of k, to a resistive behaviour. A low values of k the effect is to distort the capacitive behaviour of the diffusion element at low frequency. These effects also propagate into the impedance of the porous electrode, giving corresponding changes at low ω.

In Fig. 7.10 is shown the impedance of the mixed electrode with $k = 10^{-2}$ s^{-1} and $R_a = 2 \cdot 10^{-3}$ cm. As can be seen from the result, the impedance appears for these parameters as a series connection of two Gerischer elements, the high-frequency element corresponding to charging of the double-layer in the porous electrode, and the low frequency one to diffusion in the intercalation particles.

As is apparent from the calculations performed here, the main features of the impedance of the metallic intercalation electrode are to a certain extent retained as long as $k = 0$. This includes a Warburg-like behaviour at high frequencies, a semicircle related to charge transfer and double-layer charging at somewhat lower frequencies, and a diffusional impedance reminiscent of that of a one-dimensional blocking electrode a still lower frequencies [238], in line with the limiting behaviour discussed above.

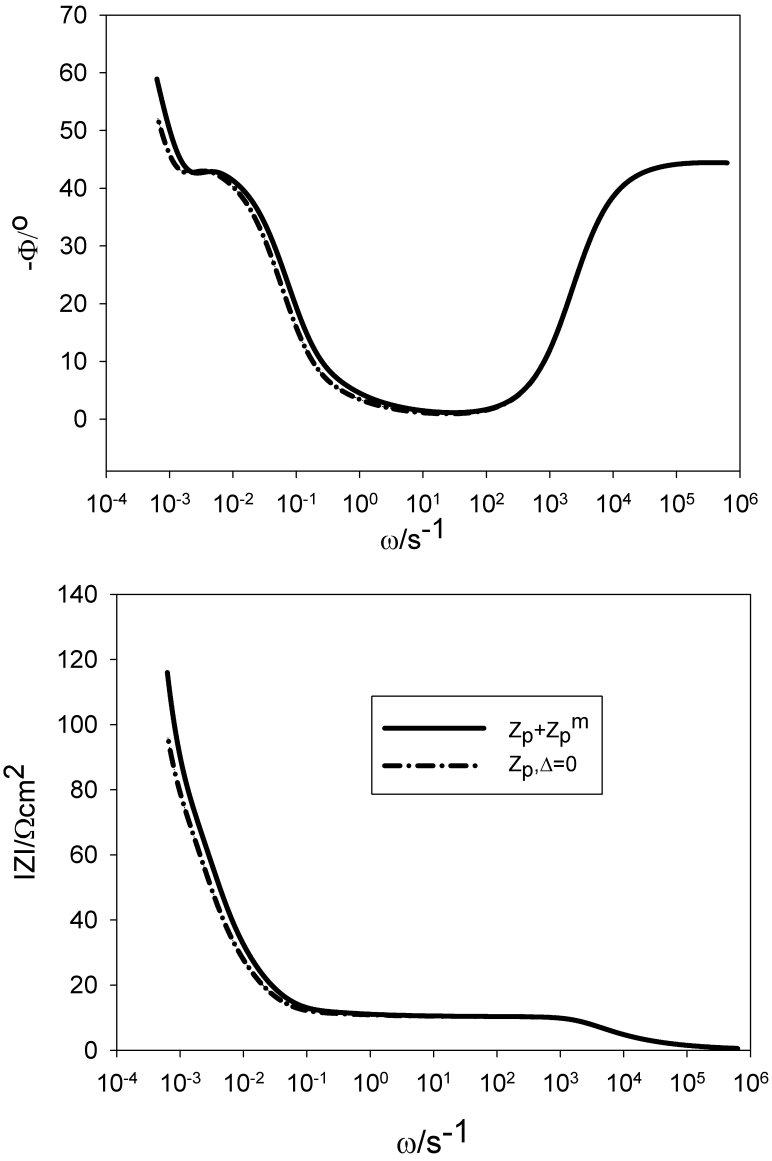

Figure 7.3: Comparison of the total impedance of the mixed conducting porous intercalation electrode with that of a metallically conducting porous intercalation electrode. Parameters are given in Table 7.1 and 7.2.

In view of the results presented here, it appears that possibilities for inferring mixed conductivity based on the impedance data alone are limited. The impedance diagrams appear to be changed only quantitatively by the presence of mixed conductivity in the electrode rather than displaying qualitatively new features that can be used to draw conclusion about the processes occurring at the electrode [239].

One possibility, in principle, is to fit the data to the model for the porous mixed electrode and from the fitted parameters evaluate the breakpoint frequency $\omega_D = D/R_a^2$. If this frequency does not correspond to the experimental break-point frequency this may be taken as an indication of mixed conductivity the electrode. However, the experimental break-point frequency will not be very sharply defined,

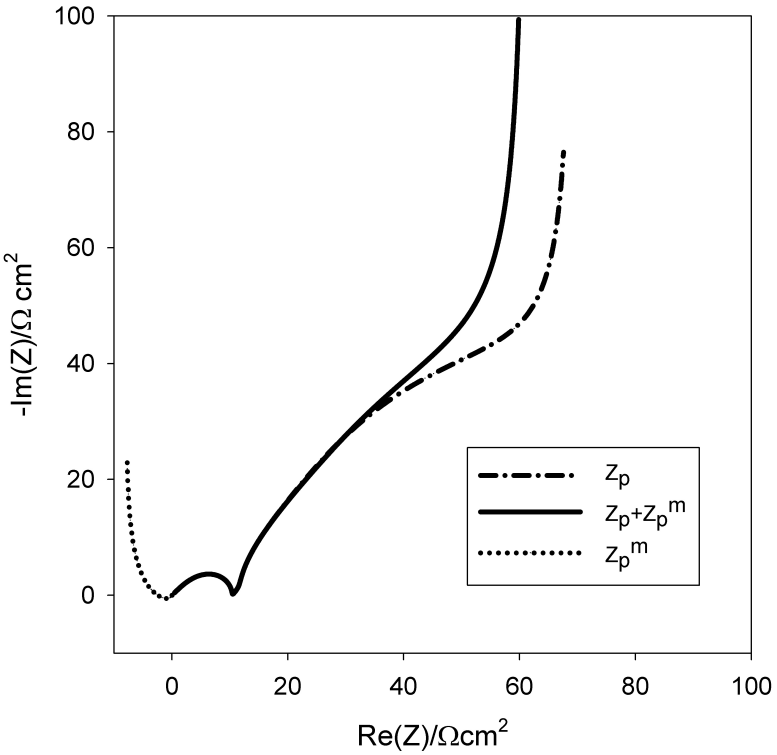

Figure 7.4: The two contributions to the impedance of the mixed conducting porous intercalation electrode Z_p (Eq. (7.43)) and Z_p^m (Eq. (7.50)) plotted separately. A plot of $Z_p + Z_p^m$ has been included for comparison. Parameters are given in Table 7.1 and 7.2.

and various non-idealities may serve to distort the fitted values. There may also be problems determining all the required variables precisely, such as particle size (or size distributions [220]). Mixed conductivity and transitions to or from this type of conductivity will therefore in all probability have to be inferred from separate measurements.

Importantly, though, the deviations in quantitative behaviour will affect the evaluation of parameters of the model. From the calculations presented here, the high-frequency deviations appear to be totally negligible, whereas the low-frequency discrepancies are certainly significant. The interpretation of the impedance of a porous intercalation electrode with mixed conductivity in terms of the expression Z_p (with $H(s) = 1$) will obviously lead to imprecise values for the diffusion coefficient.

Somewhat surprisingly in view of the logarithmic dependence on the concentration the impedance Z_p^m appears to represent a significant contribution to the corrections to the impedance function of a purely metallic electrode. The contributions to these discrepancies from the effect of $H(s)$ on Z_p appears to be equally important, c.f. Fig. 7.4. (These effects cancel almost exactly when $t_- \approx 0$, Fig. 7.2 and 7.3.) This implies that the transport process from particle to particle is not well described by Ohm's law for the parameter sets employed here. This is reasonable since the gradients in the concentration c (in x) are related to the gradients

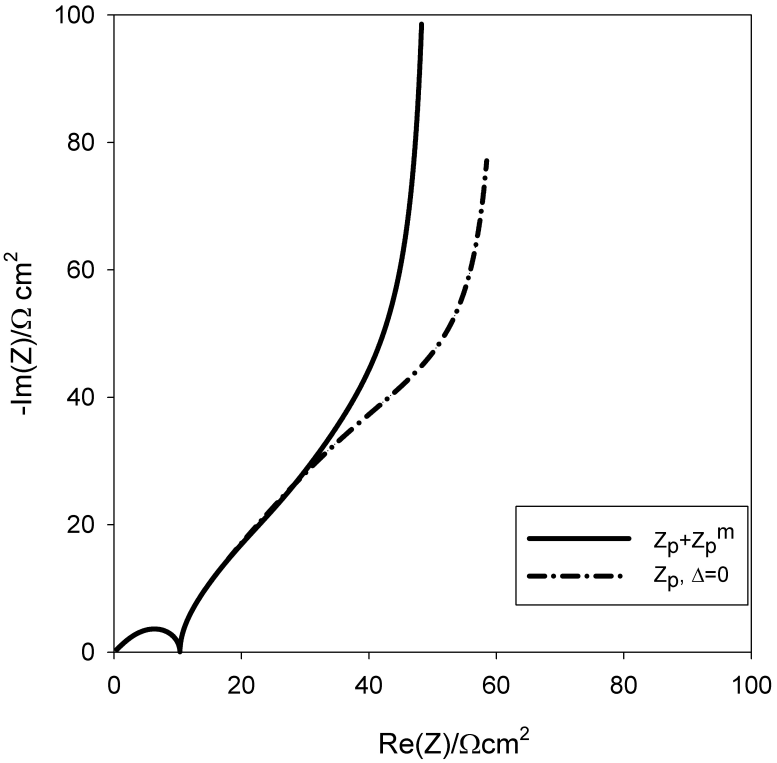

Figure 7.5: The impedance $\mathrm{Z_p} + \mathrm{Z_p^m}$ for a proton-vacancy mobility of $u_{-\prime} = 0.1\ \mathrm{cm^2\,(V\,s)^{-1}}$. All other parameters are given in Table 7.1 and 7.2. A calculation for the metallic electrode has been included for comparison ($Z_p, \Delta = 0$).

in $\Phi_1 - \Phi_2$ through Eqs. (7.12) and (7.11). The influence of the concentration term of Eq. (7.21) then depends solely on the parameters employed. A result of the parameter estimates made in the previous section is that one may expect for cases with mixed conductivity that the concentration gradient will play a significant role in Eq. (7.21).

Charge transfer resistance and capacitance at the support interface may change the impedance associated with this interface, Eq. (7.50). However, as a linearised kinetic model would be appropriate, the same impedance function would apply for the charge-transfer resistance, but with different parameters. A double-layer capacitance for this interface would be trivially included.

The model will not always produce a convincing straight line at 45^o angle with the real axis corresponding to one-dimensional semi-infinite diffusion, c.f. Figure 7.2. Meyers et al. [220] have shown that for spherical diffusion there is an intermediate frequency range neither corresponding to semi-infinite one-dimensional diffusion nor to low-frequency diffusive capacitive behaviour. An impedance corresponding to one-dimensional semi-infinite diffusion might thus only occur at the very highest frequencies of the frequency range in which diffusion dominates the impedance, c.f. their Eq. (27). At intermediate frequencies a more complicated behaviour may result [220]. As alluded to by Meyers et al. [220], the latter is a consequence

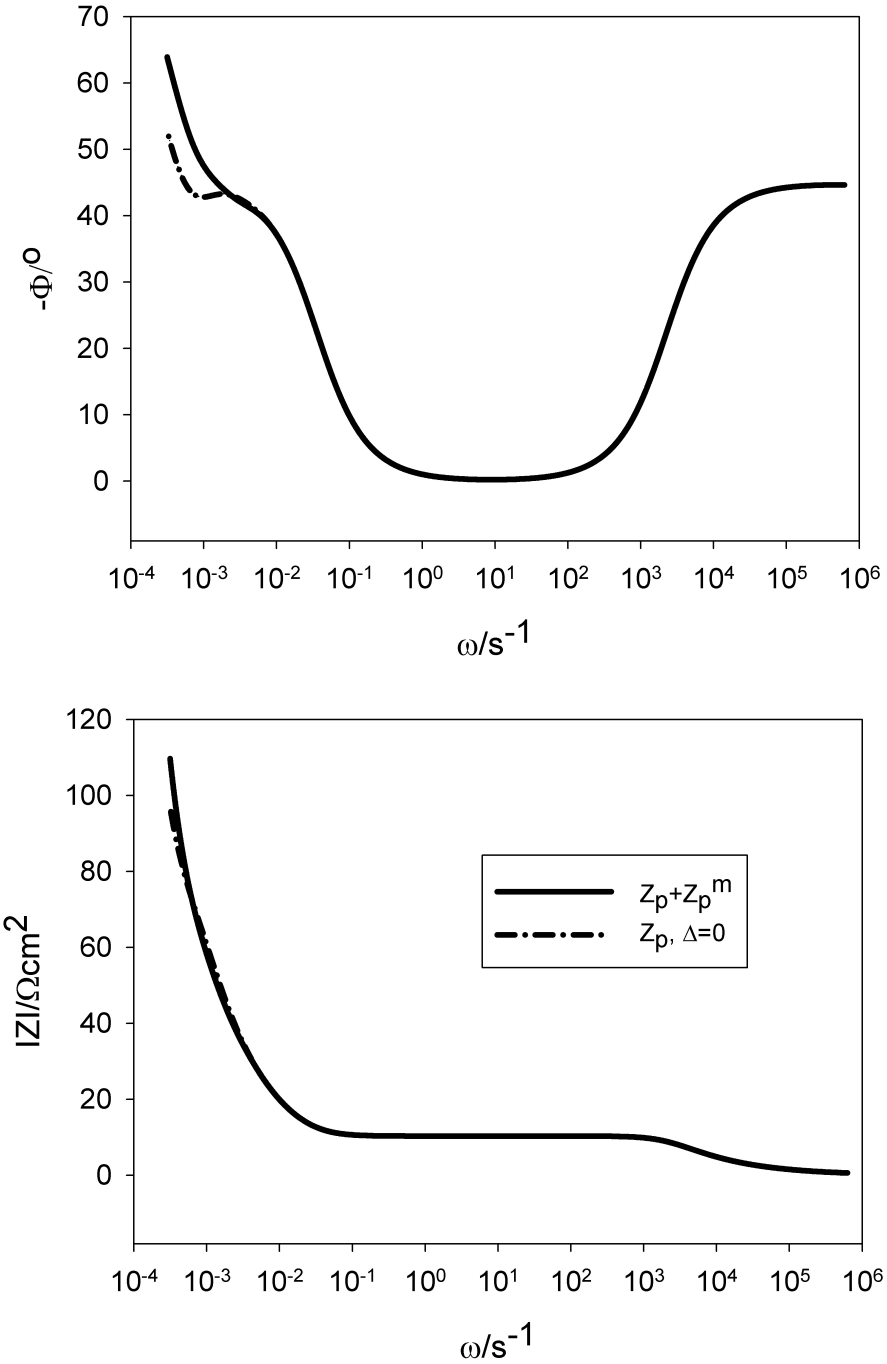

Figure 7.6: The impedance $Z_p + Z_p^m$ for a proton-vacancy mobility of $u_{-\prime} = 0.1\ \mathrm{cm^2\,(V\,s)^{-1}}$. All other parameters are given in Table 7.1 and 7.2. A calculation for the metallic electrode has been included for comparison ($Z_p, \Delta = 0$).

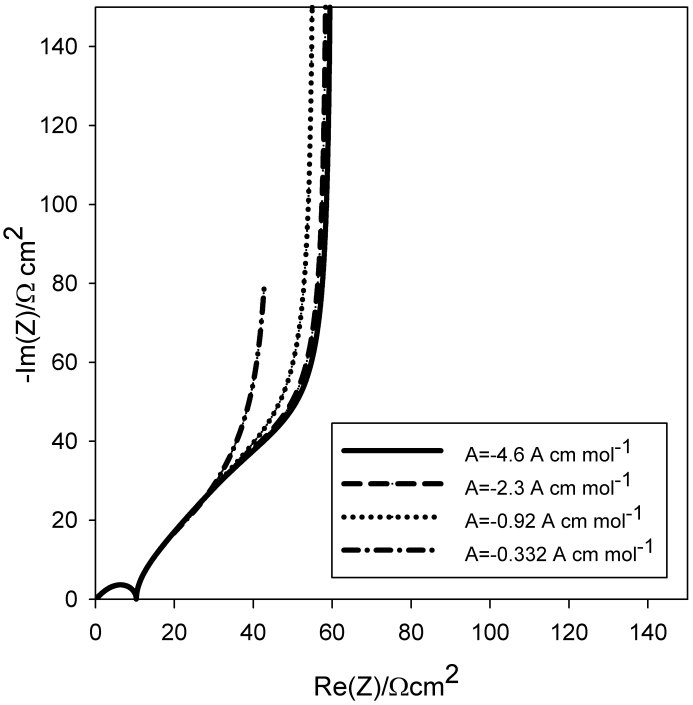

Figure 7.7: The porous mixed electrode impedance $Z_p + Z_p^m$ as a function of $A = \left(\frac{\partial i_f}{\partial c}\right)_{\Phi_1 - \Phi_2}$. The proton-vacancy mobility is $u_{-\prime} = 0.1\ \mathrm{cm^2\,(V\,s)^{-1}}$. All other parameters are given in Table 7.1 and 7.2. (The figure is an expanded view, and the maximum value of -Im(Z) for all curves except that of $A = -0.332 A \cdot cm \cdot mol^{-1}$ were larger than the maxim value of the imaginary axis.)

of the penetration depth being large enough that curvature affects the diffusion process so that it can no longer be regarded as one-dimensional. Another reason for deviations from a 45° line that applies to mixed electrodes only can be found in Figure 7.4, which illustrates the effect of the impedance Z_p^m, Eq. (7.50). Depending on the parameters this impedance may also tend to distort the diffusive part of the impedance, although this effect does not appear to be significant for the parameter set employed in Figure 7.4.

The model presented here should find application in a number of systems other than the iridium-oxide example employed here, such as for example $LiFePO_4$ [223]. A number of issues such as particle-radius distributions [220], electrolyte diffusion [222, 240] (not relevant with Nafion-oxide composites), etc have been neglected. We have, however, deliberately concentrated on features of the impedance spectra for which the mixed-conductivity *per se* would have an influence while still keeping the model relatively complete.

We would also like to point out that models of mixed conductivity in the matrix, like our own, are not simply to be regarded as equivalent to or inverse of models including mixed conductivity in the electrolyte only. The models of La Mantia et al. [240] and Sikha and White [222] would therefore not serve as a repre-

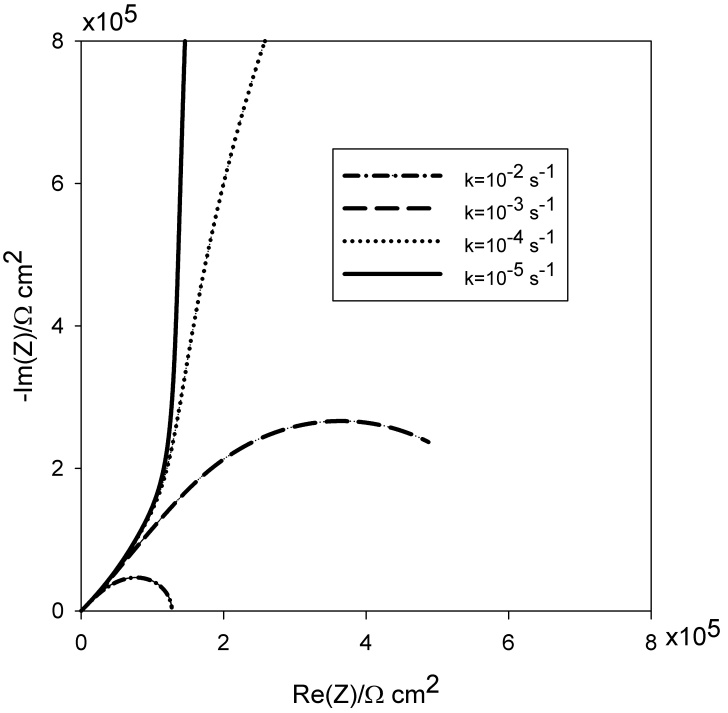

Figure 7.8: The spherical Gerischer element according to Eq. (7.20) for various values of $k = 1 \cdot 10^{-5}\,\mathrm{s}^{-1}$ through $k = 1 \cdot 10^{-2}\,\mathrm{s}^{-1}$. For this calculation R_a was set to $2 \cdot 10^{-3}\,\mathrm{cm}$. All other relevant parameters are given in Table 7.1 and 7.2.

sentation of an electrode with mixed conductivity in the matrix. A major reason for this is that the current in the matrix is linked to the diffusion in the spherical agglomerates through Eq. (7.21). The concentration appearing in this equation is the concentration at $r = R_a$ for a particle at x. The current in the matrix in the x-direction is therefore coupled to a transport process in the radial direction. In a model for binary transport in the electrolyte rather than the matrix, the current in the x-direction is coupled to a diffusion equation also in the x-direction [222], which is physically different.

Another and important difference between the case of mixed conductivity in the matrix and mixed conductivity in the electrolyte is represented by Eq. (7.50), i.e. in the way the measured electrode potential is related to the concentration of the diffusing species.

The approximation of neglecting the particle fluxes through necks when calculating the single-particle impedances may seem to be inconsistent with the inclusion of the diffusive term in Eq. (7.21). However, as argued above, one expects the influx of species at one side of the particle to be compensated by the outflux at the other, and this is more properly viewed as an approximation in terms of the dependence of the concentration in the particles on ϑ and φ. It should then be realised that similar approximations are implicit in the intercalation-particle model for metal electrodes, since modelling the electrode particles as spherically symmetric is in itself an approximation. The diffusion lengths (particle radius) would therefore become dependent on ϑ and φ. Also, since a certain degree of faceting etc is to be expected,

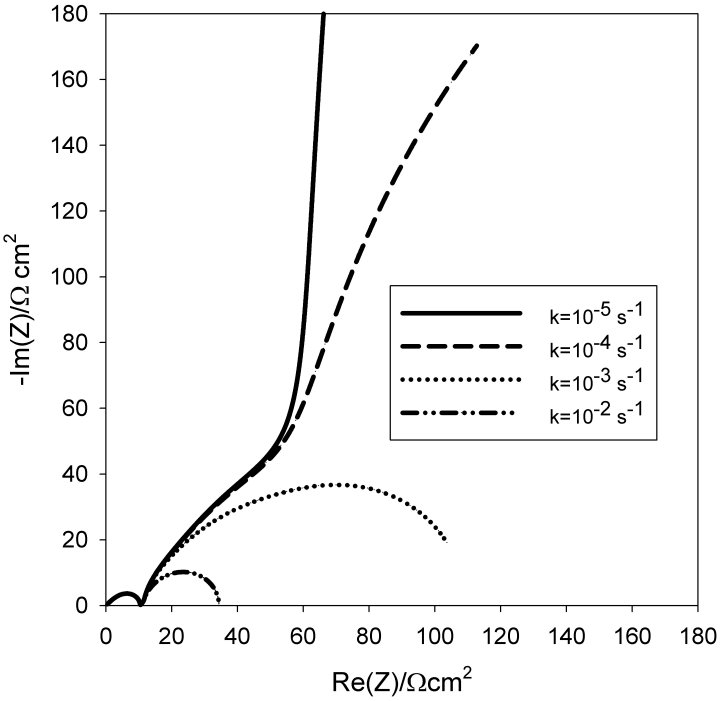

Figure 7.9: The porous mixed electrode impedance for various values of k in the range $k = 1 \cdot 10^{-5}\,\mathrm{s}^{-1}$ through $k = 1 \cdot 10^{-2}\,\mathrm{s}^{-1}$. For this calculation R_a was set to the standard value $2 \cdot 10^{-4}\,\mathrm{cm}$. All other parameters are given in Table 7.1 and 7.2.

even the kinetics of intercalant inclusion may differ from facet to facet as for the kinetics of other electrochemical reactions. Finally, for necks of finite widths there may be diffusive transport from particle to particle also for metallic electrodes, and which is normally not included. For these electrodes, however, the gradients Φ_1 and c are decoupled, and the inclusion of c in Eq. (7.21) is not relevant.

The assumption of neglecting space charges in the solid is an appropriate one for the parameter sets employed in the simulations here. The Debye length for a 0.1 mol dm^{-3} aqueous solution of a univalent electrolyte at 25 °C is 0.96 nm [241]. Since the Debye length varies in inverse proportion to the square root of the concentration, the substantially larger concentrations employed in this work should render the Debye length substantially smaller than 0.96 nm. Also, water is a highly polar solvent with a high dielectric constant. Since the Debye length is proportional to the square root of the dielectric constant, this would be expected to reduce the Debye-length further in a solid.

The space-charge dimensions thus appear to be typically very much smaller than those of the particles for the parameters employed here. However, these numbers do serve as a reminder of some of the important limitations inherent in the model. For semiconductors with carrier concentrations in the range 10^{14} through 10^{18} cm^{-3}, typical extensions of space charges appears to be in the range 10 nm through 100 nm [242], which may be significant compared to the value for R_a used here.

Finally, we also note that similar conclusions concerning space-charges were

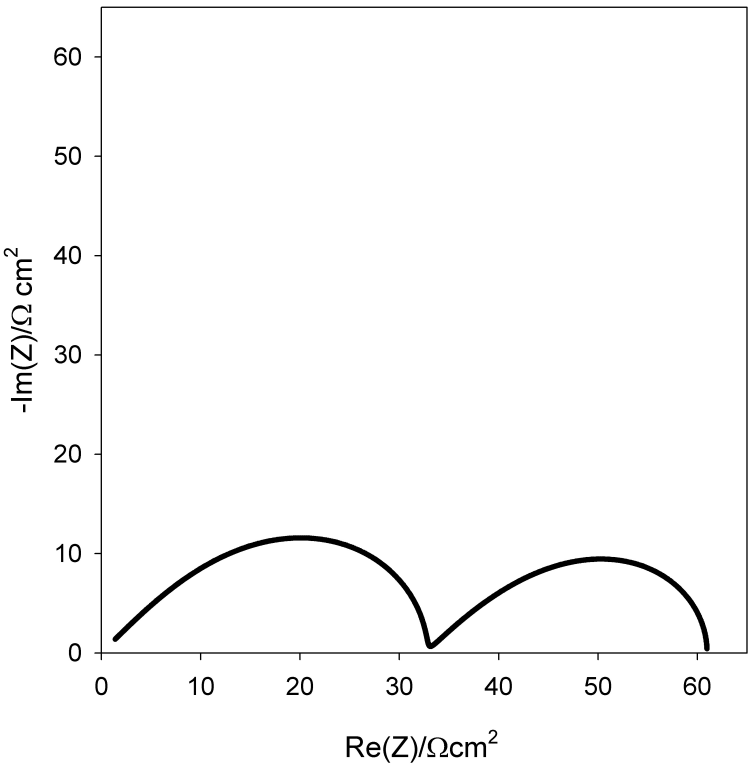

Figure 7.10: The porous mixed electrode impedance for $k = 1 \cdot 10^{-2}\ \mathrm{s}^{-1}$, $R_a = 2 \cdot 10^{-3}$ cm. All other parameters are given in Table 7.1 and 7.2.

drawn in the model of Glarum and Marshall [129], albeit for a different geometry.

7.5 Conclusions

An impedance model for a porous intercalation electrode with mixed conductivity based on the the assumption of spherical particles and dilute-solution theory has been established. The impedance diagrams emerging from the theory are to qualitatively similar to those of porous intercalation electrodes with metallic conductivity for typical parameter sets. However, significant quantitative deviations may appear in mixed conductors, in particular in the low-frequency end of the spectrum. These deviations may, if interpreted with the impedance functions for metallic electrodes, lead to significant deviations in the estimates for diffusion coefficient and possibly other parameters.

A major reason for the low-frequency deviations are found in the measurement of the potential of the electrode, leading to an impedance associated with exchange of electrons in the electrode backing and electron holes in the intercalation material. A correction due to interparticle diffusion appears to be equally important.

A Gerischer-element for spherical diffusion displays both capacitive and resistive low-frequency behaviour, depending on the reaction rate. This element may also be relevant for porous, nano-structured ex- or intrinsic semiconductors in which electrons and holes recombine at finite rates.

Acknowledgements

Part of this work was funded by the Research Council of Norway under contract 159012.

7.6 List of symbols

A	$\partial i_f/\partial c$, $\mathrm{A}\cdot\mathrm{mol}^{-1}\cdot\mathrm{cm}$
a	Surface area per volume, cm^{-1}
B	$\partial i_f/\partial\left(\Phi_1-\Phi_2\right)$, $\Omega^{-1}\cdot\mathrm{cm}^{-2}$
C_d	Double-layer capacitance, $\mu\mathrm{F}\cdot\mathrm{cm}^{-2}$
c_i, c	Concentration of species i, concentration of neutral hole-vacancy pair, $\mathrm{mol}\cdot\mathrm{cm}^{-3}$
c_e	Equilibrium concentration of neutral hole–vacancy pairs, $\mathrm{mol}\cdot\mathrm{cm}^{-3}$
c_0	Maxmimum equilibrium concentration of neutral hole-vacancy pairs, $\mathrm{mol}\cdot\mathrm{cm}^{-3}$
c	Eq. (7.40), $\Omega^{-1}\mathrm{cm}^{-2}$
D_i, D	Diffusion coefficient of species i, ambipolar diffusion coefficient, $\mathrm{cm}^2\cdot\mathrm{s}^{-1}$
F	Faraday number, 96485 $\mathrm{C\,mol}^{-1}$
G	Eq. (7.18), $\mathrm{cm}^{-1}\cdot\mathrm{s}^{-1}$
H	Eq. (7.33)

H_H^x	An intercalant hydrogen in the oxide lattice of effective zero charge
$h^\bullet$	An electron hole in the oxide lattice of effective positive charge
I	Total current density in electrode and electrolyte phases, $\mathrm{A \cdot cm^{-2}}$
Im()	Imaginary part of quantity in parentheses
i_0	Exchange-current density, $\mathrm{A \cdot cm^{-2}}$
i, i_1, i_2	Current density, current densities in electrode and electrolyte phases, $\mathrm{A \cdot cm^{-2}}$
i_s	Projected current density in the x-direction through interparticle necks, $\mathrm{A \cdot cm^{-2}}$
k	Rate constant, $\mathrm{s^{-1}}$
k_B	Boltzmann constant, $1.38 \cdot 10^{-23} \mathrm{J \cdot K^{-1}}$
q, q_i	Charge in double layer, charge of species i, C
L	Electrode thickness, cm
N_i	Flux of species i, $\mathrm{mol \cdot cm^{-2} \cdot s^{-1}}$
n_i	Concentration of species i, $\mathrm{cm^{-3}}$
R_a	Particle radius, cm
R	Gas constant, $8.314\ \mathrm{J\,K^{-1}mol^{-1}}$
R_c	Reaction rate, Eq. (7.5) $\mathrm{mol \cdot cm^{-3} s^{-1}}$
Re()	Real part of quantity in parentheses
r	Radial coordinate, cm
s	Laplace-variable
T	Temperature, K
t_-	Transference number of negatively charged species
U	Open-circuit potential, V
u_i	Mobility of species i, $\mathrm{cm^2 \cdot mol\,(J \cdot s)^{-1}}$
$u_i\prime$	Mobility of species i, $\mathrm{cm^2\,(V \cdot s)^{-1}}$
$V_H\prime$	An intercalant-hydrogen vacancy in the oxide lattice of effective negative charge
v	Insertion rate ($v > 0$) of intercalant vacancies at surface of particle, $\mathrm{mol \cdot cm^{-2} \cdot s^{-1}}$
x	Coordinate normal to the electrode, cm
Y_f	Faradaic admittance, Eq. (7.20), $\mathrm{\Omega^{-1} \cdot cm^{-2}}$
y	Dimensionless coordinate, x/L
Z	Impedance, $\mathrm{\Omega \cdot cm^2}$
Z_p, Z_p^m	Impedances, Eqs. (7.43) and (7.50), $\mathrm{\Omega \cdot cm^2}$
$Z_D\prime$, Z_D	Diffusional impedances, Eq. (7.20) and $Z_D = -(A/BF)\, Z_D\prime$, $\mathrm{\Omega \cdot cm^2}$
z_-, z_+	Charge numbers of species of negative and positive charge

Greek

α	$\sqrt{(j\omega + k)/D}$
β	Symmetry factor
Δ	$\xi z_+ \nu_+ F\,(D_+ - D_-)$, $\mathrm{C\,cm^2\,mol^{-1}\,s^{-1}}$

ϑ	Polar coordinate angle, Eq. (7.10)
κ	Electrolyte conductivity, $\Omega^{-1}\mathrm{cm}^{-1}$
μ_e	Electrochemical potential of electrons in electrode backing, J mol^{-1}
μ_h	Electrochemical potential of holes in electrode, J mol^{-1}
ν	Eq. (7.40)
ν_+	Number of holes per electron extracted
ν_-	Number of proton vacancies per electron extracted
φ	Polar coordinate angle, Eq. (7.10)
ξ	Ratio of neck area to electrode area
σ	Electrode conductivity, $\Omega^{-1}\mathrm{cm}^{-1}$
Φ_1, Φ_2	Electrode and electrolyte potentials, V
ω	Angular frequency, s^{-1}

Subscripts

i	Species number
1	Electrode phase
2	Electrolyte phase
f	Faradaic
s	Neck

Superscripts

$\bullet$	Effectively positive charge carrier in solid
$\prime$	Effectively negative charge carrier in solid

Overline

$\tilde{}$	Time-dependent part of quantity

Others

$\mathcal{L}\{\}$	Laplace-transform

Chapter 8

An Impedance Model for Anodically Formed Iridium Oxide Films

Is not included due to copyright

Chapter 9

The impedance of iridium-tin oxide

Is not included due to copyright

Chapter 10

Iridium-ruthenium oxide powders

10.1 Abstract

Possible interactions between iridium and ruthenium in mixed iridium-ruthenium oxide oxygen evolution catalysts were investigated. Both chemically and physically mixed iridium-ruthenium oxide catalysts were prepared. The oxides were characterised by X-ray diffraction, cyclic voltammetry (CV) and steady state polarisation measurements.

The diffraction data indicates that the chemically mixed oxides segregates into a nearly pure iridium oxide phase and a mixed phase different from pure ruthenium oxide. The segregation increases with increasing heat treatment temperature. The conclusion is supported by the electrochemical measurements. The rate of the oxygen evolution reaction is dependant on the ruthenium content for both the chemically and the physically mixed oxides.

10.2 Introduction

For the oxygen evolution reaction (OER) in acidic electrolytes noble metal oxide catalysts are the most active and stable. Ruthenium oxide is the most active catalyst, however the stability is not sufficient for practical applications. Iridium oxide is both stable and almost as active as ruthenium oxide. An oxide containing both elements is therefore expected to be a good catalyst for the OER [156, 252, 253].

The elements in the catalyst must be mixed on an atomic level and form common energy bands if there is to be an interaction between them. This can only happen if the energy bands of the individual elements are sufficiently close to each other. If a common valence band is formed, the position of it should change with composition. This is an effect of different band filling. A change in band position implies a change in the Fermi level. This implies a change in the oxidation potential, and thus should also affect the oxygen evolution reaction, and there should also be a change in the cyclic voltammograms.

Kötz and Stucki [252] prepared sputtered films of iridium-ruthenium oxide and investigated them electrochemically. They showed that the potentials for the OER at 0.1 mA/cm^2 and the redox peaks in the CVs shifted with composition, indicat-

ing an interaction between iridium and ruthenium. A similar shift was also seen by Kodintsev *et al.* [254]. As powders are more convenient as catalysts in polymer electrolyte membrane water electrolysers (PEM WE) the same experiments should be performed for mixed iridium-ruthenium oxide powders. This is particularly important as the stability of nano sized crystallite might not be the same as for lager crystallites. For iridium oxide catalysts prepared by the hydrolysis method the crystallite size can be quite small, in the 20 nm range [44]. Even smaller crystallite sizes, in the 2–3 nm range were reported by Cheng and co-workers [255] for iridium-ruthenium oxides prepared by the Adams' fusion method. The rate of the OER was also found to increase and the onset potential for the OER decrease with increasing ruthenium content.

To simplify the interpretation of the results the synthesised iridium-ruthenium oxides were compared with physical mixtures of pure iridium and ruthenium oxide. Physical mixtures differ from chemical mixtures by the mixing level. Chemical mixtures are mixed on an atomic lever, whilst physical mixtures are mixtures of micro or nano sized particles of the pure components [94].

Comparison between physical and chemical mixtures of oxides should tell if the oxides create common structures or if they create segregated phases. In the case where common structures are created one would expect the electrochemical response of the oxide to be different from the physical mixture. The response of a physical mixture is expected to be a superimposition of the response of the two pure oxides, dependent on the composition. In the case of chemical mixtures that create common structures the response should show features intermittent of the pure oxides.

An XRD study by Balko and Davidson [170] of iridium-ruthenium oxides prepared by the Adams fusion method revealed the formation of a solid solution over the whole composition range. Iridium-ruthenium oxides have been investigated by EXAFS (Extended X-ray Adsorption Fine Structure) by Arikawa *et al.* [173] using DSA-type electrodes whilst Marshal [172] used oxide powders synthesized by the hydrolysis method. However, in both cases the conclusion was that a true solid solution was formed between IrO_2 and RuO_2. For RuO_2–IrO_2–TiO_2 mixed oxides prepared by the sol-gel method Takasu *et al.* [148] found uniform solid solutions only for TiO_2 deficient compositions. The other samples showed evidence of multiple phases being formed. However, for DSA-type electrodes solid solution has been observed for the same system [192]. Some evidence of segregation in iridium rich iridium-ruthenium oxides was found by Roginskaya and co-workers [253].

Theoretical calculations, DFT, performed by Mowbray and co-workers [176] show that the formation energy for IrO_2 (110) surfaces and nanoparticles in vacuum is significantly higher than that for RuO_2. A mixed iridium-ruthenium oxide would therefore be expected to be enriched in the surface by ruthenium. On the other hand the situation for oxides covered with adsorbed oxygen species is expected to be opposite. As iridium has a higher affinity for oxygen than ruthenium, iridium will segregate to the surface [175]. On thermally prepared RuO_2 and IrO_2 mixed oxide catalysts a surface enrichment of iridium has indeed been observed both by XPS and CVs [177, 178]. Iridium preferentially moves to the coordinatively unsaturated sites (cus), the sites active for oxygen evolution, on the (110) surface [175]. The bridge sites, where ruthenium can be found, are not active for the OER. Thus it

can be expected that for a mixed iridium-ruthenium oxide iridium will dominate the activity for the OER as soon as the number of iridium atoms present is sufficient to cover the cus positions.

The purpose of this work is to prepare mixed iridium-ruthenium oxide catalysts for oxygen evolution in acidic electrolytes. Electrochemical measurements and X-ray diffraction are used to characterise the catalysts. The characterisation of the catalysts, including comparisons with physical mixtures of pure iridium and ruthenium oxide, will show that homogeneous chemically mixed oxides were not prepared. Instead multi phase systems are formed.

10.3 Experimental

All oxides were prepared by the hydrolysis method. The precursors, $H_2IrCl_6 \cdot 4H_2O$ (OMG AG & Co. KG, 99.2 %) and $RuCl_3$ (Alfa Aesar, 99.9 %), were dissolved in aqueous sodium hydroxide solution (0.2 M, J. T. Baker, Baker Analyzed). The resulting solution was stirred at 80 °C for one hour, before cooling and adjusting the pH to 8 with nitric acid (Merck, p.a.). After an additional 30 minutes of stirring and heating at 80 °C, the precipitate was separated and washed by centrifuging. The precipitate was heat treated for 30 minutes in air at 600 °C, unless otherwise stated. Details of the method can be found in Marshall *et al.* [146].

The electrodes were prepared by the thin film technique [256]. The oxide catalysts were dispersed in water (1 mg/mL) in an ultrasound bath. Two or three portions of 20 µL of the dispersion were pipetted onto a glassy carbon RDE with diameter 5 mm and dried under an N_2 gas stream. A 20 µL drop of Nafion solution (1:100 in water) was applied on top and dried in the same manner. The physically mixed oxides were prepared *in situ* on the electrode by adding the pure oxide dispersions in the required ratio to the electrode.

The surface area of catalysts per mass was not the same for the different compositions. The amount of catalyst was chosen so that roughly equal currents would be obtained in the CVs. For pure iridium oxide, $Ir_{0.5}Ru_{0.5}O_2$ and the physical mix with 25 mol% IrO_2 40 µg was used. For the remaining samples 60 µg was used.

A standard three electrode electrochemical cell was used. Either a Radiometer Analytical silver–silver chloride reference electrode or a dynamic hydrogen reference electrode was used. All reported potentials are referred to the SHE scale. A Gamry Instruments Series G 300 potentiostat was used for all electrochemical measurements.

The electrolyte, 0.5 M H_2SO_4 (Merck, p.a.), was de-aerated by argon gas (AGA, 5.0 quality) before all experiments. All solutions were prepared with water tapped from a Millipore Direct-Q3 water purification system.

XRD analysis were performed on a Bruker AXS D8Focus. The data was analysed using Bruker AXS TOPAS. SEM analysis were performed on a Hitachi S-3400N SEM with an Oxford EDS system.

10.4 Results and discussion

Table 10.1 gives the desired and the actual composition of the iridium-ruthenium oxides as found by EDS. The synthesis gave compositions that were within 2 mol% of the desired composition for all three mixed oxides.

Table 10.1: The desired and actual composition, found by EDS, of the prepared oxide catalyst.

Desired comp. mol% Ir	*Actual comp.* mol% Ir
100	100
75	74
50	51
25	27
0	0

Diffractograms of pure ruthenium oxide and iridium oxide were similar to previously reported diffractograms of the oxides [44, 173]. The chemically mixed oxide samples had diffractograms intermittent to those of the pure oxides. The peaks at 2θ values of 28° and 40° were similar for all the samples. The peaks at about 54° and 35° did, however, shift with composition between the peak position in iridium and ruthenium oxide. This is in accordance with the diffractograms of the pure oxides, where iridium and ruthenium oxide both have peaks at 28° and 40°, but the two other peaks are at slightly different 2θ values.

A heat treatment study was performed on a chemically mixed iridium-ruthenium oxide catalyst with equal amounts of iridium and ruthenium. The samples were heat treated at 450, 550, 650 and 750 °C in pure oxygen for 60 min. Diffractograms of the samples are given in Figure 10.1. The XRD data was analysed using structure-less full pattern fitting on Bruker AXS TOPAS. The shift in the crystallite size and the unit cell lengths are given in Table 10.2 for the case where the system is modelled as a two phase system, and in Table 10.3 for the case where the system is modelled as a one phase system. Data analysis shows that the best fits are achieved for a two phase system as opposed to a single phase system. The error, as predicted by the modelling software, is about two times higher when the data is fitted to a single phase system as opposed to a two phase system.

The crystallite size increases with increasing heat treatment temperature, with the exception of the data for the sample heat treated at 750 °C modelled as a two phase system, see Tables 10.2 and 10.3. The lattice constant a is close to the values of pure IrO_2 and RuO_2 for all samples and for both the single and two phase fitting. This is, however, expected as a is similar for both IrO_2 and RuO_2, 4.4900 Å and 4.4919 Å respectively. A bigger change can be seen for the lattice constant c. The values of c for IrO_2 and RuO_2 are 3.1400 Å and 3.1066 Å respectively. For the single phase fitting, seen in Table 10.3, the value of c is intermediate of the two pure oxides for all heat treatment temperatures. The lattice constant c in "Phase B", see Table 10.2, shifts towards that of pure IrO_2 with increasing heat

treatment temperature, whilst c takes an intermediate value in "Phase A" for all heat treatment temperatures. The data indicates that "Phase B" shifts towards that of pure iridium oxide with increasing heat treatment temperature. In other words segregation is taking place. The other phase does not, at any heat treatment temperature, resemble that of pure ruthenium oxide.

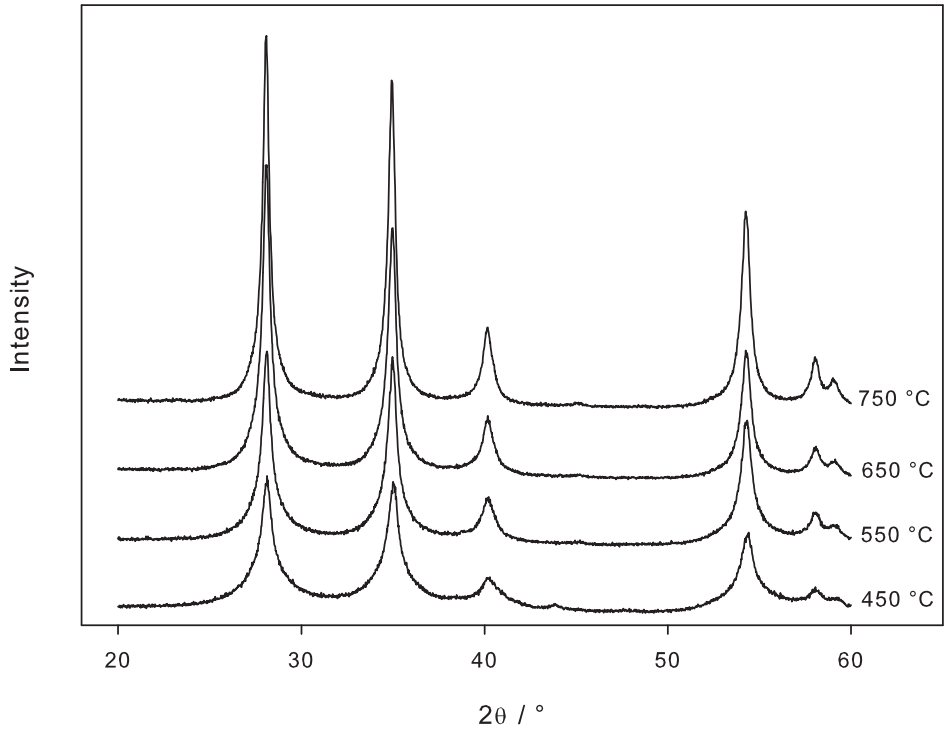

Figure 10.1: Diffractogram of $Ir_{0.5}Ru_{0.5}O_2$ heat treated at 450, 550, 650 and 750 °C for 60 min

The CV of iridium oxide, see Figure 10.2, is similar to previous results [44]. The main anodic peak is seen at 1 V and the corresponding cathodic peak at 0.9 V. The CV of ruthenium oxide, see Figure 10.2, has an anodic and cathodic peak at lower potentials, 0.6 V, than iridium oxide. However, the most noticeable difference from iridium oxide is the large cathodic current, that is twice that at other potentials, at low potentials. Capacitative behaviour also dominates the CV of ruthenium oxide to a greater extent than the CV of iridium oxide. CVs on ruthenium oxide with the same features have been observed before by Kötz and Stucki [252], although the large cathodic current at low potentials was not as pronounced. Similar CVs have also been recorded on thermally prepared RuO_2 [177] and electrochemically deposited RuO_2 [257, 258], although both studies had a more positive cathodic sweep limit than in this work. The large cathodic current at low potentials was therefore not observed. Large cathodic currents are seen on RuO_2 layers on titanium prepared by the alkoxide ink procedure for a cathodic sweep limit of −0.25 V (SCE) [259]. The same distinct cathodic peak at the lowest potentials was, however, not seen.

Table 10.2: The crystallite size, d, and unit cell lengths, a and c, as a function of heat treatment temperature for $Ir_{0.5}Ru_{0.5}O_2$ modelled as a two phase system. All samples are heat treated for 60 min.

	Phase A			Phase B		
Temp.	a	c	*d*	a	c	*d*
°C	Å	Å	nm	Å	Å	nm
450	4.488	3.119	10.54	4.487	3.130	2.99
550	4.491	3.126	18.02	4.495	3.133	4.07
650	4.491	3.126	21.13	4.496	3.138	5.16
750	4.490	3.126	16.80	4.496	3.139	5.00

Table 10.3: The crystallite size, d, and unit cell lengths, a and c, as a function of heat treatment temperature for $Ir_{0.5}Ru_{0.5}O_2$ modelled as a single phase system. All samples are heat treated for 60 min.

Temp.	a	c	*d*
°C	Å	Å	nm
450	4.489	3.121	7.71
550	4.491	3.126	10.65
650	4.491	3.127	12.93
750	4.492	3.128	15.39

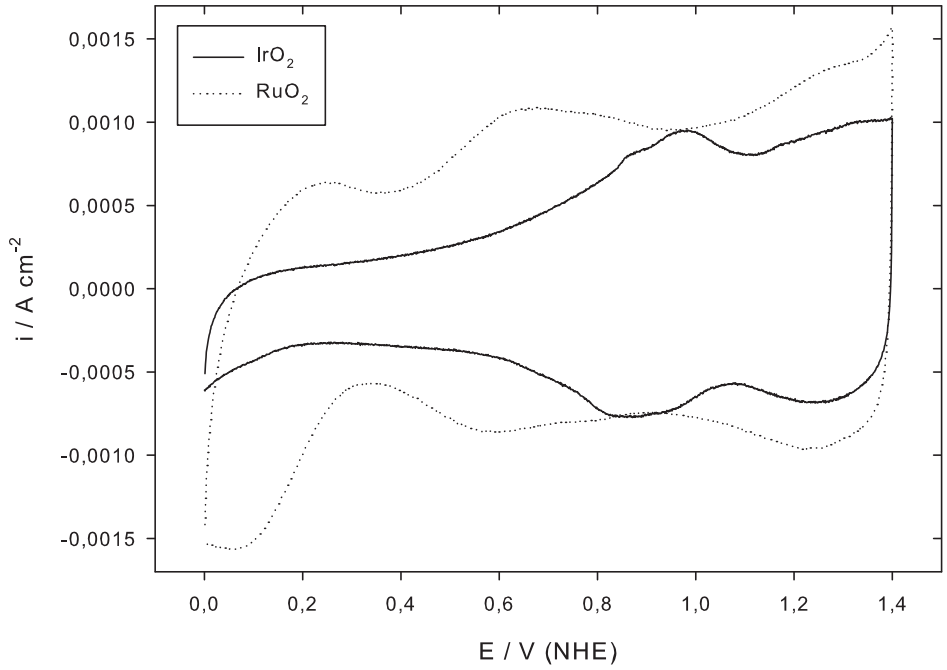

Figure 10.2: CVs of pure IrO_2 and RuO_2. 50 mV/s.

The CVs of the chemically mixed catalysts, shown in Figure 10.3, change to a small extent with composition[1]. The signal of iridium oxide seems to dominate the CV for all compositions, except at the highest potentials where the current for the anodic sweep resembles that of ruthenium oxide. The anodic peak just under 1 V is present for all the samples and is at the same potential. This peak resembles that of pure iridium oxide, see Figure 10.2. With the exception of an anodic peak at 1.2–1.3 V the CV of $Ir_{0.75}Ru_{0.25}O_2$ appears to be almost that of pure iridium oxide. The CV of $Ir_{0.25}Ru_{0.75}O_2$ does show more ruthenium oxide behaviour in that the CV is more capacitative in nature. As for the CV of $Ir_{0.5}Ru_{0.5}O_2$ an anodic peak at 1.2–1.3 V is also seen. This peak is more distinct than that of pure RuO_2.

Compared with the the CVs recorded on sputtered iridium-ruthenium oxide films prepared by Kötz and Stucki [252], the peaks are clearer in this work. Whereas the capacity of the low potential region in their work is about equal to that in the high potential region, the capacity of the high potential region in the chemically mixed samples shown in Figure 10.3 dominates. The shift in the anodic peak potential seen by Kötz and Stucki [252] for sputtered films or by Kodintsev and co-workers [254] for thermally prepared oxides was not evident for the powder oxide samples in this work. Thermally prepared iridium-ruthenium oxides are similar to the sputtered films in that the peaks of the CVs are not clear [177]. However, the capacitative nature of the thermally prepared samples is close to the powders prepared in this work. The lower annealing temperature of 400 °C used in the preparation of the thermally prepared samples is expected to give less pronounced peaks than the 600 °C heat treatment temperature used in this work, as can be seen in Figure 10.3. The anodic peak at potentials of 1.2–1.3 V, seen in Figure 10.3, has been seen before for iridium-ruthenium oxide powders prepared by the Adams' fusion method [255].

The CVs of the physical mixtures of ruthenium and iridium oxide are given in Figure 10.4. The CV of the mix with 75 mol% IrO_2 has a CV that is close to identical to that of pure iridium oxide. The same can be said for the sample with 50 mol% IrO_2. Only the sample with 25 mol% IrO_2 shows an appreciable ruthenium oxide behaviour. However, the sample with 25 mol% IrO_2 does still have an anodic peak at the same potential as the main anodic peak of iridium oxide.

Considering the difference between the chemical and physical mixes seen in Figure 10.5 it is apparent that the differences are not that significant. The CVs of the physical and chemical mixtures with the highest iridium content (75 mol% IrO_2) are close to identical. The CVs of the samples with equal amounts of iridium and ruthenium are also similar, with the exception of the anodic peak at 1.2–1.3 V mentioned previously for the chemically mixed sample. The CVs of the samples with the lowest iridium content are also quite similar, though more of the capacitative nature of pure ruthenium oxide can be seen in the CV of the physical mix.

Polarisation measurements of the pure oxides and both the chemical and physical mixed samples with equal amounts of iridium and ruthenium, are shown in Figure 10.6. The rate of the OER is highest on pure RuO_2 and slowest on IrO_2. For the mixed oxides the chemical mixture has a slightly lower rate of the OER at any

[1]The emphasis of the comparison of the different samples will be place on the shape of the CVs, and not the current.

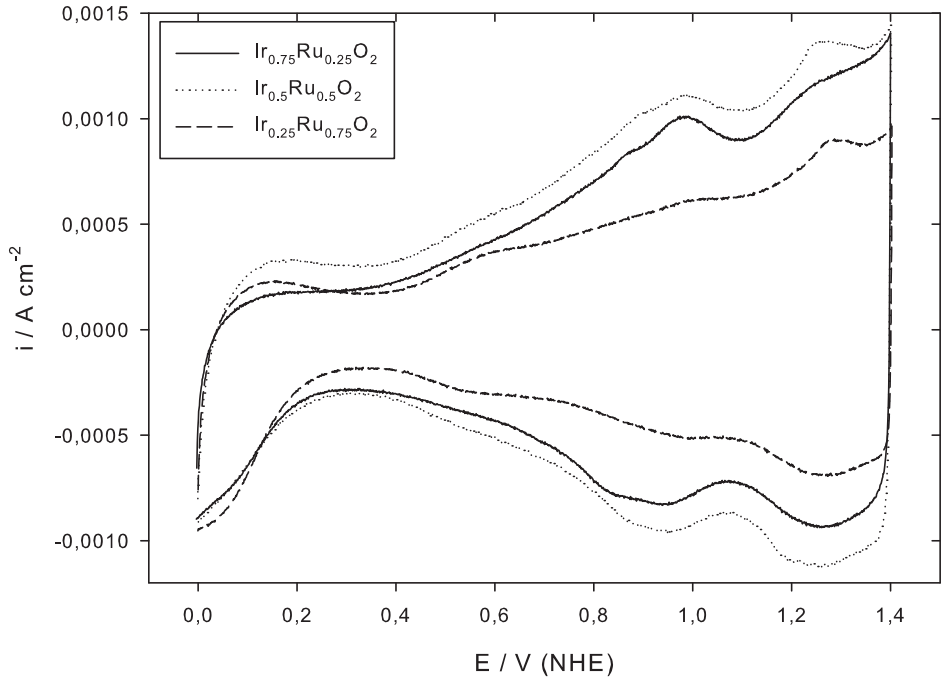

Figure 10.3: CVs of the chemical mixtures of iridium-ruthenium oxide. 50 mV/s.

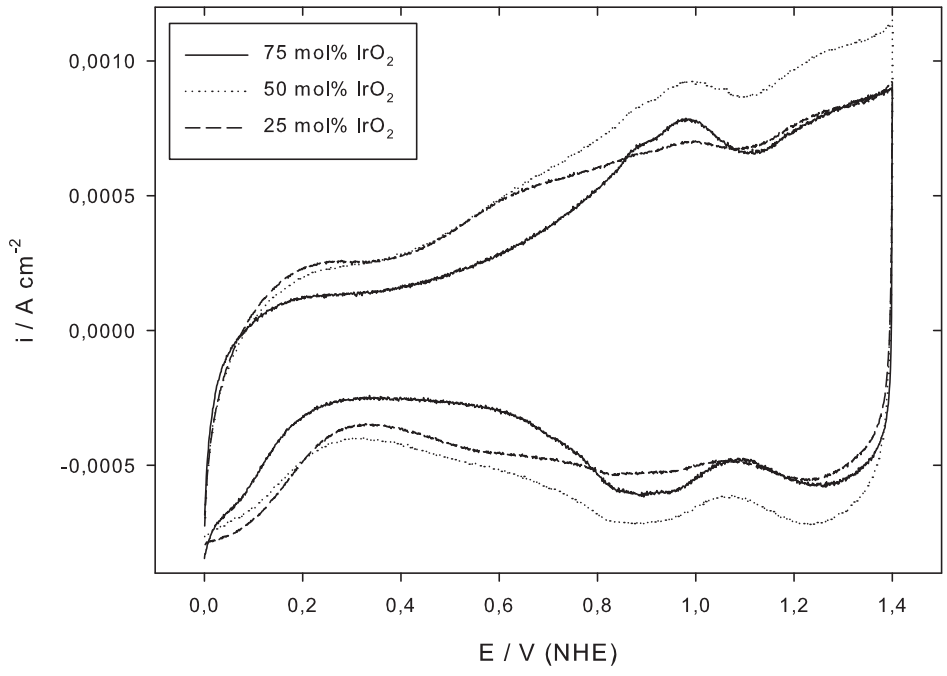

Figure 10.4: CVs of the physical mixtures of iridium oxide and ruthenium oxide. 50 mV/s.

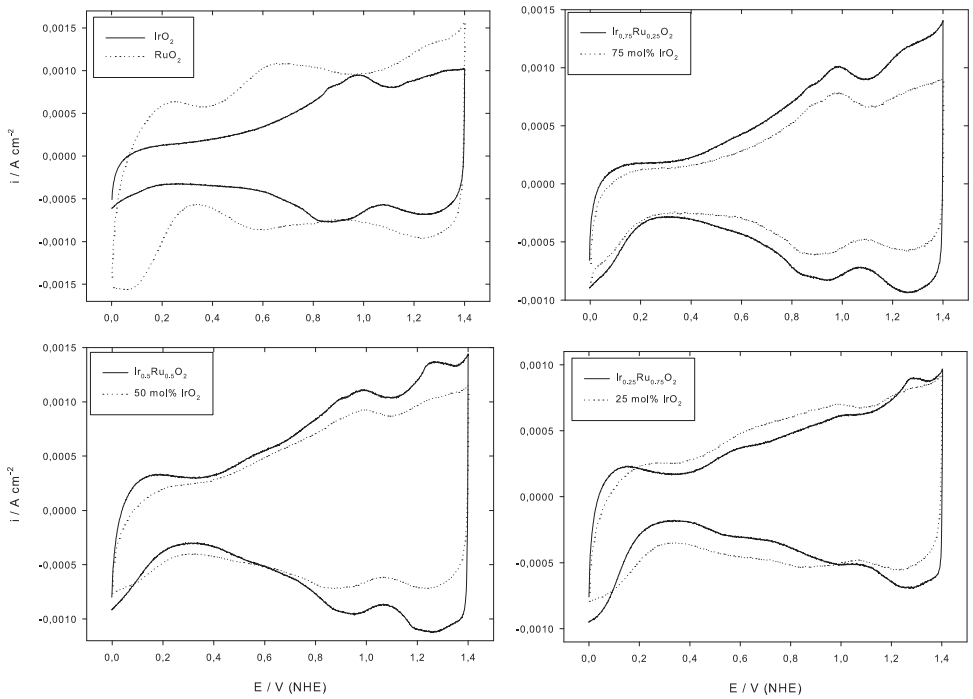

Figure 10.5: CVs of the chemical (—) and physical mixtures ($\cdots$) of iridium oxide and ruthenium oxide. The CVs of pure IrO_2 (—) and RuO_2 ($\cdots$) are included for reference. 50 mV/s.

given potential than the physical mixture. For the physical mixes the sample with 75 mol% IrO_2 had a lower rate of OER than the sample shown in Figure 10.6. On the other hand the sample with 25 mol% IrO_2 had the same rate for the OER as the sample with 50 mol% IrO_2 for all but the highest potentials, where the rate was higher. The situation was not as clear for the chemically mixed oxides, with all the mixed oxides giving approximately the same rate for the OER. However, the largest increase in the rate for the OER occured between the pure iridium oxide sample and the samples, both chemically and physically mixed, with 25 mol % RuO_2, see Figure 10.7. The potential for the start of the OER followed the same trend as that for the rate of OER. The starting potential was lowest for pure RuO_2 and highest for pure IrO_2.

A fairly linear region in the current-potential curve can be seen in the current range of $1 \cdot 10^{-5}$ A/cm^2 to $5 \cdot 10^{-2}$ A/cm^2 in Figure 10.6. A slope of 30–40 mV/dec was observed for all the samples, including the chemical and physical mixed samples with compositions other than equal amounts of iridium and ruthenium (not shown). This is in contrast to the increase from 40 mV/dec for pure RuO_2 to almost 60 mV/dec for samples with iridium content above 50 % observed by Kötz and Stucki [252] on sputtered films and on thermally prepared oxides by Angelinetta and co-workers [178]. A gradual transition from 40 mV/dec for RuO_2 to 60 mV/dec for samples of IrO_2 was also seen for thermally prepared electrodes [178].

The experimental and calculated potentials for the OER at 0.1 mA/cm^2 is shown

in Figure 10.7 in the same manner as presented by Kötz and Stucki [252]. The calculated overpotential, η, was found from:

$$i_{\mathrm{tot}} = \mathrm{x} \cdot i_{0,\mathrm{Ru}} \cdot 10^{\eta/b_{\mathrm{Ru}}} + (1-\mathrm{x}) i_{0,\mathrm{Ir}} \cdot 10^{\eta/b_{\mathrm{Ir}}} = 0.1 \text{ mA/cm}^2 \tag{10.1}$$

were x gives the ruthenium content ($\mathrm{Ru_xIr_{1\text{-}x}O_2}$), $i_{0,\mathrm{Ru}} = 10^{-8}$ mA/cm^2 is the exchange current density for $\mathrm{RuO_2}$ and $i_{0,\mathrm{Ir}} = 10^{-9}$ mA/cm^2 is for $\mathrm{IrO_2}$. The Tafel slope for $\mathrm{RuO_2}$ is $b_{\mathrm{Ru}} = 32$ mV/dec and $b_{\mathrm{Ir}} = 38$ mV/dec is for $\mathrm{IrO_2}$. The Tafel slopes are the measured slopes from the experiments shown here. The potential for the OER at 0.1 mA/cm^2 was found from: $E_{\mathrm{OER}} = 1.23 \text{ V} + \eta$. The physically mixed oxides have a potential for the OER close to that of the calculated value, whilst the chemically mixed oxides have a higher potential.

Comparing Figure 10.7 with the corresponding figure in Kötz and Stucki [252] it can be seen that Kötz and Stucki [252] observed a potential variation different from that expected assuming a linear combination of the properties of $\mathrm{IrO_2}$ and $\mathrm{RuO_2}$. The same trend was observed by Marshall and Haverkamp [160] for iridium-ruthenium oxide on antimony doped tin oxide particles, and by Cheng *et al.* [255] for iridium-ruthenium oxide powders. These results are in contrast to the small changes in potential observed in this work. No explanation for this deviation is known.

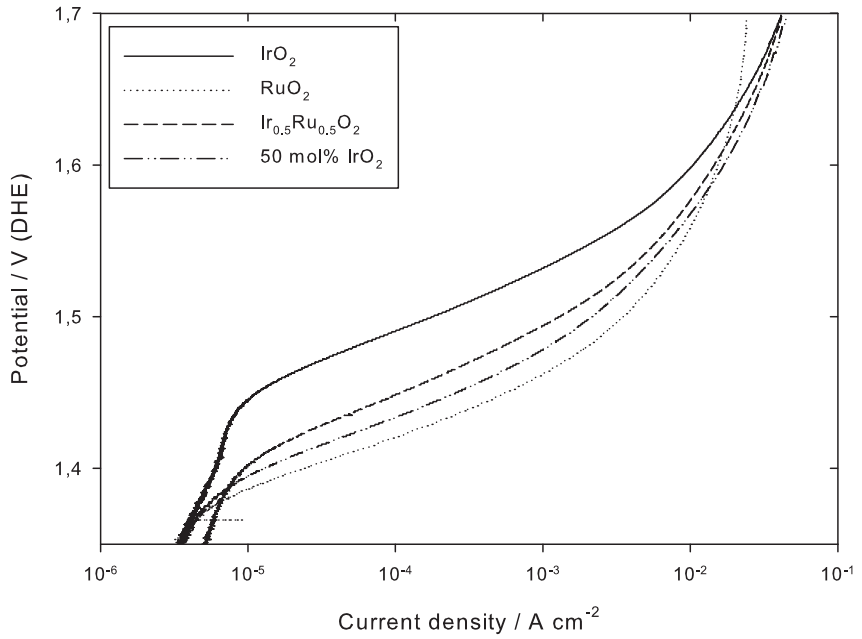

Figure 10.6: Polarisation curves of the chemical and physical mixtures of equal amounts of iridium oxide and ruthenium oxide. The polarisation curves of pure $\mathrm{IrO_2}$ (—) and $\mathrm{RuO_2}$ ($\cdots$) are included for reference.

XRD analysis of the chemically mixed oxides show that an inhomogeneous system was likely formed. For the heat treatment study of $\mathrm{Ir_{0.5}Ru_{0.5}O_2}$ it would appear that a two phase system was formed. As the crystal structure of one of the phases

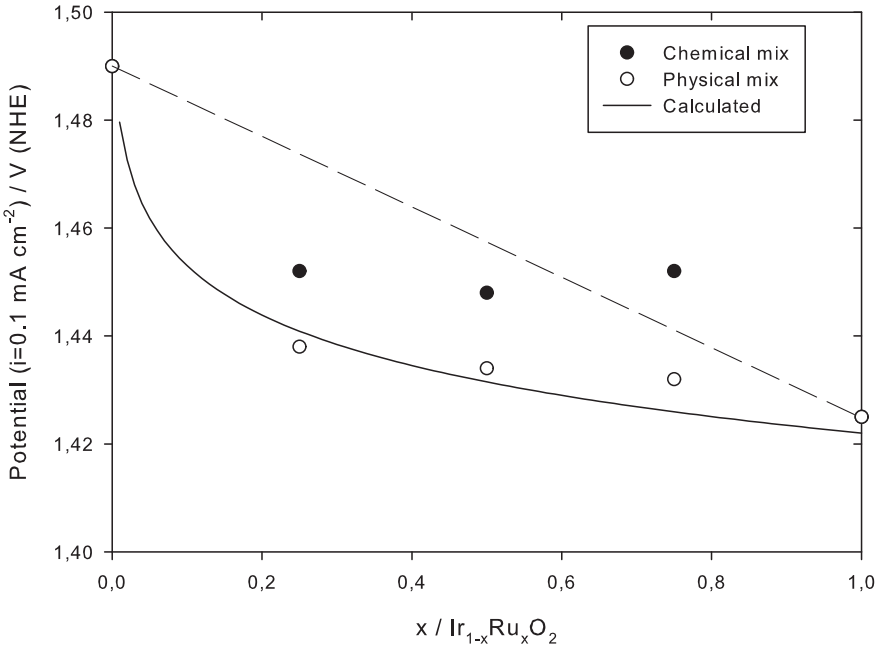

Figure 10.7: The potential for the OER at 0.1 mA/cm^2. (—) The calculated potential, assuming a linear combination of the properties of IrO_2 and RuO_2, see the text for details. (- - -) is just a straight line.

moved closer to that of pure iridium oxide with increasing heat treatment temperature, ruthenium must be lost from this phase. However, no separate ruthenium oxide phase was observed. Several scenarios can be envisioned: Ruthenium can diffuse out of the iridium oxide like phase and form separate small ruthenium oxide crystallites, ruthenium can diffuse to the surface and form a thin ruthenium oxide layer or ruthenium can enter the other phase giving a mixed iridium-ruthenium oxide phase. No separate ruthenium oxide phase would be visible for any of these scenarios (assuming that the pure ruthenium oxide crystals or layers are small enough).

The voltammetry does not either clarify the situation. As the chemically and physically mixed oxides, with the same composition, were similar it would seem that an iridium rich and a ruthenium rich phase was formed. The anodic peak at 1.2–1.3 V in the chemical mixtures of $Ir_{0.5}Ru_{0.5}O_2$ and $Ir_{0.25}Ru_{0.75}O_2$, that is not seen in the pure oxides nor the physical mixtures, suggest the formation of some sort of a mixed oxide phase. This is in accordance with the data from the heat treatment study of $Ir_{0.5}Ru_{0.5}O_2$ as the catalysts shown in the CVs was heat treated at 600 °C. A quite pure iridium oxide phase can therefore be expected to be present, together with a more mixed phase.

The polarisation measurements, see Figure 10.6 and Figure 10.7, show that there was a difference between the chemically and the physically mixed oxides. The straight line trend observed by others [160, 252, 255] was not found for the chemically mixed oxides in this work. However, it is hard to conclude if homogeneous chemically mixed oxides were formed or not on this basis. What is clear is that the

presence or not of ruthenium in the sample is the main factor determining both the starting potential and the rate of the OER, both in the physical and the chemical mixed samples.

In the CVs the ruthenium oxide signal seemed to be less dominant than the iridium oxide signal, both for the physically and the chemically mixed oxides. The same was true for the polarisation measurements, see Figure 10.7. A smaller active surface area, for example because of larger particle sizes, for ruthenium rich samples could explain the dominance of the iridium oxide signal. Surface enrichment of iridium can be an explanation for the strong iridium signal in the polarisation measurements as only the surface is involved. For the CVs the bulk is also involved. Surface enrichment of iridium has been observed before on thermally prepared iridium-ruthenium oxides [177, 178], thermally prepared iridium-ruthenium-titanium oxides [192] and for iridium-ruthenium oxides prepared by the Adams fusion method [156]. The results shown here also fit with the DFT calculations by Man [175] as they indicate that a surface enrichment of iridium is likely for the chemically mixed oxide samples with oxygen species adsorbed on the surface. A final point is that the DFT calculations [175] show that iridium preferentially segregates to the active sites for the OER on the (110) surface. Polarisation measurements on a chemically mixed iridium-ruthenium oxide catalysts are therefore expected to show iridium oxide behaviour even for quite small iridium contents. Although this is not observed in Figure 10.7, nor in Figure 10.6, it can be seen that the potential is higher for the chemically mixed samples. This might be the result of a increased number of iridium atoms in the active sites for the OER.

As discussed above the main anodic peak of iridium oxide, at just under 1 V, would be expected to change with the addition of ruthenium to the oxide if a true solid solution was formed. Comparing the CVs of the chemical mixtures seen in Figure 10.3 it is evident that the peak potential does not shift from that of pure iridium oxide for $Ir_{0.75}Ru_{0.25}O_2$ and $Ir_{0.5}Ru_{0.5}O_2$. Only for $Ir_{0.25}Ru_{0.75}O_2$ a small shift in the anodic direction can be detected. This is in contrast to the shift of over 100 mV seen by Kötz and Stucki [252] for sputtered iridium-ruthenium oxide films. This is further confirmation that homogeneous chemical mixtures of the oxides were not formed.

10.5 Conclusions

Iridium-ruthenium oxide catalysts were prepared by the hydrolysis method. Both X-ray diffraction and electrochemical measurements indicate that homogeneous chemically mixed iridium-ruthenium oxides were not prepared. Instead multi phase systems were formed. These were likely two phase systems with a nearly pure iridium oxide phase and a mixed phase.

The rate of the oxygen evolution reaction appeared only to be dependent on the amount of ruthenium for the samples prepared in this work. The presence of ruthenium, even 25 mol%, gave a faster OER both for the chemical and the physical mixtures.

Chapter 11

Electrochemical behaviour of iridium oxide films in trifluoromethanesulfonic acid

Lars-Erik Owe, Ingrid Anne Lervik, Mikhail Tsypkin, Marie Varden, Svein Sunde

This article is published in The Journal of the Electrochemical Society [2]. *The layout of the article has been changed to improve readability, however the text and figures have not been changed.*

11.1 Abstract

Anodically formed iridium oxide film (AIROF) in trifluoromethanesulfonic acid (TFMSA) was used as a model system to examine the possible influence of Nafion™ on the electrochemical properties of iridium oxide catalysts for the oxygen-evolution reaction (OER) in PEM water electrolysis. A series of observations were made that are consistent with a significantly higher degree of adsorption of sulphate than triflate at the oxide surface. In TFMSA the reaction rates for the OER are significantly higher than in H_2SO_4, and the flatband potential in TFMSA is higher than in sulphuric acid. In solutions of $Fe(CN)_6^{3-/4-}$ and sulphuric acid the reduction currents associated with the redox couple were much smaller than the oxidation currents. The same cathodic "blocking" was observed in TFMSA and $Fe(CN)_6^{3-/4-}$. However, in the presence of small amounts of chloride ions (10 ppm) in TFMSA the AIROF electrode showed no such cathodic "blocking" of the faradaic current and the electrode behaves similarly to a metal electrode. Chloride ions do not affect the redox behaviour with sulphuric acid as the electrolyte. The absence of cathodic "blocking" in TFMSA with chloride ions is also suggested to be due to the lesser degree of electrolyte adsorption than in sulphuric acid, the oxide and substrate being more open to chloride hindering reoxidation of oxide cracks.

11.2 Introduction

Water electrolysis with polymer electrolyte membranes (PEM) relies on proton-conducting membranes such as Nafion™ and, at the anode, oxide electrocatalysts such as iridium oxide. Nafion™ consists of a perfluorocarbon matrix with randomly clusters of superacidic trifluoromethanesulfonic (triflic) groups. While the combination of Nafion™ and iridium-based oxides appears to give reasonably good performance [146], Fukuda *et al.* [260] found that addition of F^- reduces the rate of oxygen evolution on dimensionally stable anodes (DSA-type) of Ti/RuO_2, Ti/IrO_2 and Ti/RuO_2–TiO_2 electrodes. The activity reduction comes about by the inactivation of sites for oxygen evolution or the exchange of hydroxyl groups by adsorbed F^-. Fluoride adsorption was also found on TiO_2 [261–263]. One may therefore consider the possible adsorption of fluoride moieties from the Nafion™ membrane a relevant possibility, with adverse effects on the oxygen-evolution reaction (OER). Also, this addresses the common practice of characterisation of the electrocatalysts in sulphuric acid at a pH corresponding to that in the membrane. While investigations aimed at the assemsment of the influence of the membrane material have been performed for PEM fuel cells [264, 265], no such results appear to be available for the anode reaction in PEM water electrolysis.

The oxide electrocatalysts for PEM OER studied in our group so far are powders consisting crystallites in the order of 15 through 20 nm size produced by the hydrolysis or the polyol method [82, 143–145]. While this gives a large surface area, the application of these catalysts to solid electrodes becomes impractical without the use of a binder such as Nafion™. To be able to make the comparison of the system with and without the presence of Nafion™-like entities, anodically formed iridium oxide films (AIROF) [34, 35, 42–44, 105, 108–110, 115, 117, 120, 123, 126, 129, 132, 140, 187] appears to be an appealing model system. Not only does the AIROF appear to behave more or less identically to both DSA and oxide powders in terms of the OER [44, 187], but it also displays a metal-to-semiconductor transition absent in the powders [44, 188]. This is useful, since adsorption processes may have easily recognisable consequences at a semiconductor electrode, for example through the value of the flatband potential. Also, faradaic reactions are significantly influenced by the type of adsorbate and its coverage. For example, Gottesfeld [140] reported that for the $Fe(CN)_6^{3-/4-}$ redox couple in alkaline solutions the electrode showed metallic behaviour in both the oxidised and reduced states, as did an unoxidised Ir electrode. In acidic medium, however, a "blocking" of the cathodic current appears due to misalignment of the energy bands in the AIROF and the energy levels in solution caused by the hydroxyl ions adsorbed at the oxide surface at high pH being replaced by protons at low pH.

As the experiments implied by the considerations above would involve transfer of the oxide between different solutions, relevant studies is that of Birss *et al.* [105], Bock and Birss [120] and Lee *et al.* [126] that show that the AIROF electrode can crack and possibly expose Ir metal to the electrolyte upon such transfer and also during potential cycling. These results are somewhat difficult to reconcile with the semiconducting behaviour observed by Gottesfeld [140] and also by ourselves [44]; one would expect an electrode with significant amounts of metallic Ir exposed to

the electrolyte to display significant cathodic currents also at low pH. This is less of a problem to understand if the exposed iridium metal is quickly repassivated. However, also in this case would one expect the adsorption of solvent entities to influence on the process. A simple experiment, pursued here, to address these issues is to add chloride ions to the electrolyte as it is known that chloride hinders the growth of iridium oxide on iridium metal [115]. Strong adsorption of electrolyte moieties would thus be expected to hinder chloride access favouring growth, and vice versa.

It is the purpose of the present paper to address the issue of electrolyte adsorption at iridium oxide and its influence on the electrochemical properties of the oxide. In addition to modelling the anode electrocatalyst of the PEM water electrolysis system by AIROF, trifluormethanesulfonic acid (TFMSA) is used as a model for the Nafion™ membrane. We will use sulphuric acid as the reference system. This seems in place as sulphuric acid is a common choice as the electrolyte in examinations of electrocatalysts for the oxygen evolution reaction (OER). In the following we will show, somewhat contrary to our expectations, that a significantly higher degree of adsorption is to be expected in sulphuric acid, and that the experiments in this electrolyte significantly underestimates the true catalytic activity of iridium oxide. This will be shown to be consistent with a series of other findings such as variations in flatband potential and repassivation in the absence and presence of chloride in the electrolyte.

11.3 Experimental

11.3.1 Materials and Chemicals

Wire of Ir (purity 99.8 %) from Alfa Aesar was mounted in a non-conducting sheath of Tefzel from Dupont. Foil of Ir (purity 99.5 %) from Sigma-Aldrich was used for impedance and OER measurements. HCl (37 %), H_2SO_4 (95–97 %), $K_3[Fe(CN)_6]$ (> 99 %), $K_4[Fe(CN)_6] \cdot 3\,H_2O$ (> 99 %), KCl (> 99.0 %), KOH (p.a.) and Agar was obtained from Merck KgaA. The TFMSA (98+ %) was obtained from Alfa Aesar and Merck. All solutions were prepared from deionised water and stored in glass containers. Chloride was added as concentrated HCl (p.a., Merck KgaA).

11.3.2 AIROF electrode preparation

Prior to every measurement the Ir wire was mechanically polished to a mirror finish. The Ir wire and the resin sheath were boiled in 10 wt.% HCl and four changes of deionised water. The foil was prepared by the same method.

In order to grow a layer of iridium oxide the electrodes were put in a solution of 0.5 M H_2SO_4, or alternatively TFMSA with a pH of 0.4, and cycled as described in [42], briefly the electrode was cycled between 0 and 1.5 V at 150 mV/s. The oxide layers on the rotating disc- and the iridium foil-electrodes were grown by cycling 250 and 500 times respectively.

11.3.3 Electrochemical measurements

The oxide growth and cyclic voltammetry measurements on the iridium rotating disc electrode (RDE) were made with a PAR Model 273A potentiostat or a Gamry Instruments Series G 300 potensiostat. Measurements were carried out using a standard three-electrode setup; iridium metal/oxide RDE as working electrode with a geometric area of 0.00785 cm^2, Pt counter electrode and a dynamic hydrogen reference electrode (DHE) in a separate compartment connected with a glass fritt or a Radiometer Analytical Model REF321 general purpose Ag/AgCl reference placed in an external compartment of saturated KCl solution connected to the electrolyte by a salt bridge (agar and saturated KCl solution) with a Luggin capillary tip. The DHE was placed in the base electrolyte, i.e the electrolyte without the $Fe(CN)_6^{3-}/Fe(CN)_6^{4-}$ redox couple and chloride ions.

The RDE measurements were made with a Modulated Speed Rotator from Pine Research Instrumentation and a Computer Controlled Bipotentiostat from Pine Research Instrumentation or a Gamry Instruments Series G 300 potensiostat. All other details were as reported above.

Impedance measurements and oxygen evolution measurements were made with a Voltalab PGZ 301 potentiostat from Radiometer Analytical. Measurements were carried out using a standard three-electrode setup; iridium foil as working electrode with a geometric area of 1.94 or 3.9 cm^2, Pt counter electrode and either a DHE or a Radiometer Analytical Model REF321 general purpose Ag/AgCl reference placed in a Luggin capillary.

All solutions were argon purged. All measurements were carried out at room temperature, 23–24 °C. All potentials are given against the dynamic hydrogen reference electrode (DHE) unless otherwise stated.

A Hitachi S-3400N SEM (scanning electron microscope) was used for the SEM investigations. A working distance of 15 mm with an acceleration voltage of 15 kV was used. The instrument was operated in the high vacuum mode. The electrode was not coated before imaging. An Oxford Instruments EDS (energy dispersive spectroscopy) system was used for composition detection.

11.4 Results and discussion

A SEM image of the AIROF electrode (after 500 growth cycles in sulphuric acid) is shown in Fig. 11.1. The electrode was dried in air at room temperature (three days or several weeks, no difference was observed between the two) before SEM imaging. Some charging was observed during the experiment. EDS results show iridium and oxygen present in all tested areas. The film does not appear to have quite the same cracked structure as seen by others [105, 117, 126], but rather the smother surface observed by Mozota and Conway [115].

Fig. 11.2 shows cyclic voltammograms of the oxide film on the iridium RDE in H_2SO_4 and TFMSA. As a comparison a CV recorded in TFMSA of a film that was also grown in TFMSA is shown. The anodic peaks between 0.7 V and 1.1 V are related to intercalation of electrolyte ions in the oxide. The spectrum and peak

positions of the results from H_2SO_4 are in good agreement with results found by other authors [42, 43, 109, 110, 123]. The CVs of the films that were not transferred to a new electrolyte before recording of the CVs were in essence similar. Besides the lower charge of the film grown in TFMSA the anodic prepeak is less pronounced. The anodic prepeak is known to be more or less visible depending on the electrolyte [108]. This can explain the change in the anodic prepeaks seen in the CVs, shown in Fig. 11.2. As the reaction giving rise to the main anodic peak involves solution anions [35] a shift of the main peak potential with different anions is not unreasonable.

The oxide growth was slightly slower in TFMSA solutions than in sulphuric acid solutions. Typically 300–350 growth cycles where required in TFMSA to get the same charge as 250 cycles in sulphuric acid.

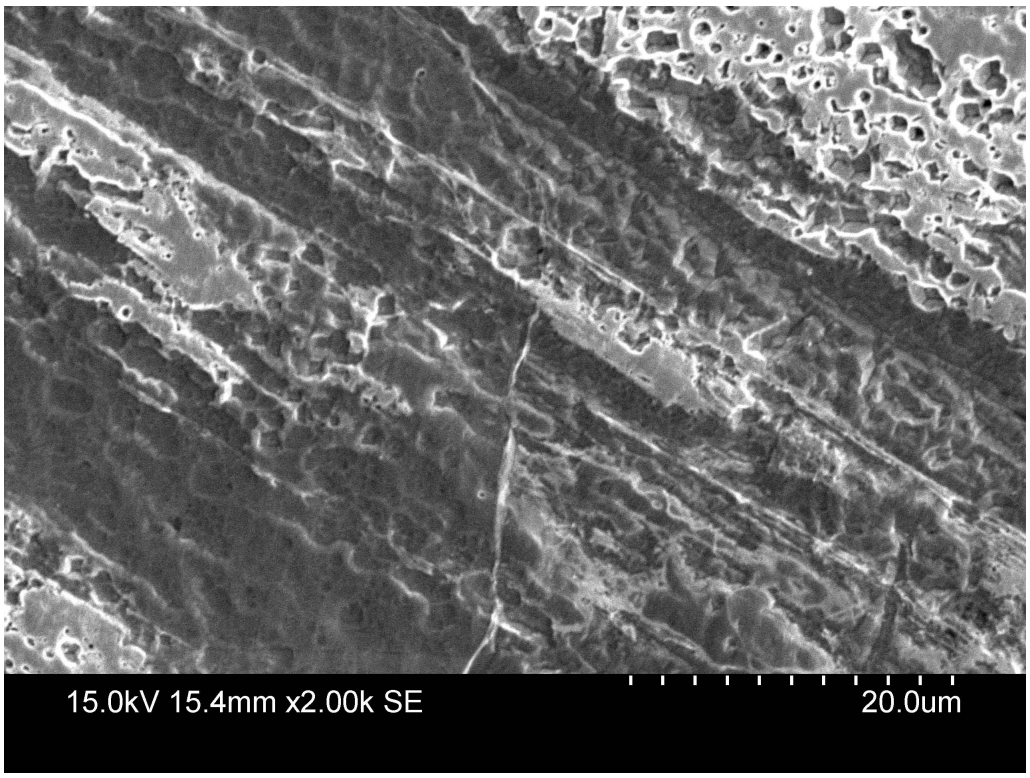

Figure 11.1: SEM image of AIROF after 500 growth cycles in H_2SO_4.

Fig. 11.3 shows the oxygen evolution reaction on AIROF in H_2SO_4 and TFMSA, both at pH 0.4. The potential was swept from 1.0 V to 1.7 V at a sweep rate of 5 mV/min. The figure indicates no significant differences in the two solutions in terms of (Tafel) slope, but the potential remains lower for the oxide in TFMSA than in H_2SO_4 for the entire current range, indicative of a higher catalytic activity in this solution.

Impedance measurements of the AIROF electrode were performed both directly after making the film, without removing it from the H_2SO_4 or TFMSA solution, and after transferring the film to a different solution.

The impedance measurements were conducted at 1.0 V, with an amplitude of 5 mV and with frequencies between 100 kHz and 10 mHz. After the first impedance

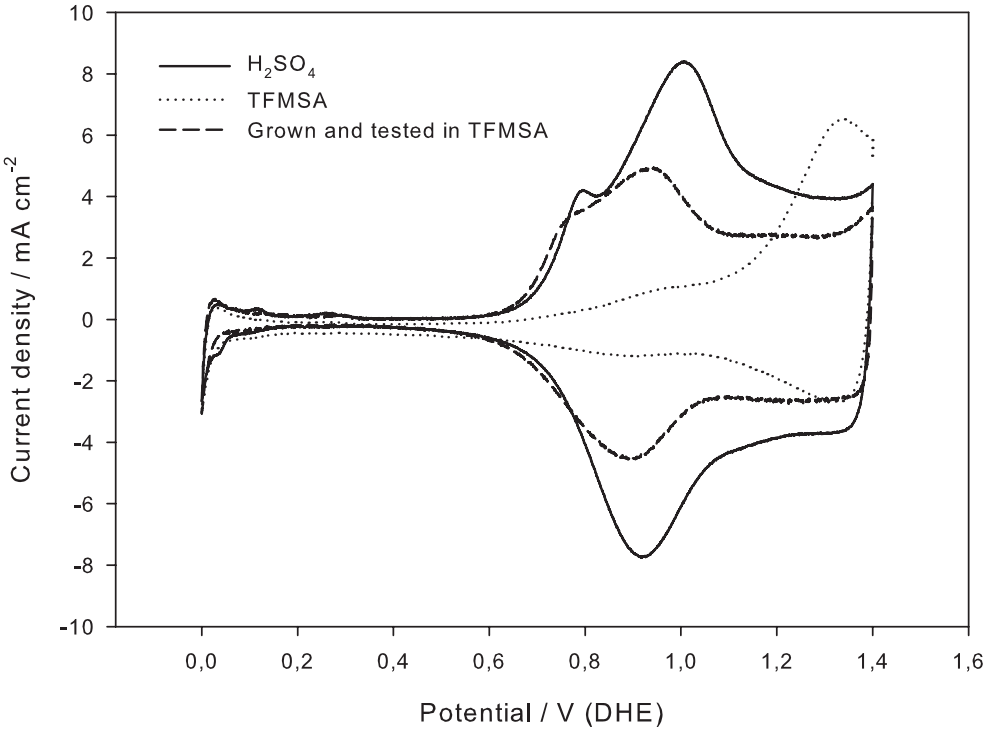

Figure 11.2: Cyclic voltammogram of AIROF in H_2SO_4 (pH=0.4), AIROF grown in H_2SO_4 then transferred to TFMSA (pH=0.4) and AIROF grown and tested in TFMSA (pH=0.4), sweep rate 100 mV s^{-1}.

measurement a CV (0–1.4 V, 100 mV/s) was recorded and a new impedance measurement was conducted, then 9 CVs were recorded before a new impedance measurement and finally 40 CVs before a last impedance measurement.

Figure 11.4 shows the impedance measurements for an electrode that was not removed from the sulphuric acid solution before the impedance measurement. The experiment where the AIROF electrode was prepared in TFMSA, removed and rinsed with distilled water and transferred to a solution of TFMSA with 10 ppm Cl^- (not shown) gave qualitatively similar results. Figure 11.5 shows the results for an electrode that was removed from the H_2SO_4 solution, rinsed with distilled water and placed in a TFMSA solution. The presence or absence of Cl^- did not significantly change the impedance results. Table 11.1 shows the frequency, ω_D, where the plot makes a sharp bend upwards to a near vertical line (see Figure 11.4 where this point is indicated). Experiments where also carried out on an Ir metal electrode in the same solutions (the Ir electrode was treated the same way as it would be before growth of an AIROF layer).

The frequency, ω_D, shown in Table 11.1 is related to the diffusion length, L, by $\omega_D \propto {}^D/_{L^2}$ [188]. A reasonable assumption would be that the diffusion constant, D, is the same for all experiments. As ω_D changes only to a small degree for the experiments in sulphuric acid and TFMSA without transfer the diffusion length

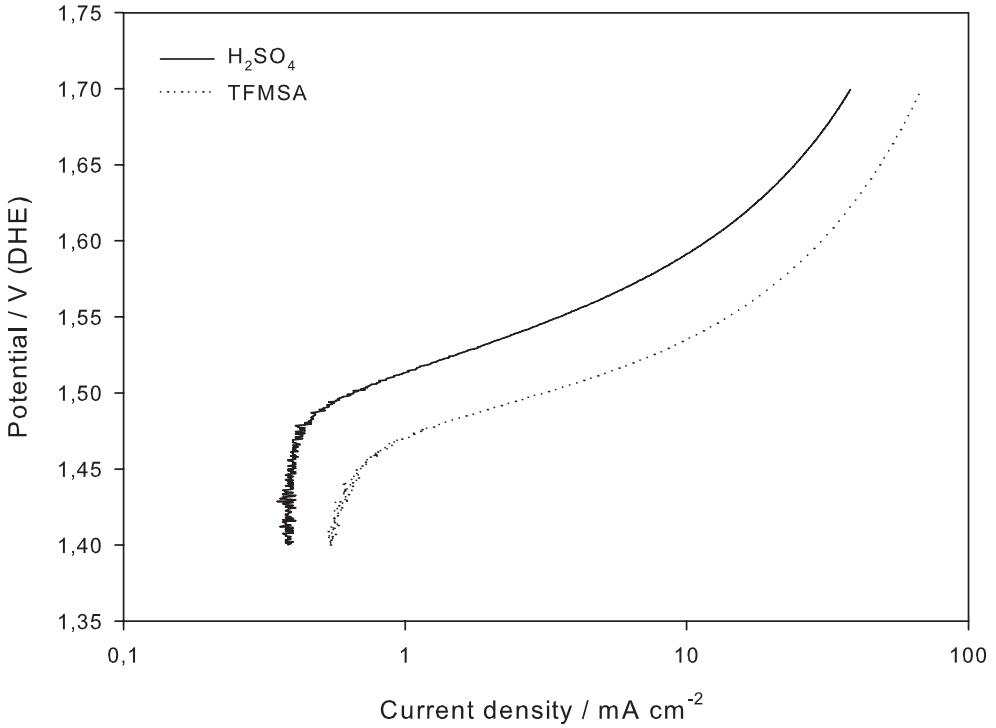

Figure 11.3: OER on AIROF in TFMSA (Cl^- free) and H_2SO_4 (pH 0.4). The electrode was swept from 1.0 V to 1.7 V vs DHE at a sweep rate of 5 mV/min.

does not change significantly during the experiments. The same behaviour was observed by Bock and Birss [120]. However in the experiment where the electrode was transferred from H_2SO_4 to a TFMSA solution a significant change is evident indicating that the diffusion length is changing. As the frequency ω_D is higher in TFMSA this once again confirms that the oxide film is thinner when it is made in TFMSA solutions (the same number of cycles were used to make the oxide film for all the impedance measurements). Finally, the frequency ω_D is increasing upon transfer from sulphuric acid to TFMSA (Table 11.1) indicating that the effective diffusion length is decreasing.

The impedance measurements on iridium metal (not shown) showed a clear development of the impedance response with cycling. The difference is assumed to be caused by the growth of the iridium oxide layer on the electrode. Similar trends were observed in all the tested electrolytes, sulphuric acid and TFMSA, both with and without chloride ions present.

Fig. 11.6 shows current-potential curves for $Fe(CN)_6^{3-}$ /$Fe(CN)_6^{4-}$ obtained on the AIROF RDE in TFMSA (pH 0.4). Directly after transferring the electrode to the electrolyte the film shows symmetrical non-blocking behaviour, similar to the case with 10 ppm Cl^- in the figure. In the absence of chloride ions the faradaic reduction current gradually changed to a limited or blocked value independent of the rotational rate, ω, as seen in the inset in the figure. The change from non-

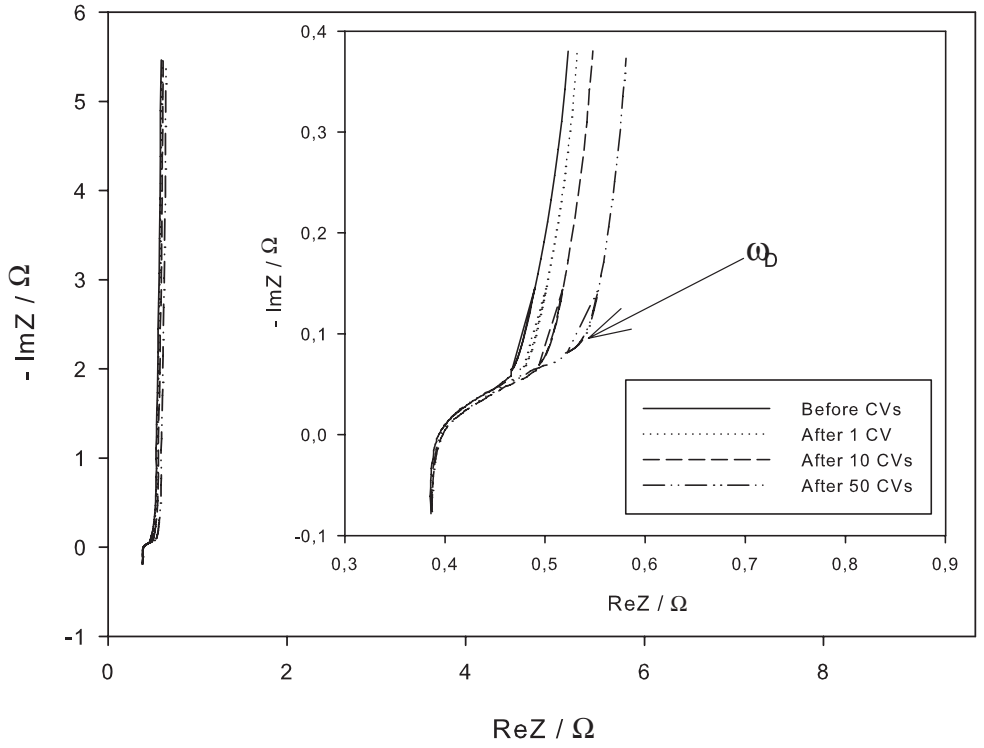

Figure 11.4: Nyquist diagram for an AIROF electrode in 0.5 M H_2SO_4. ω_D is the frequency where the plot makes a sharp upwards bend.

Table 11.1: The frequency, ω_D, where the impedance diagram makes a sharp upwards bend

# of CVs	H_2SO_4	H_2SO_4 - TFMSA	TFMSA
0	18 Hz	140 Hz	250 Hz
1	18 Hz	89 Hz	223 Hz
10	20 Hz	–	200 Hz
50	18 Hz	–	200 Hz

blocking to blocking behaviour can also be seen in the CVs of Fig. 11.7. For linear potential sweeps this change was completed in the course of about 10 sweeps from 1.2 V to 0 V.

In the presence of chloride ions ($\geq$ 10 ppm) the redox couple never exhibited a blocked faradaic reduction current even after 60 cyclic voltammograms between 0 V to 1.2 V. On the contrary, the current response was similar to one in alkaline solution (see [44]), where the anodic and cathodic limiting currents are proportional to the concentration of the redox species and $\omega^{1/2}$. The same results were obtained if the AIROF electrode was prepared in TFMSA (not shown).

Current-potential curves similar to those shown in Figure 11.6 were performed in 0.5 M H_2SO_4 and 0.1 M KOH both with 0.1 M $Fe(CN)_6^{3-}$ and $Fe(CN)_6^{4-}$. In the

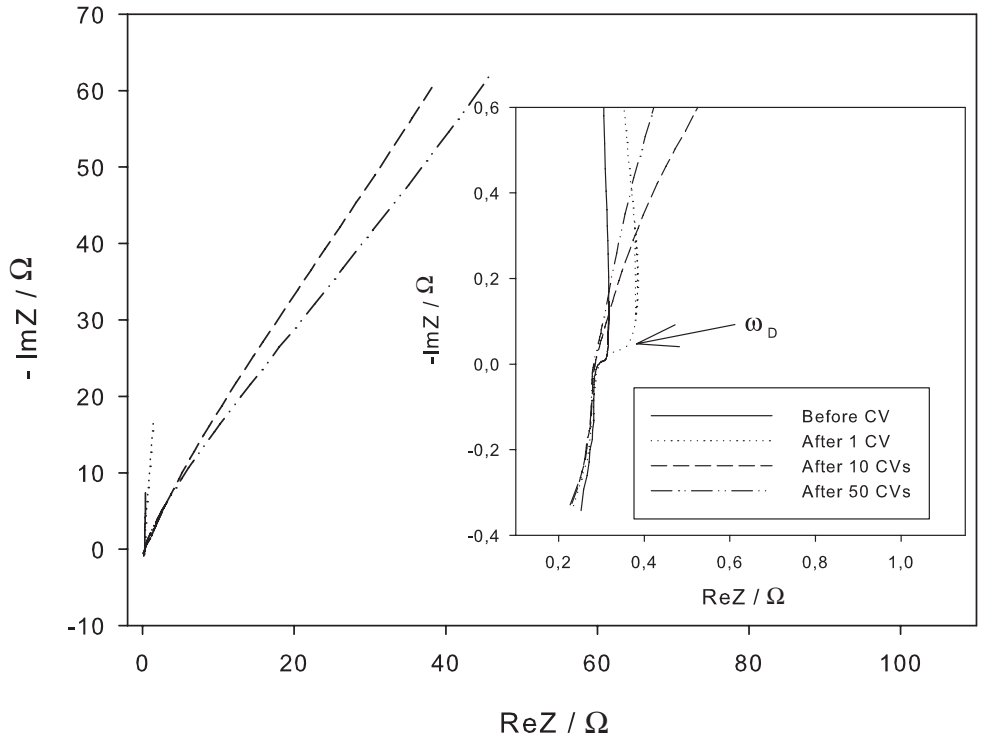

Figure 11.5: Nyquist diagram for an AIROF electrode manufactured in 0.5 M H_2SO_4 and moved to TFMSA (pH=0.4).

sulphuric acid solution, both with and without chloride ions, results similar to the ones in chloride free TFMSA were obtained. In the alkaline solution non-blocking behaviour, similar to what was measured in TFMSA with chloride ions present, was always obtained regardless of the presence or absence of chloride ions. Conducting measurements in the pH range between that of 0.5 M H_2SO_4 and 0.1 M KOH gave a gradual decline in the absolute value of the reduction current from that found in 0.1 M KOH to that found in 0.5 M H_2SO_4. The results are reported and discussed further elsewhere [44].

An example of plots of the inverse current density vs. one over the square root of the angular velocity, ω, are shown for selected potentials in Fig. 11.8. Corresponding plots were similar for the other electrolytes (not shown). The kinetic currents obtained by extrapolation of the current in Fig. 11.8 to infinite rotational velocity ($\omega \to \infty$) are given as Tafel plots in Fig. 11.9 both for hexacyanoferrate solutions with sulphuric acid and TFMSA (with and without Cl^-) as the supporting electrolyte. (The "blocking" behaviour for cathodic currents in sulphuric acid and chloride free TFMSA, Fig. 11.6, obviously prevents the cathodic branch to be presented in these solutions.)

From Fig. 11.9 clear and discernible Tafel-behaviour is present in most cases (although the linear region only spans 1–2 decades). For the oxidation reaction it is apparent that the fastest reaction is in TFMSA with 10 ppm Cl^-, followed by

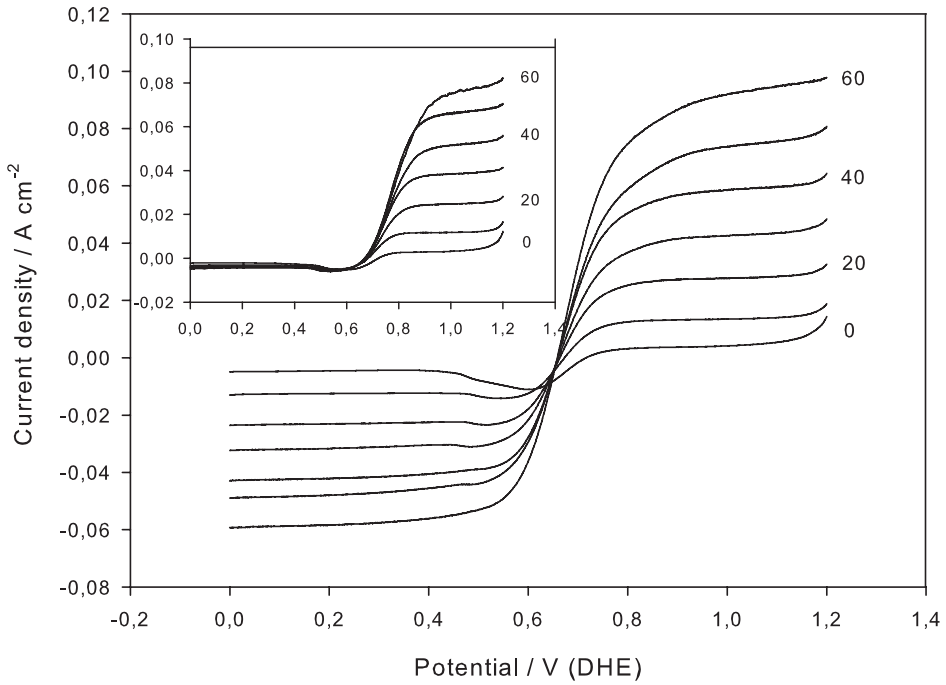

Figure 11.6: Current-potential curves obtained on the AIROF RDE with 0.1 M $Fe(CN)_6^{3-}$ and $Fe(CN)_6^{4-}$ in TFMSA (pH 0.4) with 10 ppm Cl^-. The inserted graph shows the case without chloride ions. Scan rate -5 mV/s. The square root of the rotational angular velocity ω is given in $(\text{rpm})^{1/2}$.

the reaction in TFMSA without Cl^- and finally the reaction in H_2SO_4 (assuming a one-electron reaction, symmetry factors of approximately 0.5 results both in sulphuric acid and in TFMSA). In TFMSA with Cl^- present a rate constant slightly in excess of $10^{-3}\,\text{cm}\,\text{s}^{-1}$ can be estimated, in reasonable agreement with rate constants reported for the same reaction at Pt [266–271].

In view of the known attraction of the oxide to fluoride anions [261, 262] we conducted another set of impedance measurements in order to extract the surface band edge positions as a function of electrolyte composition. The effect of the applied potential on the capacitance of the AIROF in H_2SO_4 at pH 0.4 is shown in Fig. 11.10 as a Mott-Schottky plot for various frequencies. The measured capacitance makes a reasonably straight line in parts of the C^{-2} vs. E plot. The results obtained are in good agreement with previously published data [141]. The line has a negative slope, indicating a p-type semiconductor as expected [141]. The flatband potential, V_{fb}, of AIROF in H_2SO_4 at a concentration corresponding to pH 0.4, as obtained from the intercept of the straight line with the potential axis, is estimated to be approximately 750 mV.

For verification of the method used, the capacitance of TiO_2 and AIROF in various pH's was also measured and is compared to AIROF in Fig. 11.11. The band edges at the solid-solution interface decrease at 59 mV/pH [272, 273] for ideal surfaces at room temperature relative to the energy level assigned to a reference

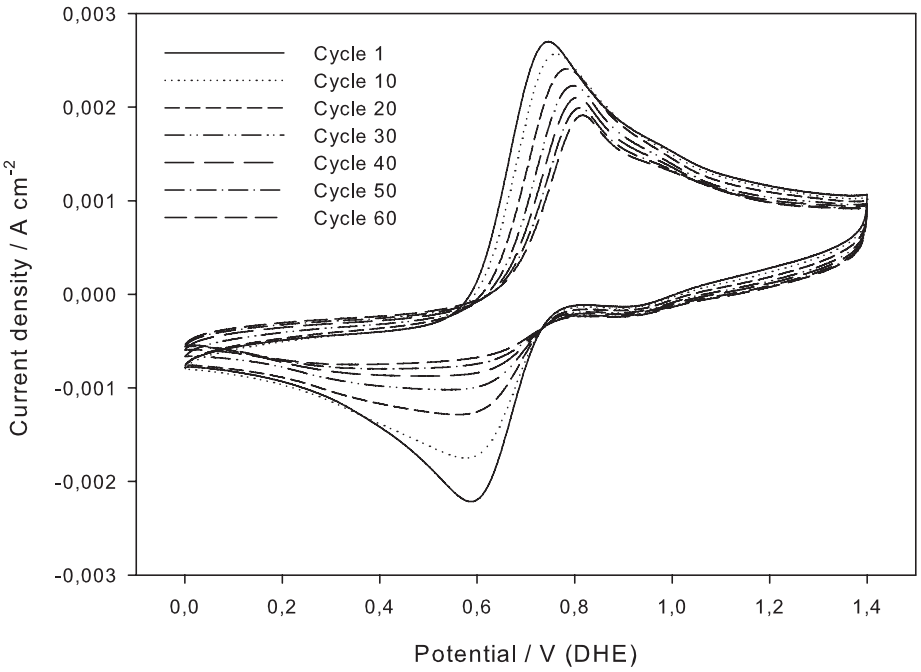

Figure 11.7: CVs obtained on the AIROF RDE with 0.1 M $Fe(CN)_6^{3-}$ and $Fe(CN)_6^{4-}$ in TFMSA (pH 0.4) without Cl^-. Scan rate 200 mV/s. The scan number is indicated in the legend.

electrode (i. e. the solution). Morrison [274, p. 88] reports that the flatband potential (i.e. the potential at which there is no space charge in the solid and therefore a measure of the band-edge positions at the surface) follow this rule in most cases for nondegenerate semiconductors. The AIROF electrode shows a slope of −75 mV/pH. Such deviations from the theoretical value are to be expected if the activity of protons in the surface is concentration dependent, though [91].

The effect of the applied potential on the capacitance of the AIROF in TFMSA pH 0.4 is shown in Fig. 11.12, again displayed as a Mott-Schottky plot. The flatband potential of AIROF in TFMSA (pH 0.4) was measured several times, both in solutions with Cl^- and without, and the mean potential was found to be 790 mV, regardless of the presence or absence of chloride ions. The presence or absence of chloride ions does therefore not appear to influence the flatband potential in TFMSA solutions.

To check for possible chemical reactions between the $Fe(CN)_6^{3-/4-}$ redox couple and TFMSA, the reactions of the redox couple obtained on a Pt electrode was studied both in sulphuric acid and TFMSA (solutions with and without 10 ppm Cl^-) by cyclic voltammetry, Fig. 11.13. The peaks of the voltammograms in Fig. 11.13 coincide. This shows that there is no alternative chemical reaction taking place between TFMSA and the redox couple in the solution. Also note the suppression of the currents in the hydrogen adsorption region and the platinum oxide region, indicative of adsorption of (Fe,CN) species at the electrode surface [275]. This is

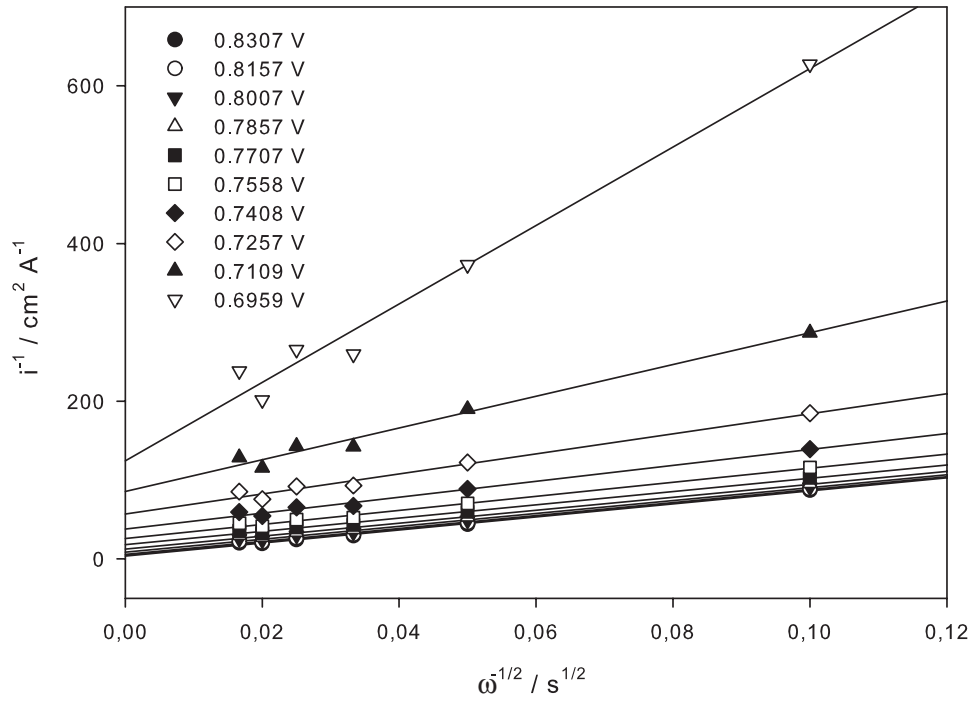

Figure 11.8: Inverse current density vs. $\omega^{-1/2}$. Potentials for a subset of the measurements are indicated in the legend. Data from the anodic part of the inserted graph in Fig. 11.6.

further supported by the fact that it was necessary to clean the Pt-electrode frequently during the experiments to remove species, that hindered the electrochemical reactions, adsorbed on the electrode.

In solutions with only $Fe(CN)_6^{4-}$ the anodic current was comparable to the anodic current with both of the redox species, whilst the cathodic current was close to zero. In solutions with only $Fe(CN)_6^{3-}$ the corresponding situation was true; cathodic current was close to the current with both of the redox species and the anodic current was close to zero. This was observed both for H_2SO_4 and TFMSA (with and without chloride) as the base electrolyte.

To check the stability with time of the AIROF electrolyte system potentiostatic measurements where conducted (not shown). The AIROF electrode was polarised at 1.4 V for 1 hour with $\omega = 1600$ rpm. The experiment was performed in TFMSA and H_2SO_4, both with and without 10 ppm Cl^- both in the presence and without the redox couple. In the electrolyte without the redox couple the current was stable, after an initial drop, in the time frame of the experiment. In the experiment conducted in the presence of the $Fe(CN)_6^{3-}/Fe(CN)_6^{4-}$ redox couple the current in TFMSA was found to decrease with time (approximately 10 % over 60 minuts), whilst the current in the sulphuric acid based electrolyte was stable.

The iridium oxide films were also characterised in sulphuric acid subsequent to the experiments in TFMSA with the redox couple in order to check for possible

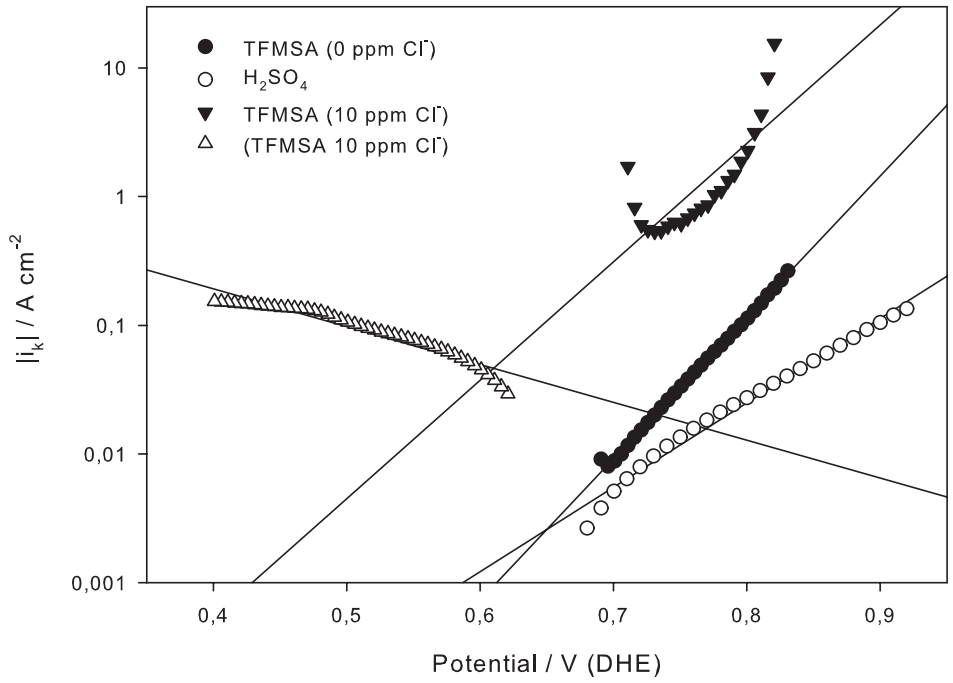

Figure 11.9: Plots of the absolute values of the kinetic current, i_k, obtained by extrapolation of data such as in Fig. 11.8 to infinite rotational velocity.

changes in the film. Cyclic voltammetry displayed no clear redox peaks nor further growth of the oxide layer, and a new oxide layer could only be produced after complete removal of the previous one. The presence or absence of chloride ions did not make a difference.

One observation should be mentioned with regard to AIROF electrodes and TFMSA solutions; the mechanical stability of the oxide layer was generally poor after experiments in TFMSA. Parts of the oxide layer could often be removed by rinsing the electrode with a jet of water from a spray bottle, leaving a metallic, shining surface. This was generally not observed after experiments in sulphuric acid.

TFMSA thus appears to significantly influence both redox reactions at the semiconducting, reduced form of the oxide (or hydroxide) and oxygen evolution at the metallic form. For PEMEL this has the practical implication that Nafion™ appears to be a very fortunate choice for this type of electrolyser, see Fig. 11.3. More fundamentally, however, the implication of the results obtained in sulphuric acid and TFMSA (Fig. 11.6) is that some caution should be exerted as far as characterisation of the electronic structure through electrochemical redox reactions [140].

All results presented above strongly indicate that TFMSA adsorbs to a significantly lesser degree than sulphate. Weaker adsorption in TFMSA than sulphate would cause the oxygen evolution reaction on AIROF to be faster in TFMSA than in sulphuric acid, as is also observed experimentally, see Fig. 11.3. This is further confirmed by the slightly higher flat band potential in TFMSA (Fig. 11.12)

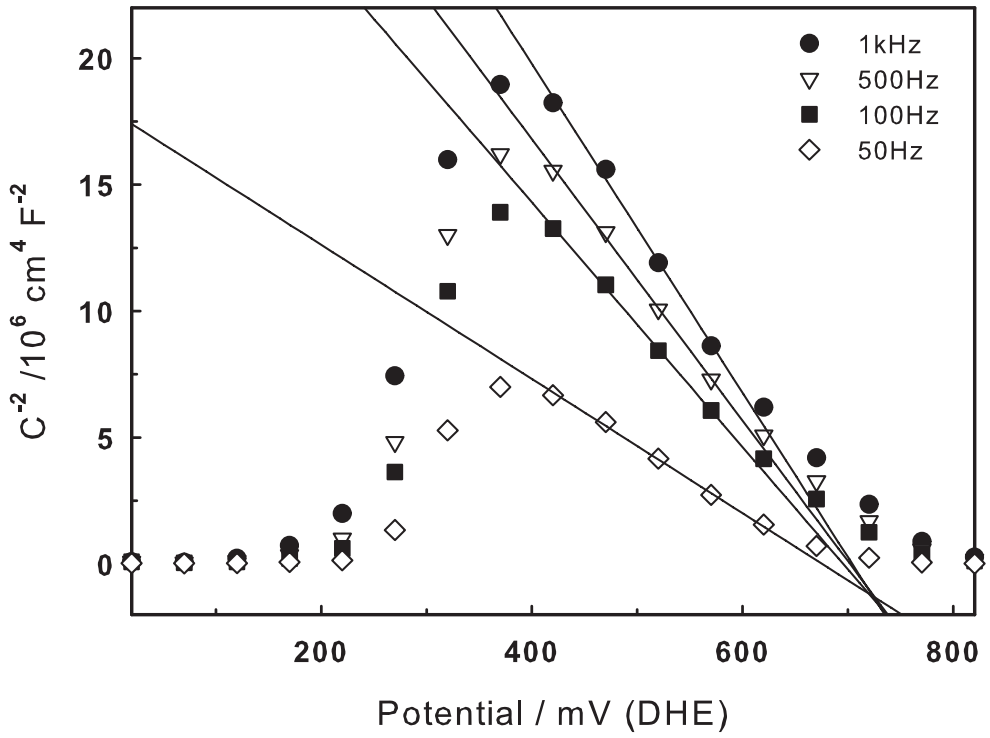

Figure 11.10: Capacitance-voltage relationship (Mott-Schottky) plots of AIROF in H_2SO_4 (pH 0.4) at different measurement frequencies.

than in sulphuric acid (Fig. 11.10) [25], which again indicates less adsorption of any TFMSA-derived anionic adsorbate.

The following explanations for the non-blocking behaviour in TFMSA with chloride ions can be envisioned: Specific adsorption of charged species on the oxide surface will change the alignment of the energy levels in the oxide with respect to the energy levels of the redox couple in the solution. This might give alignment of the energy levels making charge transfer (i.e electrochemical reactions) possible. The same line of reasoning can be applied to the case where surface states in the oxide are introduced by adsorption of TFMSA and chloride. Chemical reactions in the electrolyte between TFMSA, chloride and the redox couple could give a change in the solution energy levels making charge transfer possible.

Figures 11.10 and 11.12 show that the flat band potential changes only to a small degree between H_2SO_4 and TFMSA. To explain the change in behaviour, from blocking to non-blocking behaviour, the change in the flat band potential would have to be in the same order as the change between pH 0.4 to 13 [44], this corresponds to about 700 mV (see Fig 11.11). The small change observed in the flat band potential between H_2SO_4 and TFMSA can thus not explain the results, neither can surface states as these would have to imply electron accumulation at the surface [276, 277] to give the required shift in the flatband potential. Accumulation of electrons in the surface of a p-type semiconductor, would, however, be endothermic (excitation of

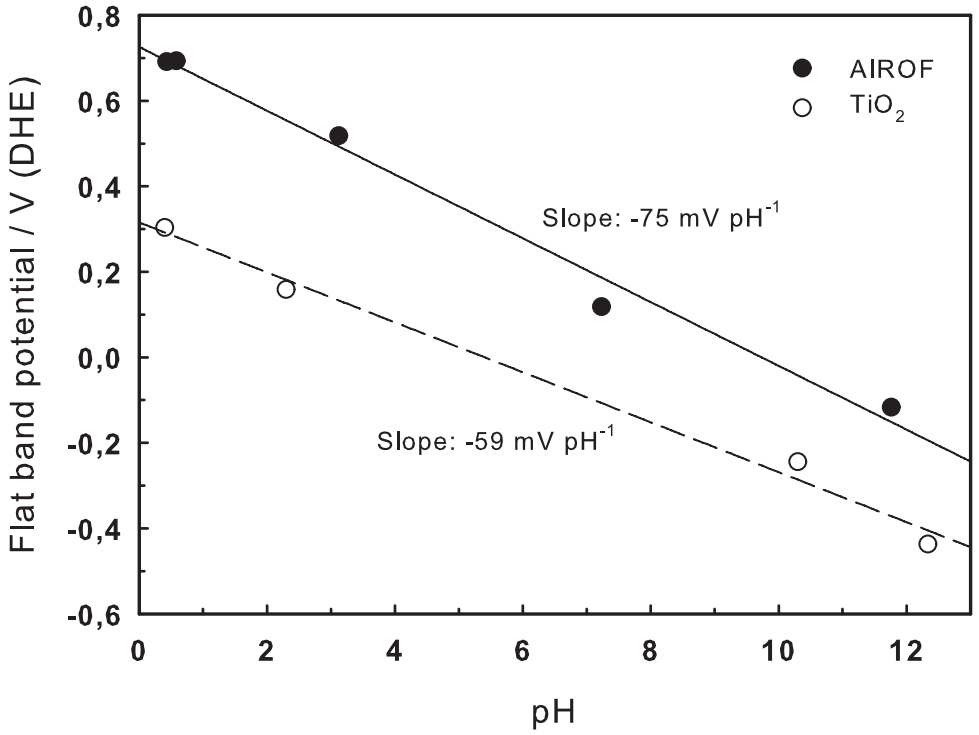

Figure 11.11: Dependence of flatband potential on pH for AIROF and TiO_2. The pH dependence was studied in solutions of H_2SO_4 where pH was adjusted by addition of NaOH.

electrons from valence band to surface states) and not likely to happen at the scale required. Moreover, this would again imply changes in the flatband potential which are not observed. As the presence or absence of chloride ions does not change the flat band potential in TFMSA the adsorption of TFMSA, in combination with chloride ions, can not be the explanation for the symmetric potential–current behaviour seen in TFMSA solutions containing Cl^-. As for chemical reactions taking place in the bulk electrolyte and thus changing the energy levels this can not be the case as the CVs on a platinum electrode in the different electrolytes are nearly identical, Fig 11.13.

A change in the electronic structure of the oxide itself from sulphuric acid to TFMSA-containing solutions is in principle also possible, since previous investigations show that anion uptake [34, 35, 114] takes place during redox cycling, c.f. the prepeak in Figure 11.2. Any irreversibility associated with this processes so that the film is poised in its metallic state is therefore in principle possible. Although this would comply with the fact that voltammograms in the background solutions, after experiments in the redox couple, displayed no redox peaks, we are, however, not aware of any observations of this nature in the literature.

In summary, then, full reconciliation of the redox behaviour of AIROF in TFMSA solutions containing hexacyanoferrates and chloride ions in terms of a semiconductor

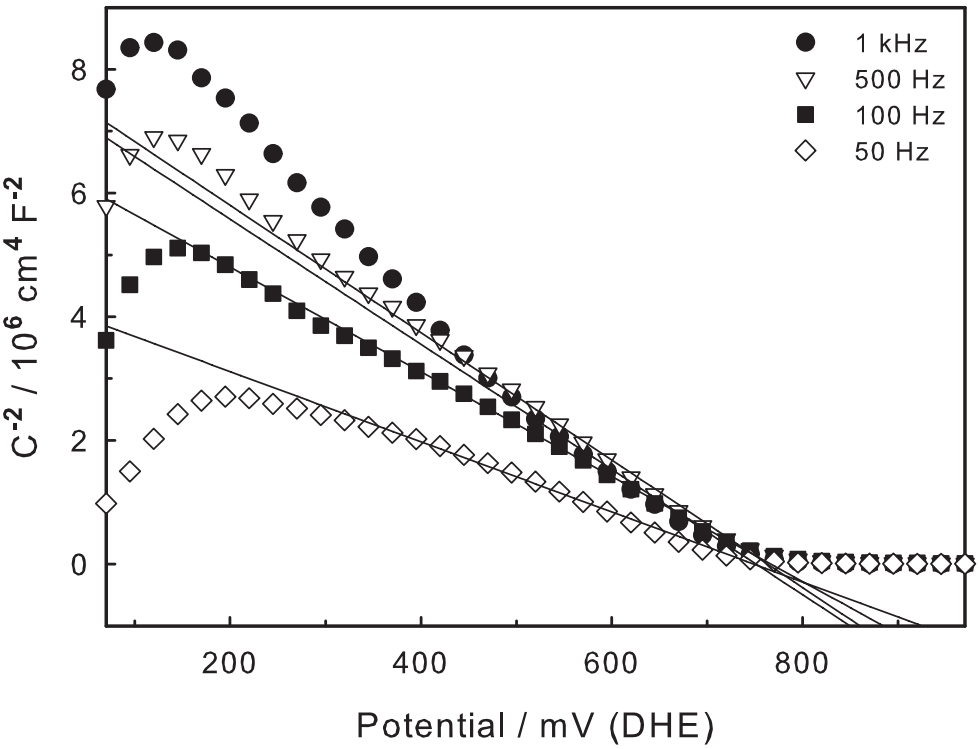

Figure 11.12: Capacitance-voltage relationship (Mott-Schottky) plots of AIROF in TFMSA (pH 0.4) in the presence of Cl^- at different measurement frequencies.

model for the oxide is difficult, and the electrochemical behaviour is only consistent with that of a metal electrode.

Previous studies show that AIROF displays a significant degree of cracking even after a small number of cycles [105, 120]. This does not seem to be the case in our study, see Figure 11.1. However the film appears to be highly porous and rough so that access to the metal is not unlikely. It is likely that in TFMSA solutions the access of the hexacyanoferrates to the underlying iridium metal substrate is better than in sulphuric acid. The rate constants for hexacyanoferrate oxidation and reduction estimated in TFMSA with chlorides are approximately 1 % of those observed at bare iridium metal electrodes [278], which is not unreasonable in view of the results in Ref. [120], and it actually appears more challenging to understand why the ferrates apparently do not get acces to the substrate in sulphuric acid.

In the end it appears that it is the presence of chloride ions that is the determining factor. It is likely that the AIROF contains cracks or cracks during transfer from the sulphuric solution it was made in to the test solution [120], or otherwise allows access to the iridium metal surface (see also Fig. 11.1). If the test solution is based on sulphuric acid the adsorption of sulphate species protects the exposed iridium metal against chloride ions in the solution, thus giving the oxide film a chance to regrow. In TFMSA, which does not seem to adsorb as strongly as sulphuric acid, the exposed iridium metal is not protected by adsorbed species, thus an oxide film

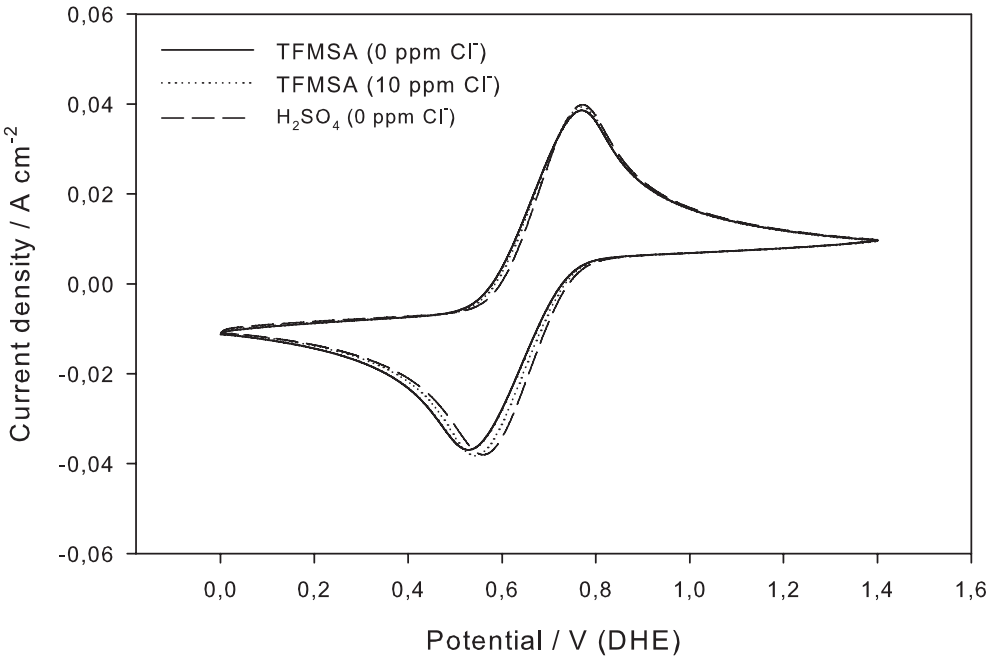

Figure 11.13: Cyclic voltammetry of $Fe(CN)_6^{3-}$ /$Fe(CN)_6^{4-}$ obtained on a platinum electrode. The measurements were carried out in both TFMSA (pH = 0.4, 0 and 10 ppm Cl^-) and H_2SO_4 (pH = 0.4, 0 ppm Cl^-). The scan rate was 200 mV/s.

can not be formed and the electrode will give a mixed oxide and metal behaviour that is, as seen in Fig 11.6, dominated by the metallic iridium signal. Mozota and Conway [115] showed that adsorption of Cl^- hinders the formation of thick AIROF films. Their results show that at 10 ppm Cl^- about 30 % of the iridium surface is hinderd from forming even the first monolayer of oxide. Furthermore on ruthenium oxide it is known that Cl^- adsorbs more weakly than HSO_4^- [91], thus it is likely that Cl^- are hindered from adsorbing in sulphuric acid solutions. Also growth of the oxide layer can be quick [111], so that any exposed iridium metal is rapidly reoxidised, in the absence of chloride, during the experiment thus giving a blocking behaviour. The potential limits used in the experiment (0–1.4 V) should be sufficient to grow AIROF [105, 108], see also Fig. 11.7. Lastly iridium is unstable in the presence of chloride as soluble species of the $IrCl_x$ type can be formed [115].

The decrease in the effective diffusion length as measured by impedance, Table 11.1, upon transference of the films from sulphuric acid to TFMSA electrolytes, and the SEM images, Fig. 11.1, appear to indicate that the crack structures in our solutions differ significantly from those described in Ref. [105, 117, 126].

The chronoamperometric measurements in pure TFMSA or sulphuric acid (with and without chloride) gives confidence to the use of AIROF insomuch as the stability should not be a problem during the time frame of the measurements. The decrease in current found in the conducted in the presence of the $Fe(CN)_6^{3-}$/$Fe(CN)_6^{4-}$ redox couple in TFMSA are indicative of a higher degree of adsorption of sulphate than

triflate, since a likely cause for the reduction in oxidation and reduction currents in the TFMSA solution is formation of Prussian blue, frequently observed at metal electrodes [269, 270, 279]. Prussian blue hinders the electron transfer. The surface in TFMSA is more open to the hexacyanoferrates and thus to their decomposition than in sulphuric acid. This therefore explains the more rapid current decay in the former than in the latter.

11.5 Conclusion

The addition of chloride to TFMSA changes the behaviour of an AIROF electrode dramatically. In its reduced state the oxide behaves as a semiconductor in sulphuric acid and in chloride free TFMSA. In particular, "blocking" of the current for reduction of hexacyanoferrat(III) is observed. However, in TFMSA-containing electrolytes cathodic blocking of the hexacyanoferrate couple was not observed in solutions containing chloride ions (at 10 ppm or higher concentrations), and in the latter solution the substrate-oxide system behaves in every respect as a metal electrode. The reasons for this behaviour is suggested to be due to an opening up of the oxide in TFMSA solutions coupled with chloride ions hindering reoxidising of the base metal. The hexacyanoferrate reactions can thus take place at the iridium substrate. Estimates of the rate constant for the hexacyanoferrate redox reaction indicates that approximately 1 % of the iridium-metal surface is exposed to the solution.

The OER on AIROF also appears to be significantly affected by the type of supporting electrolyte. Faster OER is observed in TFMSA compared to sulphuric acid. The data supports the notion of a stronger adsorption of sulphate than triflate since OER is expected to depend on the availability of free surface sites.

All in all, Nafion™ appears to be a very good choice for PEM electrolysers with iridium oxide as the electrocatalyst, and characterisation in sulphuric acid may underestimate the electrocatalytic properties of the oxide in a working PEM electrolyser. Equally important, any assessment of electronic structure of the oxide will have to very carefully take the effects of the supporting electrolyte in to account. In particular the effect of chloride ions should always be considered if there is a risk of contamination.

Acknowledgements

The authors would like to acknowledge the Norwegian Research Council for their financial support of the project through contract 159012 Electrocatalysts PEM water electrolysis.

Suzanne Paterson is acknowledged for her help with parts of the experimental work.

Chapter 12

The effect of phosphate on the oxygen evolution reaction on iridium oxide

Lars-Erik Owe, Mikhail Tsypkin, Svein Sunde

This article has been submitted. The layout of the article has been changed to improve readability, however the text and figures have not been changed.

12.1 Abstract

The rate of the oxygen evolution reaction (OER) at iridium oxide is significantly lower in phosphoric acid and sulphuric acid solutions than in perchloric acid solutions in the temperature range 0 °C to 150 °C. The results are interpreted as due to adsorption of phosphate on the oxide blocking active sites for intermediates in the OER by phosphoric acid moieties. The OER rate decreased with increasing phosphate concentration, and the oxygen-evolution current was proportional to the concentration of the electrolyte anion raised to -0.28 in phosphoric acid as compared to -0.84 in sulphuric acid. The activation energy for the OER was found to be 55 kJ/mol in phosphoric acid, 89 kJ/mol in sulphuric acid, and 85 kJ/mol in perchloric acid.

12.2 Introduction

Water electrolysis is an attractive method of producing hydrogen in an environmentally friendly fashion from electrical energy [70]. Polymer electrolyte membrane (PEM) water electrolysers, typically operating below 100 °C, have several advantages compared to traditional alkaline systems, including the high current densities, the lack of an alkaline electrolyte, pure products, and compact size [79, 80]. Since the thermal-balance potential [68, 69] increases with increasing temperature it may, however, be advantageous to operate the process above 100 °C.

Increasing the operating temperature of fuel cells causes problems as the typical Nafion® membranes loose their mechanical properties [280] and run the risk of dehydration causing loss of conductivity at temperatures above 100 °C [280,281]. A polybenzimidazole (PBI) membrane [282, 283] is one alternative that can be used at temperatures above 100 °C. However, the PBI membranes must be doped with phosphoric acid in order to achieve a sufficient conductivity [282].

Iridium and ruthenium oxides are commonly used as catalysts for the oxygen evolution reaction (OER) in acidic environments [85]. RuO_2 has the highest catalytic activity, but it is not stable enough. IrO_2 is not quite as active, but the stability is higher, making it a better candidate for practical applications, either alone or mixed with RuO_2 [252]. Usually, colloidal or other synthesis routes ensure that a large surface area are employed.

Phosphates are known to adsorb strongly on ruthenium oxide [91, p. 56]. The situation is not as clear on iridium oxide, but some investigations of adsorption on iridium oxide are available. Motoo and Furuya [284] showed that ClO_4^- adsorb less strongly than HSO_4^- on iridium metal electrodes. This was further confirmed by Fonesca and co-workers [108]. The presence of sulphate species and perchlorate species in iridium oxide films has been detected by IR spectroscopy and XPS [110, 111, 124], and phosphorous has been detected in anodically formed iridium oxide film (AIROF) by Auger electron spectroscopy [141]. The adsorption of trifluormethanesulfonic acid on AIROF has been examined by our group [2]. However, no study that focuses on adsorption of phosphates, sulphates or perchlorates on iridium oxide and the effect of adsorption on the OER has been found. As phosphates leached from the PBI membrane might adsorb on the catalyst it is of interest to study the effect of adsorption on the OER on iridium oxide. Alternatively the catalyst can in some cases come in direct contact with the polymer, for example if the polymer is mixed with the catalyst as a binder and to increase the three-phase region. Direct adsorption of phosphates from the catalyst is then possible.

The primary purpose of this work is to investigate the effect of phosphate adsorption on the OER at iridium oxide as a basis for assessment of employing phosphate-containing membranes in high temperature PEM water electrolysis. We also attempt to correlate this with the effect of phosphate on the intercalation properties of the oxide.

12.3 Experimental

12.3.1 Samples

Iridium foils (Sigma-Aldrich, 99.5 % purity, 0.1 mm thick) were used as working electrodes. A foil with a geometric area of 3.9 cm^2 was used for the measurements at temperatures between 0 and 80 °C and a foil with a geometric area of 2.0 cm^2 was used between 100 and 150 °C.

Before each experiment the iridium foil was polished to a mirror finish by hand using 1 μm diamond paste, rinsed in distilled water, boiled in 10 wt% HCl (Merck, pa) and finally rinsed in boiling distilled water four times.

The AIROF films were produced according to Gottesfeld and McIntryre [43]. Briefly, the iridium foil was cycled in 0.5 M H_2SO_4 between 0 and 1.5 V (NHE) at a sweep rate of 150 mV/s in room temperature, until the peak current of the main anodic peak (at about 1 V) reached 7.7 mA/cm^2. After transferring the electrode to the electrolyte being used for the particular experiment the electrode was cycled between 0.0 V and 1.4 V at 100 mV/s until the response was stable.

The iridium oxide powder electrodes were prepared using the thin-film technique [256]. Forty μg of iridium-oxide powder, produced by the hydrolysis method and heat treated in air at 600 °C for 30 minutes [188], dispersed in water was placed on a glassy-carbon rotating disk electrode (5 mm diameter) and dried in a nitrogen gas stream. Unlike Ref. [256] the catalyst was not covered with Nafion.

12.3.2 Electrochemical measurements

Electrochemical measurements at 0–80 °C were carried out in a standard three electrode cell. The cell was placed in a water bath for temperature control. A dynamic hydrogen reference electrode (DHE), in a Luggin capillary, in the test electrolyte was used for all measurements. The DHE was at the same temperature as the measurement was performed at. All potentials are reported against this reference electrode. A platinum foil of much greater area than the working electrode was used as the counter electrode. A Radiometer Analytical VoltaLab PGZ 301 potentiostat was used for all experiments except for the experiments on the iridium oxide powder electrodes where a Gamry Instruments Series G 300 potentiostat was used.

The measurements at temperatures of 100 °C and above were performed in a glass autoclave (a Miniclave from Büchi Glass Uster AG). The autoclave was allowed to pressurise naturally by the evaporation of the electrolyte. A DHE in the test electrolyte was used.

All solutions were prepared from water tapped from a Millipore Direct-Q system. The water had a resistivity of 18.7 MΩcm. 0.1 M and 0.5 M solutions of H_2SO_4 (Merck, p.a.), H_3PO_4 (SDS) and $HClO_4$ (Merck, Suprapure®) were prepared from the concentrated acid. The pH of the solutions containing a higher concentration of anions was kept as close as possible to the pH of the 0.5 M solution. This was done by mixing the acid with the corresponding potassium salt (K_2SO_4 (Merck, p.a.) or K_3PO_4 (Merck, extra pure)). The electrolytes were purged with argon gas (AGA, 5.0 purity) before and during the experiment, with no additional stirring. In the autoclave it was not possible to purge the electrolyte during the experiments.

Cyclic voltammograms (CVs) were recorded between 0.0 V and 1.4 V with sweep rates, ν, of 200, 100, 50, 20 and 10 mV/s. Polarisation measurements were recorded with a sweep rate of 5 mV/min, starting at the open circuit voltage and stopping at 1.7 V (1.6 V in the autoclave).

To account for the variations in the charge between each prepared oxide layer and between the powder electrode and the AIROF electrode the data were normalised with respect to the outer charge. The CVs, measured in the test electrolyte before recording the polarisation curve, were integrated from 0.4 V to 1.4 V to find the integrated charge, and the inner, outer and total charge was calculated using the method of Ardizzone and co-workers [13]. The outer charge, obtained by extrapolat-

ing the voltammetric charge vs. $1/\sqrt{v}$ (where v is the sweep rate) to zero ($v \to \infty$), was used for the normalisation.

12.3.3 EQCM measurements

An Elchema EQCN-700 instrument was used in combination with a Princeton Applied Research 2273 potentiostat. The auxiliary input of the potentiostat was used to acquire the mass signal from the EQCM.

10 MHz EQCM crystals with etched gold electrodes from International Crystal Manufacturing Co., Inc. (part # 151225-10) were used. The crystal diameter was 13.7 mm with an active gold area of diameter of 5.1 mm.

The oxide powder catalyst, the same as used for the other investigations, was applied to one side of the EQCM crystals. An ink containing the oxide and ethanol, mixed in an ultrasonic bath, was sprayed onto the electrode with an air brush (Badger 100G). A template with a circular hole of 4.0 mm was used.

Experiments were performed in the following electrolytes: 0.5 M $HClO_4$, H_2SO_4 and H_3PO_4 in addition to a solution with 1 mM of H_2SO_4 in 0.5 M $HClO_4$ and solutions with 1 mM and 10 mM of H_3PO_4 in 0.5 M H_2SO_4. All solutions were argon purged before the start of the measurements.

A DHE in the electrolyte was used, and all potentials are referred to this reference electrode. The reference electrode was placed in a Luggin capillary. A gold wire counter electrode was used.

The electrochemical measurements consisted of CVs at different sweep rates, with potential limits of 0 V to 1.4 V. 10 full cycles were recorded for each sweep rate (1, 10, 20, 50, 100, 200, 500 and 1000 mV/s). Before the start of the measurement CVs at 100 mV/s were conducted until a steady signal was recorded, typically 20 cycles sufficed.

The applied amount of catalyst was calculated using the Sauerberey equation [28]:

$$\Delta f = -\frac{2 f_0^2 \Delta m}{A(\mu_q \rho_q)^{\frac{1}{2}}} \tag{12.1}$$

In the equation Δf is the change of the resonance frequency of the EQCM crystal, $f_0 = 10$ MHz is the resonance frequency of the crystal as supplied, Δm is the mass change, A is the piezoelectric active area, ρ_q is the density and μ_q is the shear modulus of the crystal. For the set up used in this study, $A = 2.0 \cdot 10^{-5}$ m^2, $\rho = 2.648 \cdot 10^6$ g/m^3 and $\mu_q = 2.947 \cdot 10^{13}$ g/m s^2 [30].

The results reported here are from a crystal with initial frequency of 24832 Hz. The change in the frequency after applying the iridium oxide powder catalyst (measured in the dry state) was $\Delta f = -13775$ Hz . The applied catalyst loading was thus $\Delta m = 6.1$ µg, or $2.7 \cdot 10^{-8}$ mol (assuming IrO_2). The same electrode was used for all the experiments. The experiments were conducted in the order they are listed, i.e. in the order of the (assumed) increasing adsorption strength.

The mass data are normalised such that the mass of the electrode at 1.4 V is set to be zero. The value on the scale is thus the difference in weight between 1.4 V and the given potential.

12.4 Results

12.4.1 Voltammetry

The growth rate of the oxide layer, the colouration and bleaching of the film and the shape of the CVs in the growth solution were comparable to previous results, see for example [2, 43, 110, 136]. During the growth of the iridium oxide layer the peak current of the anodic and cathodic main peak at between 0.9 and 1.0 V increased linearly with the number of cycles. The onset of the oxygen evolution was visible at the highest potentials after about 100 cycles. A small anodic peak before the main anodic peak, generally referred to as the prepeak, grew at a slower rate than the main anodic peak. Its peak potential increased with increasing number of cycles until it appeared as a shoulder on the main peak. The same behaviour has been reported previously by Birss, Bock and Elzanowska [36]. Very little increase in the current was detected at potentials below 0.6 V.

Colouration and bleaching of the film were typically first observed between 100–200 cycles into the growth of the film. The film changed from the bleached state to the coloured state when the potential passed 0.8 V going in the anodic direction. On the return, cathodic, sweep the film was fully bleached at about 0.6 V.

When the film was transferred from the growth solution to the test solution the shape of the CV changed, particularly with respect to the anodic prepeak, during the first cycles. Figure 12.1 shows the first and 30th cycles after transferring the AIROF electrode from the sulphuric acid growth electrolyte to a 0.5 M phosphoric acid solution at 25 °C. The figure shows that cycling the electrode changed the shape of the prepeak dramatically, until it was a mere shoulder of the main peak [36, 108]. The current of the main anodic and cathodic peak also increased somewhat. No other significant changes were observed. After 30 cycles little further change was evident. The charge of the electrode before and after the transfer was comparable.

Colouration and bleaching was observed in phosphoric, sulphuric and perchloric acid at all concentrations. The CV recorded in sulphuric acid had a clearly defined anodic prepeak, at about 0.7 V, see Figure 12.1. In the cathodic direction no evidence of a prepeak was seen. The CV recorded in the perchloric acid differed to a large extent from CVs in the two other solutions, see Figure 12.1. However, it did resemble CVs recorded in trifluormethanesulfonic acid, an acid known to adsorb more weakly than sulphuric acid on AIROF [2]. An ill-defined anodic peak was visible at about 1.0 V. However it was overshadowed by a large anodic current, almost four times larger than the main anodic peak potential in phosphoric and sulphuric acid, at potentials above 1.2 V. Earlier results from Fonseca *et al.* [108] showed that the prepeak was more distincly visible in sulphuric acid than in perchloric acid, as observed here.

CVs on AIROF recorded in 0.5 M phosphoric acid for temperatures of 0 °C to 150 °C (the latter recorded in an autoclave) can be seen in Figure 12.2. While the main anodic peak potential is approximately the same, except for the measurement at 0 °C, the potential of the anodic prepeak decreases with increasing temperature, as has been observed before [136]. The anodic prepeak is not visible in the results at 0 °C, as the potential of the anodic prepeak is shifted to such an anodic potential

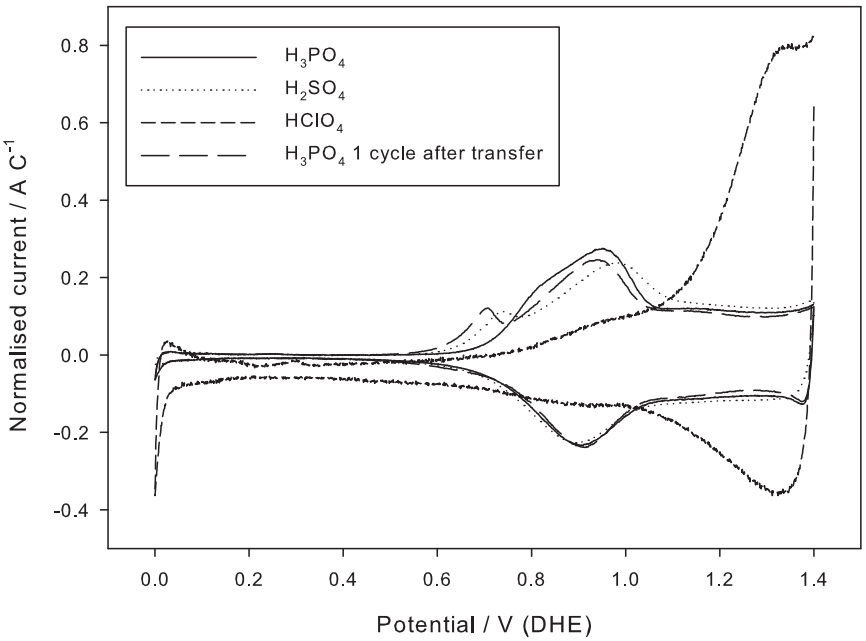

Figure 12.1: CVs in 0.5 M solutions of phosphoric, sulphuric and perchloric acid at 25 °C. The first cycle after transferring an AIROF electrode to 0.5 M phosphoric acid from 0.5 M sulphuric acid is also shown. At $\nu = 100$ mV/s.

that it has merged with the main peak. At 150 °C the anodic prepeak is rather smeared out, but follows the trend in that the peak appears at a lower potential than the measurements at lower temperatures. Experiments at 100 and 125 °C gave results intermediate to the experiments at higher and lower temperatures. The normalised current, both for the prepeak and the main anodic peak decreases with increasing temperature. This is, however, a normalisation artefact as the charge increases with temperature faster than the peak current. There appears to be no systematic variations in the cathodic peak potential. A similar effect of temperature was also seen in sulphuric and perchloric acid solutions, although the variations with temperature were not as clear in sulphuric acid solutions (not shown). Experiments on thermally prepared IrO_2 electrodes in perchloric acid also indicate a temperature independence of the main anodic peak [15].

CVs recorded at 25 °Cin solutions with phosphate concentrations of 1 M and 2 M at approximately constant pH were of similar shape as those in 0.5 M. The peak potential of the prepeak was shifted negatively by approximately 20 mV from 0.5 M to 1 M of phosphate concentration and another 40 mV from 1 M to 2 M, see Figure 12.3. This is in line with results in Ref. [36]. The main peak is substantially less affected and the small shift there is positive. For the powder electrode, which does not display a prepeak, there is practically no difference in the peak potential with concentration.

Systematic investigations made in References [32–34] indicate that cations [32, 127], exchange of anions [32] and exchange of water with the surrounding solu-

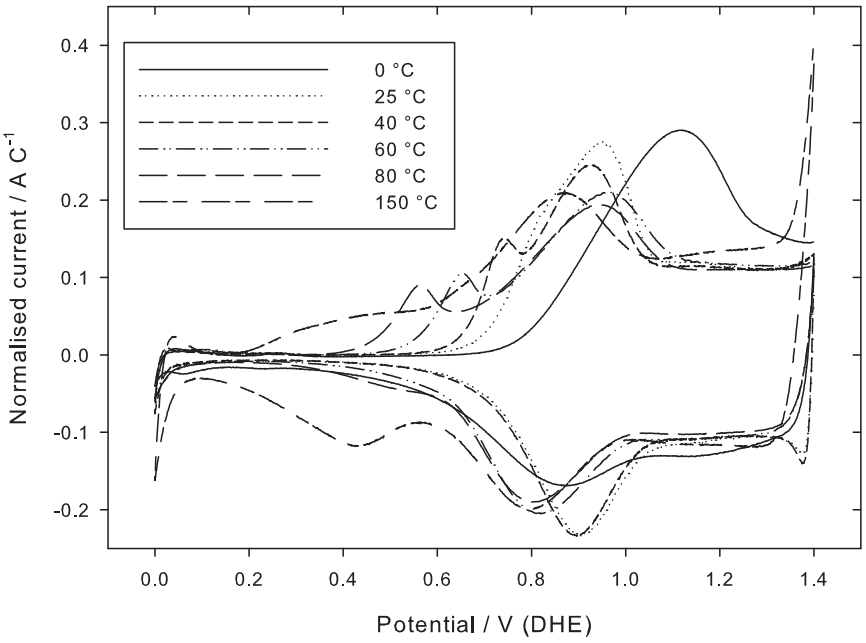

Figure 12.2: CVs of AIROF electrodes in 0.5 M phosphoric acid at temperatures between 0 °C and 150 °C. $\nu = 100$ mV/s

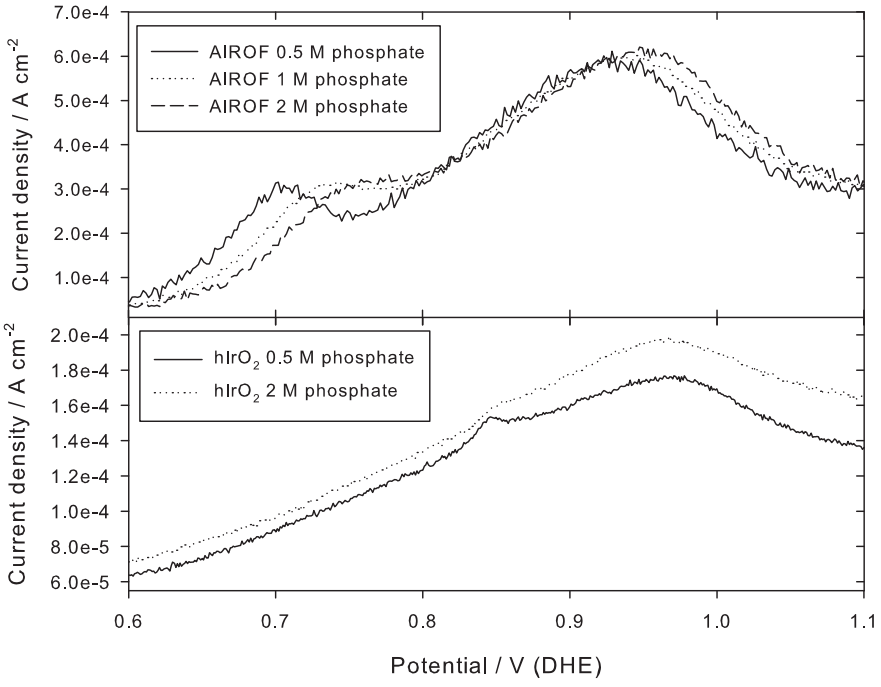

Figure 12.3: CVs of AIROF and iridium oxide powder (marked "$hIrO_2$") electrodes in phosphate solutions with different concentrations. $\nu = 10$ mV/s

tion [35] take place during the intercalation. The general reaction may be written [36]

$$\mathrm{IrO_2 \bullet nH_2O + (1+\delta)H^+ + \delta A^- + e^- \leftrightarrows IrO(OH)_{1+\delta}\delta A \bullet mH_2O + (n-m)H_2O} \quad (12.2)$$

where the values of the stoichiometric coefficients are different for the prepeak and the main peak so that δ is larger for the former than the latter. In line with previous results we thus interpret the higher sensitivity of the prepeak than the main peak to the solution anion as being due to finite values of δ in Eq. (12.2). The voltammograms performed at at high phosphate concentration and at temperatures higher than room temperature show that under the right conditions there is a clearly defined prepeak also in phosphate solutions. The negative shift of the prepeak potential with increasing phosphate concentration shows that the intercalation process therefore includes phosphate anions if these are present in the solution. Using the Nernst equation for reaction (12.2) [35] we find that during the reduction process approximately 1.2 protons are injected along with some 0.2 anions (assuming singly valent anions) for charge compensation. This indicates that the anion involvement is similar for phosphoric acid to that for sulphuric acid and perchloric acid [35].

Figure 12.1 shows that the CVs including the main anodic peak potentials in phosphoric and sulphuric acid were significantly different from that in perchloric acid. In all cases the peak current was proportional to the sweep rate, however, which indicates that diffusion is not important during the intercalation process. If so, this would violate the normalisation procedure employed below. In this case one would, since the peak potential was found to be practically independent of sweep rate, expect the current as function of the applied potential during the CV to vary as [12, p. 410 and p. 522]

$$i \propto v \frac{\exp\left[\left(\frac{nF}{RT}\right)(E - E^{0\prime})\right]}{\left\{1 + \exp\left[\left(\frac{nF}{RT}\right)(E - E^{0\prime})\right]\right\}^2} \quad (12.3)$$

where E is the applied potential as a function of time t and v the sweep rate ($E \propto vt$) and $E^{0\prime}$ the formal potential of the electrode. The voltammetric charge q^* between potential limits E_1 and E_2 is thus obtained from

$$q^* \propto v \int_{E_1}^{E_2} \frac{\exp\left[\left(\frac{nF}{RT}\right)(E - E^{0\prime})\right]}{\left\{1 + \exp\left[\left(\frac{nF}{RT}\right)(E - E^{0\prime})\right]\right\}^2} dt = \int_{E_1}^{E_2} \frac{\exp\left[\left(\frac{nF}{RT}\right)(E - E^{0\prime})\right]}{\left\{1 + \exp\left[\left(\frac{nF}{RT}\right)(E - E^{0\prime})\right]\right\}^2} dE \quad (12.4)$$

where we used that $dt = dE/v$. (The other symbols in the equations take their usual meaning.) Thus, q^* is, according to this model, constant and independent of the sweep rate. However, in our measurements q^* displayed a substantial decrease with sweep rate similar to that in Ref. [13] and the corresponding plots of q^* vs $1/\sqrt{v}$ and of $1/q^*$ vs $\sqrt{v}$ were reasonably linear, and in the absence of consistence with Eq. (12.4) above we continued to use the normalisation method of Ref. [13]. Evaluated this way the ratio between the outer and total charge also constituted another main difference in the voltammetric behaviour of anodically formed iridium

oxide in these solutions. For phosphate and sulphate solutions, the outer charge typically amounted to 90 % of the total charge, whereas in perchloric acid the number was much lower, typically around 15 %. This indicates that the internal distributions of anions in the oxide is different in the different solutions, with a relatively large amount of sulfate and phosphate at the oxide's outer or surface regions and vice versa for perchlorate. (The total charge was approximately the same in all solutions for AIROF.) For the powder electrodes the total and outer charges were rather similar in all solutions, and in view of Fig. 12.3 it appears that it is difficult to obtain information about the sorption of anions from voltammetry alone for this form of the oxide.

12.4.2 EQCM

Figure 12.4 shows the CV and frequency change of iridium oxide powder in 0.5 M $HClO_4$ including the corresponding CV. A close to linear frequency increase with increasing potential is observed, along with some hysteresis at the highest potentials. This behaviour was not seen in the other electrolytes. Figure 12.4 also shows the results in 0.5 M H_3PO_4. The frequency changes only to a small extent at the lower potentials, whereas a linear increase in the frequency with increasing potential is apparent at higher potentials. The results in 0.5 M H_2SO_4 were similar to those in phosphoric acid and also to those conducted in sulphuric acid by Birss, Elzanowska and Gottesfeld [34]. The measurement in sulphuric acid displayed a frequency change intermediate between those in perchloric and phosphoric acids. An experiment on an electrode without catalyst, i.e. pure gold, was also conducted. The frequency of the gold electrode had a minimum at about 0.4 V with a rising frequency at increasing potentials beyond 0.4 V. To the extent that pinholes in the electrocatalyst layers would affect the measurements, they would therefore do so by decreasing the measured frequency changes reported relative to the true ones. However, the total frequency change of the bare gold electrode was approximately 10 % of those for the oxide covered electrode. We do not therefore consider the response of the gold substrate to influence the measurements to any significant extent.

Comparison of the above results with experiments at electrodes at which half the amount of iridium oxide was applied showed that the EQCM frequency change during oxidation or reduction was approximately linear in oxide mass. This indicates that the oxide films are acoustically thin and that the observed frequency changes are due to mass changes and not to changes in viscoelastic response [285] or roughness [286]. (Also, the frequency changes apparent in Figure 12.4 are much larger than those expected even for changes in surface roughness corresponding to protrusions of 50 nm.) If the effect of roughness of the electrode and changes in the viscoelastic properties do not affect the measurements the frequency shift is related to the mass shift by $\Delta f = -1.132 \cdot 10^9$ Hz/g $\cdot \Delta m$. This then corresponds to a total mass change of 98 ng in the perchloric acid solution and 193 ng in the phosphoric acid solution, both at 50 mV/s. (In sulfuric acid the corresponding number was 135 ng at this sweep rate.)

The frequency shifts (or mass changes) indicate clear differences between the different electrolytes, and shows that there are significant differences in anion-oxide

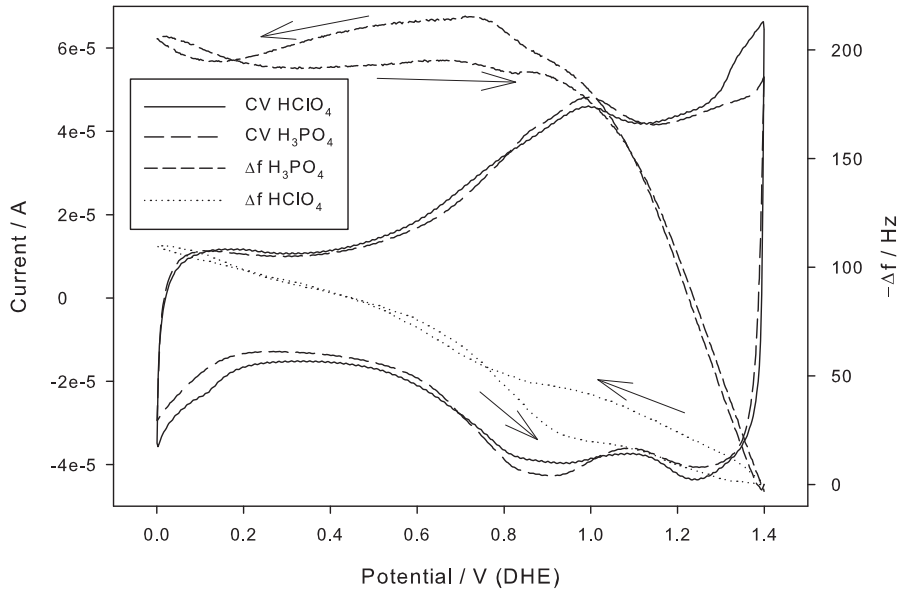

Figure 12.4: CV and frequency change in 0.5 M $HClO_4$ and 0.5 M H_3PO_4 at 50 mV/s on iridium oxide catalyst.

interaction also in this case, see Figure 12.4. It turned out that in phosphoric acid and sulfuric acid it was possible to analyse the EQCM data in a fashion analougous to the separation of the charge into outer and inner charges. Thus, the ratio of inner mass change to total mass change was 69 % and 85 % in phosphoric acid and sulfuric acid, respectively. The corresponding inner and total charges were 76 % and 84 %, in close agreement with the EQCM data. In perchloric acid the mass changes were almost constant as a function of sweep rate, and a similar analysis was not possible. The charge ratio was 72 % in this case, however.

The mass changes per Ir(+III) site oxides (or Ir(+IV) sites reduced) are 1.2 g/mol in phosphoric acid, 0.9 g/mol in sulphuric acid, and 0.6 g/mol in perchloric acid, indicating that the ratio $\delta/(n-m)$, Eq. (12.2), increases in the order $HClO_4 < H_2SO_4 < H_3PO_4$.

12.4.3 Current-potential behaviour

Polarisation curves recorded in 0.5 M solutions of phosphoric, sulphuric and perchloric acid at 24 °C at AIROF are shown in Figure 12.5. The OER is clearly fastest in perchloric acid at all potentials. The difference between sulphuric and phosphoric acid in terms of the rate of the OER is minimal. A close to linear region can be seen for the intermediate potentials. At higher potentials the slope increases. The ohmic resistance recorded in the system was in the range of 0.2–0.3 Ω.

Polarisation measurements were conducted also at temperatures up to 80 °C in the same solutions. In phosphoric acid the results at low potentials are as expected, with an increase in temperature giving a higher current at any given potential.

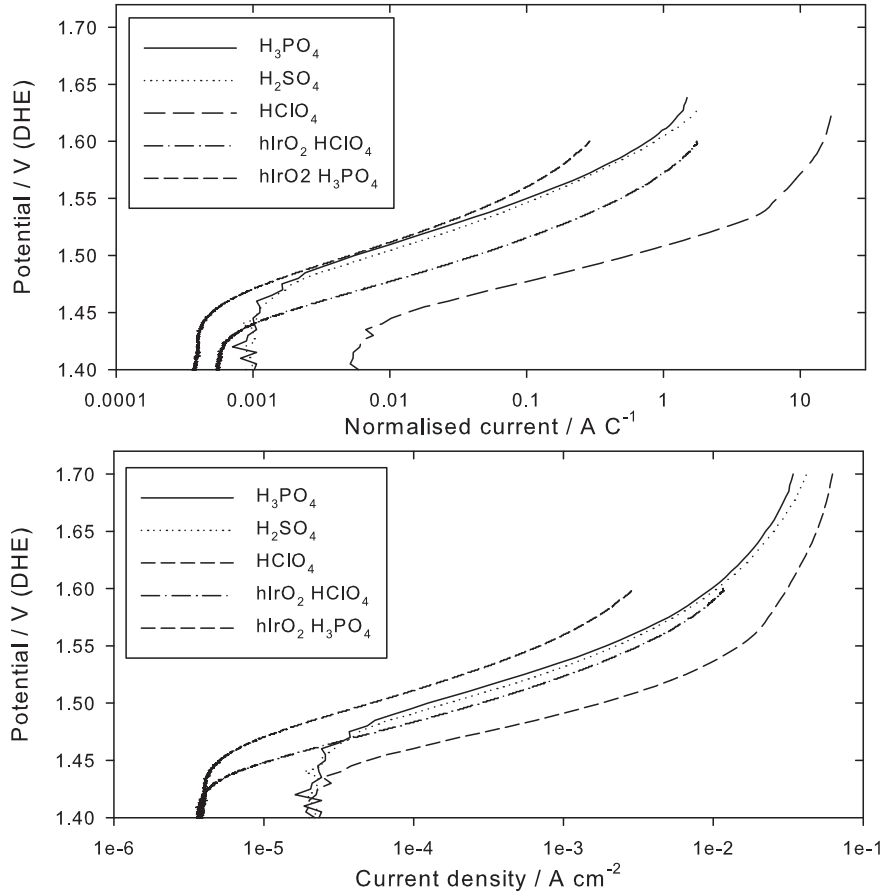

Figure 12.5: Polarisation measurements of AIROF electrodes in 0.5 M phosphoric, sulphuric and perchloric acid at 24 °C. Both the data that has been normalised and ohmic resistance corrected (top diagram) and the uncorrected current density (bottom diagram) are shown. $\nu = 5$ mV/min. Measurements of iridium oxide powder in 0.5 M phosphoric and perchloric acid are also given, they are marked "hIrO$_2$ H$_3$PO$_4$" and "hIrO$_2$ HClO$_4$" respectively.

Figure 12.5 also includes measurements on electrodes with iridium oxide powder. The iridium oxide electrode in phosphoric acid appears to give a slightly poorer result for the OER, especially at higher potentials, than the AIROF electrode. Also for the powder electrodes the current for the OER in perchloric acid was significantly faster at all potentials than in phosphoric acid. As the maximum current recorded for the powder electrodes was about 2 mA the ohmic drop in the solution is negligible in this case, and the curve has not been IR-corrected. However, because of problems encountered at large gas evolution rates, such as blocking and catalysts detachment, the polarisation measurement was stopped at 1.6 V.

Polarisation measurements recorded in an autoclave at 150 °C were similar to those at lower temperatures. Again, the OER was significantly faster in perchloric acid than in sulphuric acid, in turn faster than in phosphoric acid.

The apparent Tafel slope, b_a, was calculated from the approximately linear region of the polarisation curves for a selection of the polarisation measurements, ranging from 35 mV in 0.5 M perchloric acid to 60 mV in 2 M phosphoric acid at 25 °C. The values for the apparent Tafel slope are in the same range as reported previously [65, 144]. The values did not appear to change significantly with temperature [250, 287], but the Tafel slope did seem to increase with increasing concentration of phosphates.

The apparent activation energy, E_{act}, for the OER was taken as the slope of the straight line fitted to the logarithm of the current vs inverse temperature as shown in Figure 12.6. The current at 1.5 V was used for the calculations. The current was in the linear Tafel-region for all measurements. Although data for measurements between 0 and 150 °C are presented, only the data recorded at temperatures between 0 and 80 °C were used to calculate the activation energy. This is to avoid any possible effects of the system being pressurised at temperatures of 100 °C and above. The influence of the anion concentration on the rate of the OER was estimated for phosphates and sulphates from the slope of logarithmic plots of current at 1.5 V vs. concentration. These data suggest that the combined effect of the anion of the solution and the temperature on the current may be represented by:

$$i = i_a C^n \exp\left(\frac{E_{act}}{RT}\right) \tag{12.5}$$

In Equation (12.5) C is the anion concentration, n an exponent, i_a the preexponential of the current in absence of adsorption, and R and T take their usual meaning.

The activation energies were 55 kJ/mol in phosphoric acid, 89 kJ/mol in sulphuric acid, and 85 kJ/mol in perchloric acid, respectively, c. f. Ref. [81] . The exponent n for the anion concentration in the solution was -0.28 in phosphoric acid and -0.84 in sulphuric acid. As the exponent n is only found from experiments conducted at 25 °C, equation (12.5) should be used with some caution at temperatures other than 25 °C.

The important aspect of the findings here is that the rate of the OER will decrease significantly in case of leakages of phosphoric acid from state-of-art high-temperature PEMWE membranes, see Figure 12.5. The higher temperature of this type of electrolysis, as compared to classical PEM, will to some extent offset the adverse effect of any phosphoric acid leakages, depending on the current. In the pseudo-Tafel range where the voltage is roughly proportional to the logarithm of the current (for example the range 0.01 AC^{-1} through 1 AC^{-1} for perchloric acid in Figure 12.5) the rate of the OER will change with temperature through an activation energy of some 55–89 kJ/mol and thus be significant.

The practical implications of these results is that careful deliberations are necessary whether it is advantageous to increase the temperature of the WE if that requires the use of phosphate containing electrolytes. The increase in the temperature must be so large that the negative effects of switching to a phosphate based electrolyte membrane are compensated for by the higher increase in the performance because of the higher temperature. This in turn depends on the current at which the electrolyser is to operate.

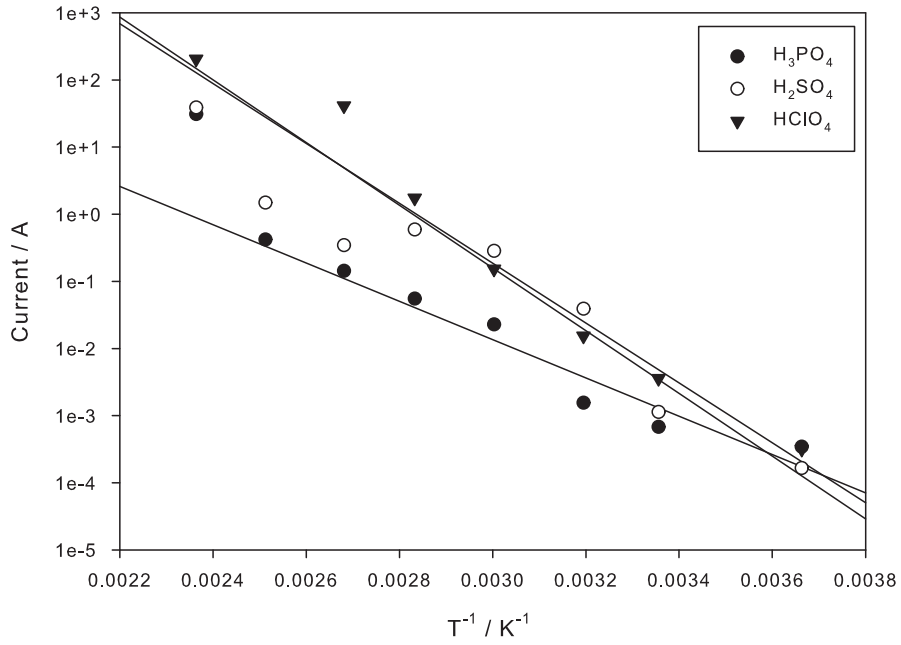

Figure 12.6: Arrhenius plot for the OER in 0.5 M solutions of phosphoric, sulphuric and perchloric acid. The current at 1.5 V is plotted. Data from 0–150 °C is presented, however only the data between 0 and 80 °C is used for the curve fitting.

12.5 Conclusion

A study of the effect of the electrolyte on the oxygen evolution reaction in conditions relevant for high temperature PEM water electrolysis has been performed. The effect of the temperature, the anion species and the anion concentration has been investigated on both AIROF and iridium oxide powder electrodes at temperatures between 0 and 150 °C.

The experiments show that the oxygen evolution activity is highest in perchlorate solutions and lowest in phosphate solutions. Increasing the temperature gives a faster OER, but the OER is still significantly slower in phosphoric acid solutions. The OER rate decreases with increasing anion concentration. The activation energy for the OER was found to be 55 kJ/mol in 0.5 M phosphoric acid, 89 kJ/mol in sulphuric acid and 85 kJ/mol in perchloric acid. A tentative equation is proposed that might serve as a basis for estimating the performance of iridium oxide as an electrocatalyst in high-temperature PEM water electrolysis.

For AIROF the electrocatlytic activity for the OER correlates with the appearance of the CVs and for the powder electrodes with a higher ratio between the degree of anion to water incorporation during intercalation reactions.

12.6 Acknowledgements

Suzanne Paterson, Carl Erik Lie Foss and Kristin Bergum were of great assistance during the laboratory work. Parts of this work is financed by the European Union through the WELTEMP project (web-page: http://www.weltemp.eu/, project nr.: 212903). Lars-Erik Owe wishes to thank the Department of Materials Science and Engineering at NTNU for financing.

Part III

Conclusions

Chapter 13

Conclusions

13.1 Adsorption

The adsorption of anions from the electrolyte will effect the rate of the oxygen evolution reaction on iridium oxide catalysts. Of the electrolytes investigated during this work the rate of the oxygen evolution reaction (OER) is highest in perchloric acid and trifluoromethanesulfonic acid (TFMSA), while it is slowest in phosphoric acid. The rate of the OER in sulphuric acid is intermediate to that in TFMSA and phosphoric acid. For the investigations both anodically formed iridium oxide films (AIROF) and iridium oxide powder electrodes were used.

The practical implication of adsorption of anions is that the choice of polymer electrolyte membrane used in an electrolyser will effect the performance of the catalyst. Nafion, which is close to TFMSA, is a particularly good choice for the membrane material as the species that can leak out of Nafion adsorbs weakly on iridium oxide. On the other hand phosphoric acid doped polybenzimidazole membranes can lead to phosphate adsorption on iridium oxide, slowing the rate of the OER significantly. In other words the water electrolyser should be designed such that species that adsorb strongly on the catalyst, and thus decrease the rate of the OER, can not come in contact with the catalyst.

13.2 Impedance modelling

An impedance model for porous intercalation electrodes with the possibility of mixed conductivity was developed. To facilitate the interpretation the limiting behaviour of the model was investigated. Several differences in the impedance diagrams of systems with metallic conductivity and those of mixed conductivity can be found.

An impedance model was also developed for intercalation electrodes with mixed conductivity. The model was used to study AIROF electrodes in sulphuric acid solutions. The model was found to describe the impedance of AIROF quite well. It was found that to fully describe the AIORF electrode the effects of diffusion (including the possibility of trapping of the charge carriers), faradaic reactions and potential differences must be included in the model. The model did, however, not allow the prediction of conductivity changes in the electrode.

13.3 Conductivity changes in iridium oxide

Iridium-tin oxide catalysts were examined by impedance to look for conductivity changes with potential. No strong evidence for this could be found. However, it was found that the conductivity of the samples changed with the heat treatment. Samples heat treated at 500 °C appeared to have a higher conductivity than samples heat treated at 400 °C.

For AIROF the impedance model that was developed could not predict conductivity changes in the oxide. Neither could the experimental impedance results show clear evidence for the semiconductor to conductor transition in AIROF upon oxidation.

13.4 Mixed oxide powder catalysts and segregation

Several compositions of mixed iridium and ruthenium oxide powder catalysts have been produced. The catalysts were studied by comparisons of the electrochemical response of the catalysts with those of physical mixes of the pure oxides and XRD experiments. It was found that the produced catalysts were not chemically mixed, but rather a multi phase system is formed. It is likely it contains a relatively pure iridium oxide phase and a mixed phase that is different from pure ruthenium oxide.

Iridium-tin oxide catalysts were prepared by the polyol method. XPS results indicate an enrichment of tin in the surface of the catalyst for the sample with composition $Ir_{0.75}Sn_{0.25}O_2$, whilst the surface composition of the $Ir_{0.5}Sn_{0.5}O_2$ sample was equal to the bulk composition. Furthermore it was found that the electrodes prepared with $Ir_{0.5}Sn_{0.5}O_2$ and $Ir_{0.75}Sn_{0.25}O_2$ heat treated at 500 °C and pure iridium oxide behaved as porous electrodes. The remaining samples, mixed iridium-tin oxide samples heat treated at temperatures lower than 500 °C, behaved as dense film electrodes. Mott–Schottky behaviour was only observed for the samples that behaved as films.

Part IV

Back matter

References

[1] S. Sunde, I.A. Lervik, L.-E. Owe Owe, and M. Tsypkin. An Impedance Model for a Porous Intercalation Electrode with Mixed Conductivity. *J. Electrochem. Soc.*, 156:B927–B937, 2009.

[2] L.-E. Owe, I. A. Lervik, M. Tsypkin, M. V. Syre, and S. Sunde. Electrochemical behaviour of iridium oxide films in trifluormethanesulfonic acid. *J. Electrochem. Soc.*, 157:B1719–B1725, 2010.

[3] D. Abbott. Keeping the energy debate clean: How do we supply the world's energy needs? *Proceed. IEEE*, 98(1):42–66, 2010.

[4] P. Kruger. Electric power requirement for large-scale production of hydrogen fuel for the world vehicle fleet. *Int. J. Hydrogen Energy*, 26:1137–1147, 2001.

[5] B. Árnason and T.I. Sigfússon. Iceland—a future hydrogen economy. *Int. J. Hydrogen Energy*, 25:389–394, 2000.

[6] C. Stiller, U. Bünger, S. Møller-Holst, A.M. Svensson, K.A. Espegren, and M. Nowak. Pathways to a hydrogen fuel infrastructure in Norway. *Int. J. Hydrogen Energy*, 35:2597–2601, 2010.

[7] Georg A. Olah, Alain Goeppert, and G. K. Surya Prakash. *Beyond Oil and Gas: The Methanol Economy*. Wiley-VCH, Weinheim, 2006.

[8] R. Tunold, A.T. Marshall, E. Rasten, M. Tsypkin, L..E. Owe, and S. Sunde. Materials for Electrocatalysis of Oxygen Evolution Process in PEM Water Electrolysis Cells. *ECS Trans.*, 25:103–117, 2010.

[9] T. Nakagawa, C.A. Beasley, and R.W. Murray. Efficient Electro-Oxidation of Water near Its Reversible Potential by a Mesoporous IrO_x Nanoparticle Film. *The Journal of Physical Chemistry C*, 113:12958–12961, 2009.

[10] Carl H. Hamann, Andrew Hamnett, and Wolf Vielstich. *Electrochemistry*. Wiley-VCH, Weinheim, 1998.

[11] D. Pletcher, R. Greef, R. Peat, L.M. Peter, and J. Robinson. *Instrumental methods in electrochemistry*. Woodhead Publishing, Chichester, 2001.

[12] A.J. Bard and L.R. Faulkner. *Electrochemical methods: Fundamentals and applications*. Wiley, New York, 2001.

[13] S. Ardizzone, G. Fregonara, and S. Trasatti. "Inner" and "outer" active surface of RuO_2 electrodes. *Electrochim. Acta*, 35:263–267, 1990.

[14] W. Sugimoto, T. Kizaki, K. Yokoshima, Y. Murakami, and Y. Takasu. Evaluation of the pseudocapacitance in RuO_2 with a RuO_2/GC thin film electrode. *Electrochim. Acta*, 49:313–320, 2004.

[15] S. Fierro, L. Ouattara, E.H. Calderon, and C. Comninellis. Influence of temperature on the charging/discharging process of IrO_2 coating deposited on p-Si substrate. *Electrochem. Commun.*, 10:955–959, 2008.

[16] S. Ardizzone, C. Bianchi, L. Borgese, G. Cappelletti, C. Locatelli, A. Minguzzi, S. Rondinini, A. Vertova, P. Ricci, C. Cannas, and A. Musinu. Physicochemical characterization of IrO_2–SnO_2 sol-gel nanopowders for electrochemical applications. *J. Appl. Electrochem.*, 39:2093–2105, 2009.

[17] J. Hu, J. Zhang, H. Meng, and C. Cao. Microstructure, electrochemical surface and electrocatalytic properties of IrO_2+Ta_2O_5 oxide electrodes. *J. Mater. Sci.*, 38:705–712, 2003.

[18] J.E. Ferrer and Ll. Victori. Oxygen evolution reaction on the iridium electrode in basic medium studied by electrochemical impedance spectroscopy. *Electrochim. Acta*, 39(4):581–588, 1994.

[19] J.E. Ferrer and Ll. Victori. Study of the oxygen evolution reaction on the iridium electrode in acid medium by eis. *Electrochimica Acta*, 39(5):667–672, 1994.

[20] M.E.G. Lyons and M.P. Brandon. The significance of electrochemical impedance spectra recorded during active oxygen evolution for oxide covered Ni, Co and Fe electrodes in alkaline solution. *J. Electroanal. Chem.*, 631:62–70, 2009.

[21] N.F. Mott. The Theory of Crystal Rectifiers. *Proceed. Roy. Soc. London Ser. A. Math. Phys. Sci.*, 171:27–38, 1939.

[22] V.W. Schottky. Zur Halbleitertheorie der Sperrshict- und Spitzengleichrichter. *Z. Phys.*, 113:367–414, 1939.

[23] V.W. Schottky. Vereinfachte und erweiterte Theorie der Randschichtgleichricter. *Z. Phys.*, 118:539–592, 1941.

[24] J. Ross Macdonald. *Impedance spectroscopy, Emphasizing Solid Materials and Systems*. John Wiley & Sons, New York, 1987.

[25] D. Kong, S. Chen, C. Wang, and W. Yang. A study of the passive films on chromium by capacitance measurement. *Corros. Sci.*, 45:747–758, 2003.

[26] N.E. Hakiki, M.D.C. Belo, A.M.P. Simoes, and M.G.S. Ferreira. Semiconducting Properties of Passive Films Formed on Stainless Steels. *J. Electrochem. Soc.*, 145:3821–3829, 1998.

[27] R.A.L. Vanden Berghe, F. Cardon, and W.P. Gomes. On the electrochemical reactivity of the redox couple $Fe(CN)_6^{3-}/Fe(CN)_6^{4-}$ at the single crystal zinc oxide electrode. *Surf. Sci.*, 39:368–384, 1973.

[28] D.A. Buttry and M.D. Ward. Measurement of interfacial processes at electrode surfaces with the electrochemical quartz crystal microbalance. *Chem. Rev.*, 92:1355–1379, 1992.

[29] G. Sauerbrey. Verwendung von Schwingquarzen zur Wägung dünner Schichten und zur Mikrowägung. *Z. Phys.*, 155:206–222, 1959.

[30] G.S. Ostrom and D.A. Buttry. Quartz crystal microbalance studies of deposition and dissolution mechanisms of electrochromic films of diheptylviologen bromide. *J. Electroanal. Chem.*, 256:411–431, 1988.

[31] E.N. El Sawy and V.I. Birss. Nano-porous iridium and iridium oxide thin films formed by high efficiency electrodeposition. *J. Mater. Chem.*, 19:8244–8252, 2009.

[32] Y. Jung, J. Lee, and Y. Tak. Electrochromic Mechanism of IrO_2 Prepared by Pulsed Anodic Electrodeposition. *Electrochem. Solid-State Lett.*, 7:H5–H8, 2004.

[33] J. Juodkazytė, B. Sebeka, G. Stalnionis, and K. Juodkazis. EQCM study of iridium anodic oxidation in H_2SO_4 and KOH solutions. *Electroanal.*, 17:1734–1739, 2005.

[34] V.I. Birss, H. Elzanowska, and S. Gottesfeld. Quartz crystal microbalance measurements during oxidation/reduction of hydrous Ir oxide electrodes. *J. Electroanal. Chem.*, 318:327–333, 1991.

[35] C. Bock and V.I. Birss. Anion and water involvement in hydrous Ir oxide redox reactions in acidic solutions. *J. Electroanal. Chem.*, 475:20–27, 1999.

[36] V.I. Birss, C. Bock, and H. Elzanowska. Hydrous Ir oxide films: the mechanism of the anodic prepeak reaction. *Can. J. Chem.*, 75:1687–1693, 1997.

[37] J. Juodkazytė, R. Vilkauskaite, G. Stalnionis, B. Sebeka, and K. Juodkazis. EQCM study of Ru and RuO_2 surface electrochemistry. *Electroanal.*, 19:1093–1099, 2007.

[38] Y. Sugawara, A.P. Yadav, A. Nishikata, and T. Tsuru. EQCM Study on Dissolution of Ruthenium in Sulfuric Acid. *J. Electrochem. Soc.*, 155:B897–B902, 2008.

[39] E. Calderon, R. Wüthrich, P. Mandin, G. Fóti, and C. Comninellis. Estimation of the effectiveness factor of an outer-sphere redox couple (Fe^{3+}/Fe^{2+}) using rotating disk Ti/IrO_2 electrodes of different loading. *J. Appl. Electrochem.*, 39:1379–1384, 2009.

[40] C.G. Granqvist. Electrochromic oxides: a bandstructure approach. *Sol. Energy Mater. Sol. Cells*, 32:369–382, 1994.

[41] L. Tronstad. The investigation of thin surface films on metals by means of reflected polarized light. *Trans. Faraday Soc.*, 29(140):502–514, 1933.

[42] S. Gottesfeld, J.D.E. McIntyre, G. Beni, and J.L. Shay. Electrochromism in anodic iridium oxide films. *Appl. Phys. Lett.*, 33:208–210, 1978.

[43] S. Gottesfeld and J.D.E. McIntyre. Electrochromism in Anodic Iridium Oxide Films. *J. Electrochem. Soc.*, 126:742–750, 1979.

[44] I.A. Lervik, M. Tsypkin, L.-E. Owe, and S. Sunde. Electronic structure vs. electrocatalytic activity of iridium oxide. *J. Electroanal. Chem.*, 645:135–142, 2010.

[45] G.A. Parks and P.L. De Bruyn. The zero point of charge of oxides. *J. Phys. Chem.*, 66:967–973, 1962.

[46] G.A. Parks. The Isoelectric Points of Solid Oxides, Solid Hydroxides, and Aqueous Hydroxo Complex Systems. *Chem. Rev.*, 65:177–198, 1965.

[47] B. Prelot, C. Poinsignon, F. Thomas, E. Schouller, and F. Villieras. Structural-chemical disorder of manganese dioxides: 1. Influence on surface properties at the solid-electrolyte interface. *J. Colloid Interface Sci.*, 257:77–84, 2003.

[48] T. Wakamatsu and S. Mukai. Behavior of hydrogen and hydroxyl ions at the oxide-water interface. *AIChE Symp. Ser.*, 71:81–87, 1975.

[49] J.S. Noh and J.A. Schwarz. Estimation of the point of zero charge of simple oxides by mass titration. *J. Colloid Interface Sci.*, 130:157–164, 1989.

[50] K. Bourikas, J. Vakros, C. Kordulis, and A. Lycourghiotis. Potentiometric Mass Titrations: Experimental and Theoretical Establishment of a New Technique for Determining the Point of Zero Charge (PZC) of Metal (Hydr)Oxides. *J. Phys. Chem.*, 107:9441–9451, 2003.

[51] J. Vakros, C. Kordulis, and A. Lycourghiotis. Potentiometric mass titrations: a quick scan for determining the point of zero charge. *Chem. Commun.*, 2002:1980–1981, 2002.

[52] K. Bourikas, C. Kordulis, and A. Lycourghiotis. Differential Potentiometric Titration: Development of a Methodology for Determining the Point of Zero Charge of Metal (Hydr)oxides by One Titration Curve. *Environ. Sci. Technol.*, 39:4100–4108, 2005.

[53] S.M. Ahmed. Studies of the dissociation of oxide surfaces at the liquid-solid interface. *Can. J. Chem.*, 44:1663–1670, 1966.

[54] K. Hu, F.F. Fan, A.J. Bard, and A.C. Hillier. Direct Measurement of Diffuse Double-Layer Forces at the Semiconductor/Electrolyte Interface Using an Atomic Force Microscope. *J. Phys. Chem. B*, 101:8298–8303, 1997.

[55] A.G. Stack, S.R. Higgins, and C.M. Eggleston. Point of zero charge of a corundum-water interface probed with optical second harmonic generation (SHG) and atomic force microscopy (AFM): New approaches to oxide surface charge. *Geochim. Cosmochim. Acta*, 65:3055–3063, 2001.

[56] H. Churchill, H. Teng, and R.M. Hazen. Correlation of pH-dependent surface interaction forces to amino acid adsorption: Implications for the origin of life. *Am. Mineral.*, 89:1048–1055, 2004.

[57] C.Z. Na and S.T. Martin. Interfacial forces are modified by the growth of surface nanostructures. *Environ. Sci. Technol.*, 42:6883–6889, 2008.

[58] M. Valtiner, S. Borodin, and G. Grundmeier. Stabilization and Acidic Dissolution Mechanism of Single-Crystalline ZnO(0001) Surfaces in Electrolytes Studied by In-Situ AFM Imaging and Ex-Situ LEED. *Langmuir*, 24:5350–5358, 2008.

[59] S. Ardizzone and S. Trasatti. Interfacial properties of oxides with technological impact in electrochemistry. *Adv. Colloid Interface Sci.*, 64:173–251, 1996.

[60] W. M. Haynes and D. R. Lide (ed.). *CRC Handbook of Chemistry and Physics*. CRC Press, Florida, 91 edition, 20010–2011.

[61] R. de Levie. The electrolysis of water. *J. Electroanal. Chem.*, 476:92—93, 1999.

[62] R.L. LeRoy. Industrial water electrolysis: Present and future. *International Journal of Hydrogen Energy*, 8(6):401–417, 1983.

[63] P. Häussinger, R. Lohmüller, and A. M. Watson. Hydrogen. In M. Bohnet, editor, *Ullmann's Encyclopedia of Industrial Chemistry*, volume 17, pages 85–240. Wiley-VCH Verlang GmbH & Co. KGaA, Weinheim, 7th edition, 2003.

[64] J.O. Bockris. Kinetics of Activation Controlled Consecutive Electrochemical Reactions: Anodic Evolution of Oxygen. *J. Chem. Phys.*, 24:817–827, 1956.

[65] Y. Matsumoto and E. Sato. Electrocatalytic properties of transition metal oxides for oxygen evolution reaction. *Mater. Chem. Phys.*, 14:397–426, 1986.

[66] G. Aylward and T. Findlay. *SI Chemical Data*. John Wiley & Sons Australia, Ltd, Milton, 1998.

[67] T. Oi and Y. Sakaki. Optimum hydrogen generation capacity and current density of the PEM-type water electrolyzer operated only during the off-peak period of electricity demand. *J. Power Sources*, 129:229–237, 2004.

[68] R.L. LeRoy, C.T. Bowen, and D.J. LeRoy. The Thermodynamics of Aqueous Water Electrolysis. *J. Electrochem. Soc.*, 127:1954–1962, 1980.

[69] R.L. LeRoy. Hydrogen Production by the Electrolysis of Water. *J. Electrochem. Soc.*, 130:2158–2163, 1983.

[70] B. V. Tilak, P. W. T. Lu, J. E. Colman, and S. Srinivasan. Electrolytic production of hydrogen. In J. O'M. Bockris, B. E. Conway, E. Yeager, and R. E. White, editors, *Comprehensive Treaties of Electrochemistry*, volume 2, pages 1–104. Plenum Press, New York and London, 1981.

[71] K. Zeng and D. Zhang. Recent progress in alkaline water electrolysis for hydrogen production and applications. *Prog. Energy Combust. Sci.*, 36:307–326, 2010.

[72] S.A. Grigoriev, V.I. Porembsky, and V.N. Fateev. Pure hydrogen production by PEM electrolysis for hydrogen energy. *Int. J. Hydrogen Energy*, 31:171–175, 2006.

[73] H. Takenaka, E. Torikai, Y. Kawami, and N. Wakabayashi. Solid polymer electrolyte water electrolysis. *Int. J. Hydrogen Energy*, 7:397–403, 1982.

[74] P. Millet, M. Pineri, and R. Durand. New solid polymer electrolyte composites for water electrolysis. *J. Appl. Electrochem.*, 19:162–166, 1989.

[75] P. Millet, R. Durand, and M. Pineri. Preparation of new solid polymer electrolyte composites for water electrolysis. *Int. J. Hydrogen Energy*, 15:245–253, 1990.

[76] K. Petrov, K.E. Xiao, E.R. Gonzalez, S. Srinivasan, A.J. Appleby, and O.J. Murphy. An advanced proton exchange membrane electrolyzer with an improved three-dimensional reaction zone. *Int. J. Hydrogen Energy*, 18:907–913, 1993.

[77] P. Millet, T. Alleau, and R. Durand. Characterization of membrane-electrode assemblies for solid polymer electrolyte water electrolysis. *J. Appl. Electrochem.*, 23:322–331, 1993.

[78] F. Andolfatto, R. Durand, A. Michas, P. Millet, and P. Stevens. Solid polymer electrolyte water electrolysis: Electrocatalysis and long-term stability. *Int. J. Hydrogen Energy*, 19:421–427, 1994.

[79] P. Millet, F. Andolfatto, and R. Durand. Design and performance of a solid polymer electrolyte water electrolyzer. *Int. J. Hydrogen Energy*, 21:87–93, 1996.

[80] P. Millet, D. Dragoe, S. Grigoriev, V. Fateev, and C. Etievant. GenHyPEM: A research program on PEM water electrolysis supported by the European Commission. *Int. J. Hydrogen Energy*, 34:4974–4982, 2009.

[81] S. Siracusano, V. Baglio, A. Di Blasi, N. Briguglio, A. Stassi, R. Ornelas, E. Trifoni, V. Antonucci, and A.S. Aricò. Electrochemical characterization of single cell and short stack PEM electrolyzers based on a nanosized IrO_2 anode electrocatalyst. *Int. J. Hydrogen Energy*, 35(11):5558–5568, 2010.

[82] A. Marshall, B. Børresen, G. Hagen, M. Tsypkin, and R. Tunold. Hydrogen production by advanced proton exchange membrane (PEM) water electrolysers—Reduced energy consumption by improved electrocatalysis. *Energy*, 32:431–436, 2007.

[83] A.C.C. Tseung and S. Jasem. Oxygen evolution on semiconducting oxides. *Electrochim. Acta*, 22:31–34, 1977.

[84] S. Trasatti. Work function, electronegativity, and electrochemical behaviour of metals: III. Electrolytic hydrogen evolution in acid solutions. *J. Electroanal. Chem.*, 39:163–184, 1972.

[85] S. Trasatti. Electrocatalysis in the anodic evolution of oxygen and chlorine. *Electrochim. Acta*, 29:1503–1512, 1984.

[86] J. Rossmeisl, Z.-W. Qu, H. Zhu, G.-J. Kroes, and J.K. Nørskov. Electrolysis of water on oxide surfaces. *J. Electroanal. Chem.*, 607:83–89, 2007.

[87] J. Rossmeisl, K. Dimitrievski, P. Siegbahn, and J.K. Nørskov. Comparing electrochemical and biological water splitting. *J. Phys. Chem. C*, 111:18821–18823, 2007.

[88] J.I. Martinez, H.A. Hansen, J. Rossmeisl, and J.K. Nørskov. Formation energies of rutile metal dioxides using density functional theory. *Phys. Rev. B: Condens. Matter Mater. Phys.*, 79:045120–5, 2009.

[89] H.A. Hansen, I.C. Man, F. Studt, F. Abild-Pedersen, T. Bligaard, and J. Rossmeisl. Electrochemical chlorine evolution at rutile oxide (110) surfaces. *Phys. Chem. Chem. Phys.*, 12:283–290, 2010.

[90] P. Rasiyah and A.C.C. Tseung. The Role of the Lower Metal Oxide/Higher Metal Oxide Couple in Oxygen Evolution Reactions. *J. Electrochem. Soc.*, 133:803–808, 1984.

[91] A. Daghetti, G. Lodi, and S. Trasatti. Interfacial properties of oxides used as anodes in the electrochemical technology. *Mater. Chem. Phys.*, 8:1–90, 1983.

[92] S. Trasatti. Oxide/aqueous solution interfaces, interplay of surface chemistry and electrocatalysis. *Mater. Chem. Phys.*, 16:157–174, 1987.

[93] L.A. De Faria, M. Prestat, J.-F. Koenig, P. Chartier, and S. Trasatti. Surface properties of Ni+Co mixed oxides: a study by X-rays, XPS, BET and PZC. *Electrochim. Acta*, 44:1481–1489, 1998.

[94] L.A. De Faria and S. Trasatti. Physical versus chemical mixtures of oxides: the point of zero charge of Ni+Co mixed oxides. *J. Electroanal. Chem.*, 554-555:355–359, 2003.

[95] F. Beck. Wear mechanisms of anodes. *Electrochim. Acta*, 34:811–822, 1989.

[96] G.N. Martelli, R. Ornelas, and G. Faita. Deactivation mechanisms of oxygen-evolving anodes at high-current densities. *Electrochim. Acta*, 39:1551–1558, 1994.

[97] J.D. Holladay, J. Hu, D.L. King, and Y. Wang. An overview of hydrogen production technologies. *Catal. Today*, 139:244–260, 2009.

[98] W. Böld and M. Breiter. Untersuchung des anodischen aufbaus und der kathodischen reduktion der sauerstoffbelegung am rhodium und iridium. *Electrochim. Acta*, 5:169–179, 1961.

[99] A. Capon and R. Parsons. The effect of strong acid on the reactions of hydrogen and oxygen on the noble metals. A study using cyclic voltammetry and a new teflon electrode holder. *J. Electroanal. Chem.*, 39:275–286, 1972.

[100] D.A.J. Rand and R. Woods. Cyclic voltammetric studies on iridium electrodes in sulphuric acid solutions: Nature of oxygen layer and metal dissolution. *J. Electroanal. Chem.*, 55:375–381, 1974.

[101] J.M. Otten and W. Visscher. The anodic behaviour of iridium: I. The effect of potential cycling. *J. Electroanal. Chem.*, 55:1–11, 1974.

[102] J.M. Otten and W. Visscher. The anodic behaviour of iridium: II. The oxygen coverage. *J. Electroanal. Chem.*, 55:13–21, 1974.

[103] D.N. Buckley and L.D. Burke. The Oxygen electrode Part 5.— Enhancement of Charge Capacity of an Iridium Surface in the Anodic Region. *J. Chem. Soc. Faraday Trans. 1*, 71:1447–1459, 1975.

[104] P.G. Pickup and V.I. Birss. A model for anodic hydrous oxide growth at iridium. *J. Electroanal. Chem.*, 220:83–100, 1987.

[105] V. Birss, R. Myers, H. Angerstein-Kozlowska, and B.E. Conway. Electron Microscopy Study of Formation of Thick Oxide Films on Ir and Ru Electrodes. *J. Electrochem. Soc.*, 131:1502–1510, 1984.

[106] E.J. Frazer and R. Woods. The oxygen evolution reaction on cycled iridium electrodes. *J. Electroanal. Chem.*, 102:127–130, 1979.

[107] P.G. Pickup and V.I. Birss. The Influence of the Aqueous Growth Medium on the Growth Rate, Composition, and Structure of Hydrous Iridium Oxide Films. *J. Electrochem. Soc.*, 135:126–133, 1988.

[108] I.T.E. Fonseca, M.I. Lopes, and M.T.C. Portela. A comparative voltammetric study of the Ir|H_2SO_4 and Ir|$HClO_4$ aqueous interfaces. *J. Electroanal. Chem.*, 415:89–96, 1996.

[109] J. Mozota and B.E. Conway. Surface and bulk processes at oxidized iridium electrodes—I. Monolayer stage and transition to reversible multilayer oxide film behaviour. *Electrochim. Acta*, 28:1–8, 1983.

[110] B.E. Conway and J. Mozota. Surface and bulk processes at oxidized iridium electrodes—II. Conductivity-switched behaviour of thick oxide films. *Electrochim. Acta*, 28:9–16, 1983.

[111] E.R. Kötz and H. Neff. Anodic iridium oxide films: An UPS study of emersed electrodes. *Surf. Sci.*, 160:517–530, 1985.

[112] R. Kötz. Ultraviolet photoelectron spectroscopy (UPS) of anodic oxide films on Au, Pt, Ru and $Ru_{0.5}Ir_{0.5}$ alloy. *Surf. Sci.*, 47:109–114, 1991.

[113] L.D. Burke, J.K. Mulcahy, and D.P. Whelan. Preparation of an oxidized iridium electrode and the variation of its potential with pH. *J. Electroanal. Chem.*, 163:117–128, 1984.

[114] P.G. Pickup and V.I. Birss. Chemical analysis of the ionic content of hydrous iridium oxide films. *J. Electroanal. Chem.*, 240:171–183, 1988.

[115] J. Mozota and B.E. Conway. Modification of Apparent Electrocatalysis for Anodic Chlorine Evolution on Electrochemically Conditioned Oxide Films at Iridium Anodes. *J. Electrochem. Soc.*, 128:2142–2149, 1981.

[116] C. Bock. *A Kinetic, Structural and Compositional Study of Electrochemically Formed Hydrous Ir Oxide Films.* PhD thesis, University of Calgary, 1997.

[117] C. Bock and V.I. Birss. Comparison of Ir oxide film redox kinetics in sulfuric and p-toluene sulfonic acid solutions. *Electrochim. Acta*, 46:837–849, 2001.

[118] L.D. Burke and R.A. Scannell. An investigation of hydrous oxide growth on iridium in base. *J. Electroanal. Chem.*, 175:119–141, 1984.

[119] A. Kapałka, S. Fierro, Z. Frontistis, A. Katsaounis, O. Frey, M. Koudelka, C. Comninellis, and K.M. Udert. Electrochemical behaviour of ammonia (NH_4^+/NH_3) on electrochemically grown anodic iridium oxide film (AIROF) electrode. *Electrochem. Commun.*, 11:1590–1592, 2009.

[120] C. Bock and V.I. Birss. Irreversible Decrease of Ir Oxide Film Redox Kinetics. *J. Electrochem. Soc.*, 146:1766–1772, 1999.

[121] H. Elzanowska and V.I. Birss. Reversible ageing of iridium oxide electrodes in acidic solutions. *J. Appl. Electrochem.*, 23:646–654, 1993.

[122] J.D.E. McIntyre, W.F. Peck Jr, and S. Nakahara. Oxidation State Changes and Structure of Electrochromic Iridium Oxide Films. *J. Electrochem. Soc.*, 127:1264–1268, 1980.

[123] S. Gottesfeld and S. Srinivasan. Electrochemical and optical studies of thick oxide layers on iridium and their electrocatalytic activities for the oxygen evolution reaction. *J. Electroanal. Chem.*, 86:89–104, 1978.

[124] D. Michell, D.A.J. Rand, and R. Woods. Analysis of the anodic oxygen layer on iridium by X-ray emission, electron diffraction and electron microscopy. *J. Electroanal. Chem.*, 84:117–126, 1977.

[125] H. Elzanowska, E. Miasek, and V.I. Birsss. Electrochemical formation of Ir oxide/polyaniline composite films. *Electrochim. Acta*, 53:2706–2715, 2008.

[126] I. Lee, C. Whang, Y. Lee, G. Hwan Lee, B. Park, J. Park, W. Seo, and F. Cui. Formation of nano iridium oxide: material properties and neural cell culture. *Thin Solid Films*, 475:332–336, 2005.

[127] J.D.E. McIntyre, S. Basu, W.F.J. Peck, W.L. Brown, and W.A. Augustyniak. Cation insertion reactions of electrochromic tungsten and iridium oxide films. *Phys. Rev. B*, 25:7242–7254, 1982.

[128] M.F. Yuen, I. Lauks, and W.C. Dautremont-Smith. pH dependent voltammetry of iridium oxide films. *Solid State Ionics*, 11:19–29, 1983.

[129] S.H. Glarum and J.H. Marshall. The A-C Responce of Iridium Oxide Films. *J. Electrochem. Soc.*, 127:1467–1474, 1980.

[130] D. Čukman and M. Vuković. Electrochemical behaviour of an electrodeposited iridium electrode in acid solution. *J. Electroanal. Chem.*, 279:283–290, 1990.

[131] M. Vuković. Voltammetric and galvanostatic studies of hydrous and anhydrous iridium oxide films. *J. Appl. Electrochem.*, 20:969–973, 1990.

[132] P.G. Pickup and V.I. Birss. The kinetics of charging and discharging of iridium oxide films in aqueous and non-aqueous media. *J. Electroanal. Chem.*, 240:185–199, 1988.

[133] B. Aurian-Blajeni, X. Beebe, R.D. Rauh, and T.L. Rose. Impedance of hydrated iridium oxide electrodes. *Electrochim. Acta*, 34:795–802, 1989.

[134] L. Sziráki and L. Bóbics. Impedance study of electrochromism in anodic Ir oxide films. *Electrochim. Acta*, 47:2189–2197, 2002.

[135] M. Huppauff and B. Lengeler. Valency and Structure of Iridium in Anodic Iridium Oxide Films. *J. Electrochem. Soc.*, 140:598–602, 1993.

[136] M.S. Cruz, T.F. Otero, and S.U. Za nartu. Effect of temperature on the potentiodynamic behaviour of iridium in 0.5 M H_2SO_4. *J. Electroanal. Chem.*, 158:375–381, 1983.

[137] P.G. Pickup and V.I. Birss. The Electrochemistry of Iridium Oxide Films in Some Nonaqueous Solvents. *J. Electrochem. Soc.*, 135:41–45, 1988.

[138] H. Elzanowska, J. Segal, and V.I. Birss. Complications associated with kinetic studies of hydrous Ir oxide films. *Electrochim. Acta*, 44:4515–4524, 1999.

[139] S. Gottesfeld, A. Redondo, I. Rubinstein, and S.W. Feldberg. Resistance-induced peaks in cyclic voltammograms of systems that can be switched electrochemically between an insulating and conductive state. *J. Electroanal. Chem.*, 265:15–22, 1989.

[140] S. Gottesfeld. Faradaic Processes at the Ir/Ir Oxide Electrode. *J. Electrochem. Soc.*, 127:1922–1925, 1980.

[141] T.M. Silva, A.M.P. Simoes, M.G.S. Ferreira, M. Walls, and M.D. Belo. Electronic structure of iridium oxide films formed in neutral phosphate buffer solution. *J. Electroanal. Chem.*, 441:5–12, 1998.

[142] F. Fievet, J.P. Lagier, B. Blin, B. Beaudoin, and M. Figlarz. Homogeneous and heterogeneous nucleations in the polyol process for the preparation of micron and submicron size metal particles. *Solid State Ionics*, 32-33:198–205, 1989.

[143] A. Marshall, B. Borresen, G. Hagen, M. Tsypkin, and R. Tunold. Preparation and characterisation of nanocrystalline $Ir_xSn_{1-x}O_2$ electrocatalytic powders. *Mater. Chem. Phys.*, 94:226–232, 2005.

[144] A. Marshall, B. Børresen, G. Hagen, M. Tsypkin, and R. Tunold. Electrochemical characterisation of $Ir_xSn_{1-x}O_2$ powders as oxygen evolution electrocatalysts. *Electrochim. Acta*, 51:3161–3167, 2006.

[145] A. Marshall, B. Børresen, G. Hagen, S. Sunde, M. Tsypkin, and R. Tunold. Iridium oxide-based nanocrystalline particles as oxygen evolution electrocatalysts. *Russ. J. Electrochem.*, 42:1134—1140, 2006.

[146] A.T. Marshall, S. Sunde, M. Tsypkin, and R. Tunold. Performance of a PEM water electrolysis cell using $Ir_xRu_yTa_zO_2$ electrocatalysts for the oxygen evolution electrode. *Int. J. Hydrogen Energy*, 32:2320–2324, 2007.

[147] Y. Murakami, S. Tsuchiya, K. Yahikozawa, and Y. Takasu. Preparation of ultrafine IrO_2–Ta_2O_5 binary oxide particles by a sol-gel process. *Electrochim. Acta*, 39:651–654, 1994.

[148] Y. Takasu, S. Onoue, K. Kameyama, Y. Murakami, and K. Yahikozawa. Preparation of ultrafine RuO_2–IrO_2–TiO_2 oxide particles by a sol–gel process. *Electrochim. Acta*, 39:1993–1997, 1994.

[149] S. Ardizzone, C.L. Bianchi, G. Cappelletti, M. Ionita, A. Minguzzi, S. Rondinini, and A. Vertova. Composite ternary SnO_2-IrO_2-Ta_2O_5 oxide electrocatalysts. *J. Electroanal. Chem.*, 589(1):160–166, 2006.

[150] R. Adams and R.L. Shriner. Platinum oxide as a catalyst in the reduction of organic compounds. III. Preparation and properties of the oxide of platinum obtained by the fusion of chloroplatinic acid with sodium nitrate. *J. Am. Chem. Soc.*, 45:2171–2179, 1923.

[151] W.F. Bruce. The Preparation of Platinum Oxide for Catalytic Hydrogenations. *J. Am. Chem. Soc.*, 58:687–688, 1936.

[152] L.K. Kurihara, G.M. Chow, and P.E. Schoen. Nanocrystalline metallic powders and films produced by the polyol method. *Nanostructured Matererials*, 5:607–613, 1995.

[153] F. Bonet, V. Delmas, S. Grugeon, R. Herrera Urbina, P. Silvert, and K. Tekaia-Elhsissen. Synthesis of monodisperse Au, Pt, Pd, Ru and Ir nanoparticles in ethylene glycol. *Nanostruct. Mater.*, 11:1277–1284, 1999.

[154] R. Harpeness, Z. Peng, X. Liu, V.G. Pol, Y. Koltypin, and A. Gedanken. Controlling the agglomeration of anisotropic Ru nanoparticles by the microwave-polyol process. *J. Colloid Interface Sci.*, 287:678–684, 2005.

[155] Y. Murakami, H. Ohkawauchi, M. Ito, K. Yahikozawa, and Y. Takasu. Preparations of ultrafine IrO_2–SnO_2 binary oxide particles by a sol-gel process. *Electrochim. Acta*, 39:2551–2554, 1994.

[156] R. Hutchings, K. Müller, R. Kötz, and S. Stucki. A structural investigation of stabilized oxygen evolution catalysts. *J. Mater. Sci.*, 19:3987–3994, 1984.

[157] E. Rasten. *Electrocatalysts in Water Electrolysis with Solid Polymer Electrolyte*. PhD thesis, Norwegian University of Science and Technology, 2001.

[158] E. Rasten, G. Hagen, and R. Tunold. Electrocatalysis in water electrolysis with solid polymer electrolyte. *Electrochim. Acta*, 48:3945–3952, 2003.

[159] A.C.C. Tseung and S.C. Dhara. Loss of surface area by platinum and supported platinum black electrocatalyst. *Electrochim. Acta*, 20:681–683, 1975.

[160] A.T. Marshall and R.G. Haverkamp. Electrocatalytic activity of IrO_2-RuO_2 supported on Sb-doped SnO_2 nanoparticles. *Electrochim. Acta*, 55:1978–1984, 2010.

[161] S. Ferro and A. De Battisti. Electrocatalysis and Chlorine Evolution Reaction at Ruthenium Dioxide Deposited on Conductive Diamond. *J. Phys. Chem. B*, 106:2249–2254, 2002.

[162] G. Siné, I. Duo, B. Roustom, G. Fóti, and C. Comninellis. Deposition of clusters and nanoparticles onto boron-doped diamond electrodes for electrocatalysis. *J. Appl. Electrochem.*, 36:847—862, 2006.

[163] E. Slavcheva, V. Nikolova, T. Petkova, E. Lefterova, I. Dragieva, T. Vitanov, and E. Budevski. Electrocatalytic activity of Pt and PtCo deposited on Ebonex by BH reduction. *Electrochim. Acta*, 50:5444–5448, 2005.

[164] L. Ma, S. Sui, and Y. Zhai. Preparation and characterization of Ir/TiC catalyst for oxygen evolution. *J. Power Sources*, 177:470–477, 2008.

[165] O.E. Haas, S.T. Briskeby, O.E. Kongstein, M. Tsypkin, R. Tunold, and B.T. Børresen. Synthesis and characterisation of $Ru_xTi_{x-1}O_2$ as a catalyst support for polymer electrolyte fuel cell. *J. New Mater. Electrochem. Syst.*, 11:9–14, 2008.

[166] S.M.A. Shibli and V.S. Dilimon. Development of TiO_2-supported nano-RuO_2-incorporated catalytic nickel coating for hydrogen evolution reaction. *Int. J. Hydrogen Energy*, 33:1104–1111, 2008.

[167] J.B. Goodenough. Metallic oxides. *Prog. Solid State Chem.*, 5:145–399, 1971.

[168] J. M. Honig. Electronic band structure of oxides with metallic or semiconducting characteristics. In Sergio Trasatti, editor, *Electrodes of Conductive Metallic Oxides A*, pages 1–96. Elsevier, Amsterdam, 1980.

[169] R. Kötz and S. Stucki. Stabilization of RuO_2 by IrO_2 for anodic oxygen evolution in acid media. *Electrochim. Acta*, 31:1311–1316, 1986.

[170] E.N. Balko and C.R. Davidson. Solid solutions of RuO_2 and IrO_2. *J. Inorg. Nucl. Chem.*, 42:1778–1781, 1980.

[171] Y. Murakami, K. Miwa, M. Ueno, M. Itoand K. Yahikozawa, and Y. Takasu. Morphology of ultrafine RuO_2–IrO_2 binary oxide particles prepared by a sol-gel process. *J. Electrochem. Soc.*, 141(9):L118–L120, September 1994.

[172] A. Marshall. *Electrocatalysts for the Oxygen Evolution Electrode in Water Electrolysers using Proton Exchange Membranes: Synthesis and Characterisation.* PhD thesis, Norwegian University of Science and Technology, 2005.

[173] T. Arikawa, Y. Takasu, Y. Murakami, K. Asakura, and Y. Iwasawa. Characterization of the Structure of RuO_2–IrO_2/Ti Electrodes by EXAFS. *J. Phys. Chem. B*, 102:3736–3741, 1998.

[174] Rhys Forgie, Greg Bugosh, K. C. Neyerlin, Zengcai Liu, and Peter Strasser. Bimetallic Ru Electrocatalysts for the OER and Electrolytic Water Splitting in Acidic Media. *Electrochem. Solid-State Lett.*, 13(4):B36–B39, 2010.

[175] I. C. Man. *Theoretical study of electro-catalysts for oxygen evolution.* PhD thesis, Technical University of Denmark, 2011.

[176] D. J. Mowbray, J. I. Martinez, F. Calle-Vallejo, J. Rossmeisl, K. S. Thygesen, K. W. Jacobsen, and J. K. Nørskov. Trends in metal oxide stability for nanorods, nanotubes, and surfaces. *The Journal of Physical Chemistry C*, 115(5):2244–2252, 2011.

[177] C. Angelinetta, S. Trasatti, L.D. Atanasoska, and R.T. Atanasoski. Surface properties of RuO_2 + IrO_2 mixed oxide electrodes. *J. Electroanal. Chem.*, 214:535–546, 1986.

[178] C. Angelinetta, S. Trasatti, L.D. Atanasoka, Z.S. Minevski, and R.T. Atanasoski. Effect of preparation on the surface and electrocatalytic properties of RuO_2 + IrO_2 mixed oxide electrodes. *Mater. Chem. Phys.*, 22:231–247, 1989.

[179] K. Macounova, I. Jirka, A. Trojanek, M. Makarova, Z. Samec, and P. Krtil. Electrochemical Behavior of Nanocrystalline $Ru_{0.8}Me_{0.2}O_{2-x}$ (Me = Fe, Co, Ni) Oxide Electrodes in Double-Layer Region. *J. Electrochem. Soc.*, 154:A1077–A1082, 2007.

[180] A. Marshall, M. Tsypkin, B. Børresen, G. Hagen, and R. Tunold. Nanocrystalline $Ir_xSn_{(1-x)}O_2$ electrocatalysts for oxygen evolution in water electrolysis with polymer electrolyte—Effect of heat treatment. *J. New Mater. Electrochem. Syst.*, 7:197–204, 2004.

[181] A. E. Newkirk and D. W. McKee. Thermal decomposition of rhodium, iridium, and ruthenium chlorides. *J. Catal.*, 11(4):370–377, 1968.

[182] C. Hu and K. Chang. Cyclic voltammetric deposition of hydrous ruthenium oxide for electrochemical supercapacitors: effects of the chloride precursor transformation. *J. Power Sources*, 112:401–409, 2002.

[183] C. Hu, Y. Huang, and K. Chang. Annealing effects on the physicochemical characteristics of hydrous ruthenium and ruthenium-iridium oxides for electrochemical supercapacitors. *J. Power Sources*, 108:117–127, 2002.

[184] R. G. Haverkamp, A. T. Marshall, and B. C. C. Cowie. Energy resolved XPS depth profile of (IrO_2, RuO_2, Sb_2O_5, SnO_2) electrocatalyst powder to reveal core-shell nanoparticle structure. *Surf. Interface Anal.*, 2010.

[185] M. Rubel, R. Haasch, P. Mrozek, A. Wieckowski, C. De Pauli, and S. Trasatti. Characterization of IrO_2-SnO_2 thin-layers by electron and ion spectroscopies. *Vacuum*, 45(4):423–427, 1994.

[186] J. Jirkovsky, H. Hoffmannova, M. Klementova, and P. Krtil. Particle Size Dependence of the Electrocatalytic Activity of Nanocrystalline RuO_2 Electrodes. *J. Electrochem. Soc.*, 153:E111–E118, 2006.

[187] L. Ouattara, S. Fierro, O. Frey, M. Koudelka, and C. Comninellis. Electrochemical comparison of IrO_2 prepared by anodic oxidation of pure iridium and IrO_2 prepared by thermal decomposition of H_2IrCl_6 precursor solution. *J. Appl. Electrochem.*, 39:1361–1367, 2009.

[188] S. Sunde, I. A. Lervik, M. Tsypkin, and L.-E. Owe. Impedance analysis of nano-structured iridium oxide electrocatalysts. *Electrochim. Acta*, 55:7751–7760, 2010.

[189] H. Beer. Improvements in or relating to electrodes for electrolysis. British Patent 1,147,442, 1969.

[190] V. de Nora and J.-W. K. von Burgsdorff. Der Beitrag der dimensionsstabilen Anoden (DSA) zur Chlor-Technologie. *Chem. Ing. Tech.*, 47:125–128, 1975.

[191] Sergio Trasatti. Interfacial electrochemistry of conductive oxides for electrocatalysis. In Andrezej Wieckowski, editor, *Interfacial Electrochemistry*, pages 769–792. Marcel Dekker, Inc, New York, 1999.

[192] K. Kameyama, K. Tsukada, K. Yahikozawa, and Y. Takasu. Surface Characterization of RuO_2–IrO_2–TiO_2 Coated Titanium Electrodes. *J. Electrochem. Soc.*, 141:643–647, 1994.

[193] Ch. Comninellis and G. P. Vercesi. Characterization of DSA-type oxygen evolving electrodes: Choice of a coating. *Journal of Applied Electrochemistry*, 21(4):335–345, 1991.

[194] R. Mráz and J. Krýsa. Long service life IrO_2/Ta_2O_5 electrodes for electroflotation. *J. Appl. Electrochem.*, 24:1262–1266, 1994.

[195] A. J. Terezo, J. Bisquert, E. C. Pereira, and G. Garcia-Belmonte. Separation of transport, charge storage and reaction processes of porous electrocatalytic IrO_2 and IrO_2/Nb_2O_5 electrodes. *Journal of Electroanalytical Chemistry*, 508(1-2):59–69, 2001.

[196] E. N. Balko and P. H. Nguyen. Iridium-tin mixed oxide anode coatings. *Journal of Applied Electrochemistry*, 21(8):678–682, 1991.

[197] X. Chen and G. Chen. Investigation of Ti/IrO_2-Sb_2O_5-SnO_2 Electrodes for O_2 Evolution. *J. Electrochem. Soc.*, 152:J59–J64, 2005.

[198] T.W. Chao, C.J. Liu, A.H. Hsieh, H.M. Chang, Y.S. Huang, and D.S. Tsai. Quartz crystal microbalance sensor based on nano structured IrO_2. *Sens. Actuators, B*, 122:95–100, 2007.

[199] E. Slavcheva, I. Radev, G. Topalov, and E. Budevski. Sputtered electrocatalysts for PEM electrochemical energy converters. *Electrochim. Acta*, 53:362–368, 2007.

[200] E. Slavcheva, I. Radev, S. Bliznakov, G. Topalov, P. Andreev, and E. Budevski. Sputtered iridium oxide films as electrocatalysts for water splitting via PEM electrolysis. *Electrochim. Acta*, 52:3889–3894, 2007.

[201] B. Wessling, A. Besmehn, W. Mokwa, and U. Schnakenberg. Reactively Sputtered Iridium Oxide. *J. Electrochem. Soc.*, 154:F83–F89, 2007.

[202] B. Wessling, W. Mokwa, and U. Schnakenberg. Sputtered Ir Films Evaluated for Electrochemical Performance I. Experimental Results. *J. Electrochem. Soc.*, 155:F61–F65, 2008.

[203] B. Wessling, D. Lusebrink, W. Mokwa, and U. Schnakenberg. Sputtered Ir Films Evaluated for Electrochemical Performance II. Simulations. *J. Electrochem. Soc.*, 155:F66–F74, 2008.

[204] T. Pauporté, D. Aberdam, J. Hazemann, R. Faure, and R. Durand. X-ray absorption in relation to valency of iridium in sputtered iridium oxide films. *J. Electroanal. Chem.*, 465:88–95, 1999.

[205] J. Backholm, P. Georen, and G.A. Niklasson. Determination of solid phase chemical diffusion coefficient and density of states by electrochemical methods: Application to iridium oxide-based thin films. *J. Appl. Phys.*, 103:023702–10, 2008.

[206] T. Jones. Iridium plating. *Met. Finish.*, 102:87–103, 2004.

[207] T. Ohsaka, M. Isaka, K. Hirano, and T. Ohishi. Effect of ultrasound sonication on electroplating of iridium. *Ultrason. Sonochem.*, 15:283–288, 2008.

[208] Y.J. Chen, P.L. Taylor, and D. Scherson. Electrochemical and In Situ Optical Studies of Supported Iridium Oxide Films in Aqueous Solutions. *J. Electrochem. Soc.*, 156:F14–F21, 2009.

[209] S.C. Mailley, M. Hyland, P. Mailley, J.M. McLaughlin, and E.T. McAdams. Electrochemical and structural characterizations of electrodeposited iridium oxide thin-film electrodes applied to neurostimulating electrical signal. *Mater. Sci. Eng., C*, 21:167–175, 2002.

[210] J. Hu, M. Abdelsalam, P. Bartlett, R. Cole, Y. Sugawara, J. Baumberg, S. Mahajan, and G. Denuault. Electrodeposition of highly ordered macroporous iridium oxide through self-assembled colloidal templates. *J. Mater. Chem.*, 19:3855–3858, 2009.

[211] V.I. Birss, H. Andreas, I. Serebrennikova, and H. Elzanowska. Electrochemical Characterization of Sol-Gel Formed Ir Metal Nanoparticles. *Electrochem. Solid-State Lett.*, 2:326–329, 1999.

[212] H. Andreas, H. Elzanowska, I. Serebrennikova, and V. Birss. Hydrous Ir oxide film properties at sol-gel derived Ir nanoparticles. *J. Electrochem. Soc.*, 147:4598–4604, 2000.

[213] T. Pauporté, F. Andolfatto, and R. Durand. Some electrocatalytic properties of anodic iridium oxide nanoparticles in acidic solution. *Electrochim. Acta*, 45:431–439, 1999.

[214] R. de Levie. On porous electrodes in electrolyte solutions: I. Capacitance effects. *Electrochim. Acta*, 8:751–780, 1963.

[215] R. de Levie. On porous electrodes in electrolyte solutions—IV. *Electrochim. Acta*, 9:1231–1245, 1964.

[216] J. Euler and W. Nonnenmacher. Stromverteilung in porósen elektroden. *Electrochim. Acta*, 2:268–286, 1960.

[217] J.S. Newman and C.W. Tobias. Theoretical Analysis of Current Distribution in Porous Electrodes. *J. Electrochem. Soc.*, 109:1183–1191, 1962.

[218] M.L. Perry, J. Newman, and E.J. Cairns. Mass Transport in Gas-Diffusion Electrodes: A Diagnostic Tool for Fuel-Cell Cathodes. *J. Electrochem. Soc.*, 145:5–15, 1998.

[219] L.O. Valøen, S. Sunde, and R. Tunold. An impedance model for electrode processes in metal hydride electrodes. *J. Alloys Compd.*, 253-254:656–659, 1997.

[220] J.P. Meyers, M. Doyle, R.M. Darling, and J. Newman. The Impedance Response of a Porous Electrode Composed of Intercalation Particles. *J. Electrochem. Soc.*, 147:2930–2940, 2000.

[221] A.M. Svensson, L.O. Valøen, and R. Tunold. Modeling of the impedance response of porous metal hydride electrodes. *Electrochim. Acta*, 50:2647–2653, 2005.

[222] G. Sikha and R.E. White. Analytical Expression for the Impedance Response of an Insertion Electrode Cell. *J. Electrochem. Soc.*, 154:A43–A54, 2007.

[223] V. Srinivasan and J. Newman. Discharge Model for the Lithium Iron-Phosphate Electrode. *J. Electrochem. Soc.*, 151:A1517–A1529, 2004.

[224] R.W.J.M. Huang, F. Chung, and E.M. Kelder. Impedance Simulation of a Li-Ion Battery with Porous Electrodes and Spherical Li^+ Intercalation Particles. *J. Electrochem. Soc.*, 153:A1459–A1465, 2006.

[225] S. Södergren, A. Hagfeldt, J. Olsson, and S. Lindquist. Theoretical Models for the Action Spectrum and the Current-Voltage Characteristics of Microporous Semiconductor Films in Photoelectrochemical Cells. *J. Phys. Chem.*, 98:5552–5556, 1994.

[226] J. S. Newman. *Electrochemical Systems*, pages 454–472. Prentice Hall, NJ, 2nd edition, 1992.

[227] Laurence D Burke and Michael E. G. Lyons. Electrochemistry of hydrous oxide films. In Ralph E. White, Bockris J. O'M., and B. E. Conway, editors, *Modern Aspects of Electrochemistry*, volume 18, pages 169–248. Plenum Press, New York and London, 1986.

[228] H Rickert. *Solid State Electrochemistry. An Introduction.* Springer, Berlin, Heidelberg, 1982.

[229] J. S. Newman. *Electrochemical Systems*, pages 241–261. Prentice Hall, NJ, 2nd edition, 1992.

[230] S. Sunde. Monte Carlo Simulations of Conductivity of Composite Electrodes for Solid Oxide Fuel Cells. *J. Electrochem. Soc.*, 143:1123–1132, 1996.

[231] T. Jacobsen and K. West. Diffusion impedance in planar, cylindrical and spherical symmetry. *Electrochim. Acta*, 40:255–262, 1995.

[232] I. D. Raistrick, D. R. Franceschetti, and J. R. Macdonald. In E. Barsoukov and J. R. Macdonald, editors, *Impedance Spectroscopy. Theory, Experiment, and Applications*, pages 54–58. John Wiley & Sons, Inc., Hoboken, New Jersey, 2nd edition, 2005.

[233] J. S. Newman. *Electrochemical Systems*, pages 82–84. Prentice Hall, NJ, 2nd edition, 1992.

[234] Wolfgang Schmickler. *Interfacial Electrochemistry*. Oxford University Press, Inc., New York, 1996.

[235] Charles Kittel. *Introduction to solid state physics*. John Wiley & Sons, New York, 6th edition, 1986.

[236] S. Trasatti. Physical electrochemistry of ceramic oxides. *Electrochim. Acta*, 36:225–241, 1991.

[237] S.H. Brewer, D. Wicaksana, J. Maria, A.I. Kingon, and S. Franzen. Investigation of the electrical and optical properties of iridium oxide by reflectance FTIR spectroscopy and density functional theory calculations. *Chem. Phys.*, 313:25–31, 2005.

[238] C. Ho, I.D. Raistrick, and R.A. Huggins. Application of A-C Techniques to the Study of Lithium Diffusion in Tungsten Trioxide Thin Films. *J. Electrochem. Soc.*, 127:343–350, 1980.

[239] G.O. Lauvstad, R. Tunold, and S. Sunde. Electrochemical Oxidation of CO on Pt and Ni Point Electrodes in Contact with an Yttria-Stabilized Zirconia Electrolyte. *J. Electrochem. Soc.*, 149:E497–E505, 2002.

[240] F. La Mantia, J. Vetter, and P. Novák. Impedance spectroscopy on porous materials: A general model and application to graphite electrodes of lithium-ion batteries. *Electrochim. Acta*, 53:4109–4121, 2008.

[241] J. S. Newman. *Electrochemical Systems*, page 88. Prentice Hall, NJ, 2nd edition, 1992.

[242] Neil W. Ashcroft and David N. Mermin. *Solid State Physics*, pages 596–597. Saunders College Publishing, Philadelphia, 1976.

[243] R. D. Meyer, S. E. Cogan, T. H. Nguyen, and R. D. Rauh. Electrodeposited iridium oxide for neural stimulation and recording electrodes. *IEEE Trans Neural Syst Rehabil Eng*, 9(1):2–11, 2001.

[244] Donald R. Franceschetti and J. Ross Macdonald. Small-Signal A-C Response Theory for Electrochromic Thin Films. *J. Electrochem. Soc.*, 129(8):1754–1756, 1982.

[245] Z. Ye, H. Meng, and D. Sun. Electrochemical impedance spectroscopic (EIS) investigation of the oxygen evolution reaction mechanism of $Ti/IrO_2 + MnO_2$ electrodes in 0.5 m H_2SO_4 solution. *J. Electroanal. Chem.*, 621:49–54, 2008.

[246] L. Xu, Y. Xin, and J. Wang. A comparative study on IrO_2–Ta_2O_5 coated titanium electrodes prepared with different methods. *Electrochim. Acta*, 54:1820–1825, 2009.

[247] T.A.F. Lassali, L.M.C. Abeid, L.O.S. Bulhões, and J.F.C. Boodts. Surface Characterization of Thermally Prepared, Ti-Supported, Ir-Based Electrocatalysts Containing Ti and Sn. *J. Electrochem. Soc.*, 144:3348–3354, 1997.

[248] T.A.F. Lassalia, J.F.C. Boodtsb, and L.O.S. Bulhões. Charging processes and electrocatalytic properties of $IrO_2/TiO_2/SnO_2$ oxide films investigated by in situ AC impedance measurements. *Electrochim. Acta*, 44:4203–4216, 1999.

[249] C. P. De Pauli and S. Trasatti. Electrochemical surface characterization of $IrO_2 + SnO_2$ mixed oxide electrocatalysts. *J. Electroanal. Chem.*, 369:161–168, 1995.

[250] C. P. De Pauli and S. Trasatti. Composite materials for electrocatalysis of O_2 evolution: $IrO_2 + SnO_2$ in acid solution. *J. Electroanal. Chem.*, 538–539:145–151, 2002.

[251] R. Memming. *Semiconductor Electrochemistry*. Wiley VCH, Weinheim, 2000.

[252] R. Kötz and S. Stucki. Stabilization of RuO_2 by IrO_2 for anodic oxygen evolution in acid media. *Electrochim. Acta*, 31:1311–1316, 1986.

[253] Y.E. Roginskaya, T.V. Varlamova, M.D. Goldstein, I.D. Belova, B.S. Galyamov, R.R. Shifrina, V.A. Shepelin, and V.N. Fateev. Formation, structure and electrochemical properties of IrO_2–RuO_2 oxide electrodes. *Mater. Chem. Phys.*, 30:101–113, 1991.

[254] I. M. Kodintsev, S. Trasatti, M. Rubel, A. Wieckowski, and N. Kaufher. X-ray Photoelectron Spectroscopy and Electrochemical Surface Characterization of $IrO_2 + RuO_2$ Electrodes. *Langmuir*, 8(1):283–290, 1992.

[255] J. Cheng, H. Zhang, G. Chen, and Y. Zhang. Study of $Ir_xRu_{1-x}O_2$ oxides as anodic electrocatalysts for solid polymer electrolyte water electrolysis. *Electrochimica Acta*, 54(26):6250–6256, 2009.

[256] T.J. Schmidt, H.A. Gasteiger, G.D. Stab, P.M. Urban, D.M. Kolb, and R.J. Behm. Characterization of High-Surface-Area Electrocatalysts Using a Rotating Disk Electrode Configuration. *J. Electrochem. Soc.*, 145:2354–2358, 1998.

[257] C. Hu and K. Chang. Cyclic voltammetric deposition of hydrous ruthenium oxide for electrochemical capacitors: effects of codepositing iridium oxide. *Electrochim. Acta*, 45:2685–2696, 2000.

[258] C. Hu and Y. Huang. Effects of preparation variables on the deposition rate and physicochemical properties of hydrous ruthenium oxide for electrochemical capacitors. *Electrochim. Acta*, 46:3431–3444, 2001.

[259] V.V. Panic, T.R. Vidakovic, A.B. Dekanski, V.B. Miskovic-Stankovic, and B.Z. Nikolic. Capacitive properties of RuO_2-coated titanium electrodes prepared by the alkoxide ink procedure. *J. Electroanal. Chem.*, 609:120–128, 2007.

[260] K. Fukuda, C. Iwakura, and H. Tamura. Effect of the addition of NH4F on anodic behaviors of DSA-type electrodes in H_2SO_4–$(NH_4)_2SO_4$ solutions. *Electrochim. Acta*, 24:367–371, 1979.

[261] M. Herrmann, U. Kaluza, and H.P. Boehm. Über die Chemie der Oberfläche des Titandioxids. IV. Austausch von Hydroxidionen gegen Fluoridionen. *Z. Anorg. Allg. Chem.*, 372:308 –313, 1970.

[262] J. Sanchez and J. Augustynskia. X-ray photoelectron spectroscopic study of the interaction of various anions with the oxide-covered titanium metal. *J. Electroanal. Chem.*, 103:423–426, 1979.

[263] C.M. Wang and T.E. Mallouk. Wide-range tuning of the titanium dioxide flat-band potential by adsorption of fluoride and hydrofluoric acid. *J. Phys. Chem.*, 94:4276–4280, 1990.

[264] P. Zelenay, M.A. Habib, and J.O. Bockris. Adsorption of Trifluoromethane Sulfonic Acid on Pt by FTIR and Radiotracer Methods. *J. Electrochem. Soc.*, 131:2464–2465, 1984.

[265] H. Saffarian, P. Ross, F. Behr, and G. Gard. Electrochemical Properties of Perfluoroalkane Disulfonic $[HSO_3(CF_2)_nSO_3H]$ Acids Relevant to Fuel Cell Technology. *J. Electrochem. Soc.*, 139:2391–2397, 1992.

[266] J. Kuta and E. Yeager. The influence of cations on the electrode kinetics of ferricyanide-ferrocyanide system on the rotating gold electrode. *J. Electroanal. Chem.*, 59:110–112, 1975.

[267] L.M. Peter, W. Dürr, P. Bindra, and H. Gerischer. The influence of alkali metal cations on the rate of the $Fe(CN)_6^{4-}/Fe(CN)_6^{3-}$ electrode process. *J. Electroanal. Chem.*, 71:31–50, 1976.

[268] E.L. Goldstein and M.R. Van de Mark. Electrode cleaning and anion effects on k_s for $K_3Fe(CN)_6$ couple. *Electrochim. Acta*, 27:1079–1085, 1982.

[269] J. Kawiak, T. Jedral, and Z. Galus. A reconsideration of the kinetic data for the $Fe(CN)_6^{3-}/Fe(CN)_6^{4-}$ system. *J. Electroanal. Chem.*, 145:163–171, 1983.

[270] J. Kawiak, P.J. Kulesza, and Z. Galus. A search for conditions permitting model behavior of the $Fe(CN)_6^{3-/4-}$ system. *J. Electroanal. Chem.*, 226:305–314, 1987.

[271] C. Beriet and D. Pletcher. A microelectrode study of the mechanism and kinetics of the ferro/ferricyanide couple in aqueous media: the influence of the electrolyte and its concentration. *J. Electroanal. Chem.*, 361:93–101, 1993.

[272] W.P. Gomes and F. Cardon. Electron energy levels in semiconductor electrochemistry. *Prog. Surf. Sci.*, 12:155–215, 1982.

[273] A.J. Nozik. Photoelectrochemistry: Applications to Solar Energy Conversion. *Annu. Rev. Phys. Chem.*, 29:189–222, 1978.

[274] S.R. Morrison. *Electrochemistry at semiconductor and oxidized metal electrodes*. Plenum Press, New York, 1980.

[275] A. Wieckowski and M. Szklarzyk. The state of the polycrystalline platinum electrode during the heterogeneous electron-transfer reaction: $Fe(CN)_6^{3-}$ + $e^- \leftrightarrow Fe(CN)_6^{4-}$. *J. Electroanal. Chem.*, 142:157–170, 1982.

[276] K. Schroder and R. Memming. Analysis of trapping and recombination effects in photoelectrochemical processes at semiconductor electrodes—investigations at n-gaas. *Ber Bunsen-Ges Phys Chem Chem Phys*, 89:385–392, 1985.

[277] J.J. Kelly and R. Memming. The Influence of Surface Recombination and Trapping on the Cathodic Photocurrent at p-Type III-V Electrodes. *J. Electrochem. Soc.*, 129:730–738, 1982.

[278] R. Feeney and S.P. Kounaves. Determination of heterogeneous electron transfer rate constants at microfabricated iridium electrodes. *Electrochem. Commun.*, 1:453–458, 1999.

[279] K. Ueno, Y. Serizawa, and M. Seo. Influence of the $Fe(CN)_6^{3-}/Fe(CN)_6^{4-}$ redox reaction on the changes in surface energy of a gold electrode in perchlorate solution with iodide ions. *Electrochemistry*, 67:1123–1125, 1999.

[280] N. H. Jalani, K. Dunn, and R. Datta. Synthesis and characterization of Nafion-MO_2 (M = Zr, Si, Ti) nanocomposite membranes for higher temperature PEM fuel cells. *Electrochim. Acta*, 51(3):553–560, 2005.

[281] V. Antonucci, A. Di Blasi, V. Baglio, R. Ornelas, F. Matteucci, J. Ledesma-Garcia, L.G. Arriaga, and A.S. Arico. High temperature operation of a composite membrane-based solid polymer electrolyte water electrolyser. *Electrochim. Acta*, 53:7350–7356, 2008.

[282] J.S. Wainright, J.-T. Wang, D. Weng, R.F. Savinell, and M. Litt. Acid-Doped Polybenzimidazoles: A New Polymer Electrolyte. *J. Electrochem. Soc.*, 142:L121–L123, 1995.

[283] J.-T. Wang, R.F. Savinell, J. Wainright, M. Litt, and H. Yu. A H_2/O_2 fuel cell using acid doped polybenzimidazole as polymer electrolyte. *Electrochim. Acta*, 41:193–197, 1996.

[284] S. Motoo and N. Furuya. Effect of anions on hydrogen and oxygen adsorption on iridium single cyrstal surfaces. *J. Electroanal. Chem.*, 181:301–305, 1984.

[285] A. R. Hillman. The electrochemical quartz crystal microbalance. In P. R. Unwin, editor, *Instrumentation and Electroanalytical Chemistry,* In A. J. Bard and M. Stramann (Series Eds.), *Encyclopedia of Electrochemistry*, volume 3, pages 23–24. Wiley-VCH, 2003.

[286] M. Urbakh and L. Daikhin. Influence of the surface morphology on the quartz crystal microbalance response in a fluid. *Langmuir*, 10(8):2836–2841, 1994.

[287] L. B. Kriksunov. The temperature dependence of the tafel slope for parallel electrochemical reactions. *Electrochim. Acta*, 40(15):2553–2555, 1995.

Acronyms

AES	Augerelectron spectroscopy
AFM	Atomic force microscopy
AIROF	Anodically formed iridium oxide film
BET	Brunauer, Emmett and Teller surface area (by nitrogen adsorption)
CB	Conduction band
CE	Counter electrode
CEF	Charge enhancement factor
cus	Coordinatively unsaturated site
CV	Cyclic voltammogram
CVD	Chemical vapour deposition
DHE	Dynamic hydrogen electrode (i.e. $Pt\|H_2(g)$ at the test solutions pH)
DFT	Density functional theory
DSA	Dimensionally Stable Anodes
EDS	Energy dispersive spectroscopy
EIS	Electrochemical impedance spectroscopy
EQCM	Electrochemical quartz crystal microbalance
HHV	Higher heating value
IEP	Isoelectric point
ITO	Indium-doped tin oxide
EXAFS	Extended X-ray adsorption spectroscopy fine structure
LHV	Lower heating value
NHE	Normal hydrogen electrode (equal to SHE)
OER	Oxygen evolution reaction
PBI	Polybenzimidazole
PEM	Polymer electrolyte membrane
PVD	Physical vapour deposition
pzc	Point of zero charge
RDE	Rotating disc electrode
RDS	Rate determining step
RE	Reference electrode
SCE	Saturated calomel electrode (+0.2415 V vs. SHE)
SEM	Scanning electron microscopy
SHE	Standard hydrogen electrode
STM	Scanning tunnelling spectroscopy
TEOM	Tapered element oscillationg microbalance

TFMSA	Trifluoromethanesulfonic acid
TGA	Thermo gravimetric analysis
TPA	Temperature programmed analysis
UPS	Ultraviolet photoemission spectroscopy
VB	Valence band
WE	Working electrode
XAS	X-ray adsorption spectroscopy
XPS	X-ray photoelectron spectroscopy
XRD	X-ray diffraction

List of Figures

List of Tables